UNIVERSITÀ DEGLI STUDI DI MILANO-BICOCCA
Facoltà di Scienze MM.FF.NN.
Scuola di Dottorato in Scienza dei Materiali
XXIII Ciclo

First principles study of the $LiNH_2/Li_2NH$ hydrogen storage system

Author:
Giacomo Miceli

Supervisor:
Prof. Dr. Marco Bernasconi

December 2010

— Et qu'est-ce qu'on brûlera à la place du charbon ?

— L'eau, répondit Cyrus Smith.

— L'eau, s'écria Pencroff, l'eau pour chauffer les bateaux à vapeur et les locomotives, l'eau pour chauffer l'eau !

— Oui, mais l'eau décomposée en ses éléments constitutifs, répondit Cyrus Smith, et décomposée, sans doute, par l'électricité, qui sera devenue alors une force puissante et maniable, car toutes les grandes découvertes, par une loi inexplicable, semblent concorder et se compléter au même moment. Oui, mes amis, je crois que l'eau sera un jour employée comme combustible, que l'hydrogène et l'oxygène, qui la constituent, utilisés isolément ou simultanément, fourniront une source de chaleur et de lumière inépuisables et d'une intensité que la houille ne saurait avoir. Un jour, les soutes des steamers et les tenders des locomotives, au lieu de charbon, seront chargés de ces deux gaz comprimés, qui brûleront dans les foyers avec une énorme puissance calorifique. Ainsi donc, rien à craindre. Tant que cette terre sera habitée, elle fournira aux besoins de ses habitants, et ils ne manqueront jamais ni de lumière ni de chaleur, pas plus qu'ils ne manqueront des productions des règnes végétal, minéral ou animal. Je crois donc que lorsque les gisements de houille seront épuisés, on chauffera et on se chauffera avec de l'eau. L'eau est le charbon de l'avenir.

— Je voudrais voir cela, dit le marin.

Jule Verne, ***L'île mystérieuse***, 1874 [1]

To my Mother
for her never-ending support
and encouragement

Contents

Nomenclature

a.u.	atomic units (in this thesis I normally use atomic units, with $e^2 = \hbar = m_e = 1$).
DFT	density functional theory
DoE	U.S. Department of Energy
GGA	generalized gradient approximation (DFT-GGA)
HH	$Imma$ Li_2NH crystal structure as obtained after geometry optimization of the $Ima2$ structure performed by *ab initio* calculations
HT	high temperature
LDA	local density approximation (DFT-LDA)
LHV	lower heating value
Li1	● (Green) lithium placed at the 48f sites of $Fd\bar{3}m$ space group
Li2	● (Dark Green) lithium placed at the 8a sites of $Fd\bar{3}m$ space group
Li3	● (Light Green) lithium (interstitial) placed at the 32e sites of $Fd\bar{3}m$ space group
Li4	● (Light Green like Li3) lithium (interstitial) placed at the 16c sites of $Fd\bar{3}m$ space group
LT	low temperature
MC	$Pbca$ crystal structure of Li_2NH
MOW	$Pnma$ crystal structure of Li_2NH

NEB	nudged elastic band
PMD	proton momentum distribution
PND	powder neutron diffraction
TBD	to be determined
TST	transition state theory
XRD	X-ray diffraction

Introduction

Hydrogen is undoubtedly one of the key alternatives to replace petroleum products as a clean energy carrier for both transportation and stationary applications. In fact, hydrogen, ultimately derived from renewable sources and used as an energy vector, must be considered as a major component of a sustainable energy future in the world. On the other hand, the safe and efficient storage of hydrogen is widely recognized as one of the key technological challenges in the transition towards a hydrogen-based energy economy [2, 3]. Whereas hydrogen for transportation applications is currently stored using cryogenics or high pressure, there is substantial research and development activity in the use of novel condensed-phase hydride materials. An ideal hydride material will be characterized by the following features: have a good gravimetric capacity (low reservoir/storage mass), have a good volumetric capacity, be inexpensive, have a rapid kinetics for absorbing and desorbing H_2 in the 25–120 °C temperature range and store large quantity of hydrogen reversibly. However, the multiple-target criteria necessary for the successful implementation of such stores have not yet been met by any single material (cf. U.S. Department of Energy, DoE [4]).

Bogdanovic and Schwickardi [5, 6] demonstrated upon doping with proper titanium compounds, the dehydriding of sodium aluminum hydrides, $NaAlH_4$, could be kinetically enhanced and maintain reversibility under moderate conditions in the solid state. These studies were to pave the way for a whole new branch of research on so called *complex hydrides* [7, 8]. These compounds are group I and II salts of $[AlH_4]^-$, $[NH_2]^-$ and $[BH_4]^-$, currently referred to as *alanates*, *amides*, and *borohydrides*, respectively. These compounds attracted a lot interest because of their light weight and the capacity for a large number of hydrogen atoms per metal atom (high gravimetric and volumetric capacities, respectively up to 18 wt% and hydrogen density of 150 kg m^{-3}). However, many of these systems are thermodynamically very stable, resulting in a very high operating temperature. Furthermore, since the release of hydrogen occurs via a solid state

decomposition reaction, the kinetics is very slow. Research is devoted to improve these two aspect aiming at lowering the desorption temperature and increasing the rate of release of hydrogen. In this work we focused our attention on the lithium amide/imide, $LiNH_2/Li_2NH$, hydrogen storage system.

Recently, P. Chen *et al.* [9] discovered that lithium amide can store a large amount of hydrogen and its release occurs in the mixture $LiNH_2 + LiH$ via a reversible solid state decomposition reaction into lithium imide (Li_2NH) and molecular hydrogen

$$LiNH_2 + LiH \rightleftharpoons Li_2NH + H_2 \,. \tag{1}$$

This reaction occurs at a typical operating temperature of about 280 °C with a theoretical hydrogen release of 6.5 wt%. Furthermore, the measured value of the reaction enthalpy is 65.6 kJ/(mol H_2) which yields an equilibrium temperature of 230 °C at normal pressure, which is probably too high for on-board applications. Nevertheless, the amide decomposition reaction is under deep scrutiny since understanding the microscopic mechanisms behind the release of hydrogen from this simple system could shed light on the mechanisms of reversible H-storage in the more complex, and more promising, reactive hydrides made of mixtures of amide, borohydrides and/or alanates (e.g., $LiNH_2/LiBH_4$ or $LiNH_2/NaAlH_4$ [10]).

The search for better performing materials in the class of complex hydrides would greatly benefit from a microscopic knowledge of the decomposition mechanism. This requires a detailed description of the crystalline phases involved. However, for several complex hydrides the structure of the phases undergoing the dehydrogenation/rehydrogenation process is still not fully resolved. This is also the case for the low temperature crystal structure of Li_2NH, which is the product of the $LiNH_2$ decomposition.

By means of *ab initio* simulations we have resolved the structure of the two crystalline phases of Li_2NH stable below and above 356 K and provide a comprehensive description of the elementary steps in the dehydrogenation and rehydrogenation processes. We performed molecular dynamics simulations based on density-functional theory and optimizations of the reaction pathways of elementary steps to provide estimates of reaction rates within the harmonic transition state theory.

Concerning the structure of Li_2NH, neutron diffraction experiments have identified a stable anti-fluorite structure above 356 K with space group $Fm\bar{3}m$, in which hydrogen atoms randomly occupy the 192l sites. On the contrary the low temperature (LT) crystal structure of Li_2NH is still matter of debate. Structural refinement from neutron and X-rays diffraction data reveals a structure of Li_2NH with $Fd\bar{3}m$ space group consisting of an anti-fluorite structure with Li Frenkel pairs generating interstitial Li atoms on the 32e sites with fractional occupation [11]. However, this structure displays anomalously short Li–Li distance of 1.56 Å. Upon geometry optimization by means of DFT, these short distances are removed leading, however, to atomic positions incompatible with neutron diffraction data.

Aiming at identifying the LT structure of Li_2NH, we performed molecular dynamics simulations starting from a realization of the $Fd\bar{3}m$ geometry proposed experimentally. The simulations revealed preferential ordering of Li interstitials forming Li_4-clusters. The structure that emerges from the simulations does not contain the short Li–Li distance but is nevertheless compatible with neutron diffraction data thus solving the inconsistencies of previous proposals. By heating the low temperature phase we have identified the

mechanism of phase transition and the structure of the high temperature phase. It turns out that the higher $Fm\bar{3}m$ symmetry of the high temperature phase is the result of dynamical disorder involving diffusion of Li interstitials and vacancies. However, an instantaneous snapshot of the dynamics reveals a local structure more similar to that of the low temperature phase considered so far.

Concerning the transformation process of Li amide into imide, Chen and coworkers [12] initially suggested that formation of hydrogen occurs at the interface between $LiNH_2$ and LiH by combination of the two different charged species H^- from LiH and H^+ from $LiNH_2$. However, experimental studies with isotopic labeling does not confirm this idea. On the other hand, a two step reaction has been suggested for the decomposition of $LiNH_2$ by Ichikawa and coworkers [13]. Following this latter proposal lithium amide first decomposes into Li_2NH and releases gaseous NH_3. In the second step ammonia reacts with LiH forming $LiNH_2$ and releasing molecular hydrogen

$$2\,LiNH_2 \longrightarrow Li_2NH + NH_3 \tag{2}$$

$$NH_3 + LiH \longrightarrow LiNH_2 + H_2\,. \tag{3}$$

The second step of the reaction is known to be very fast [14], therefore the kinetics of the whole decomposition process is controlled by the evolution of ammonia. This latter ammonia mediated mechanism was substantiated by isotopic labeling experiments [15]. Similar ammonia-mediated decomposition pathways have also been proposed for the $Mg(NH_2)_2$/LiH mixtures [16].

Using *ex situ* synchrotron XRD and probing the amide–imide step of storage cycle, David *et al.* [17] proposed a mechanism in which ammonia formation occurs in $LiNH_2$ bulk and that the system evolves into Li_2NH through sub-stoichiometric phases. Furthermore, they suggested that formation of Frenkel pairs is the key factor for ammonia formation and so $LiNH_2$ decomposition. On the contrary, by means of kinetic measurements of hydrogen evolution from ball milled samples, Shaw *et al.* [18] showed that the decomposition process starts at the $LiNH_2$ surface, Li_2NH grows as a shell around a shrinking core of $LiNH_2$. The diffusion of ammonia inside Li_2NH represents the rate-limiting step of the whole reaction.

Aiming at providing a theoretical support to the two steps decompositions mechanism and clarifying the role of surfaces in this process, in this thesis we present the results of *ab initio* calculations of activation energies of different elementary steps that we hypothesize to be crucial for the ammonia mediated transformation path focusing in particular on the first step of the reaction

$$2\,LiNH_2 \longrightarrow Li_2NH + NH_3\,.$$

We first analyzed the formation of ammonia via a proton transfer between two NH_2^- groups in the presence or in the absence of a Li Frenkel pair in the bulk and at the surface of $LiNH_2$. Diffusivity of H^+ (*i.e.*, NH_3 via a Grotthuss mechanism), H^+ vacancy (NH^{2-}) and Li^+ species in $LiNH_2$, and Li_2NH were then computed to contrast the alternative scenarios described above. The H^+ and Li^+ transfer across the $LiNH_2/Li_2NH$ interface was also investigated as well as the ammonia desorption from the Li_2NH and $LiNH_2$ surfaces. The scenario for the decomposition mechanism of $LiNH_2$ emerging from the simulations suggests that the transformation path depends on the surface-to-volume

ratio. The formation of sub-stoichiometric phases is possibly favored in bulk material with a small surface-to-volume ratio, while the direct formation of imide is favored in the presence of small crystallites (large surface-to-volume ratio) that transform according to the core-shrinking model of Ref. [18]. Our results thus allow reconciling the apparently contradicting results on the presence of sub-stoichiometric phases inferred from X-ray data in Ref. [17] with the kinetic data of Ref. [18] suggesting the growth of a Li_2NH shell outside a $LiNH_2$ shrinking core. The simulations provide a comprehensive description of formation of defects and diffusivity in the bulk and at the surface of Li amide and imide that is open to experimental verification, for example, by measurements of the ionic conductivity. Preliminary and ongoing analysis of the hydrogenation of Li_2NH ($Li_2NH + H_2 \longrightarrow LiNH_2 + LiH$) that has been pursued by *ab initio* calculations is also presented.

Thesis structure

This thesis is organized as follows:

Chapter 1 we give a brief overview on the state-of-the-art of hydrogen storage systems and materials.

Chapter 2 a literature survey of the properties of $LiNH_2$ / Li_2NH system is given pointing out the open issues that we have addressed in the thesis.

Chapter 3 in this chapter we give a brief description of the theory and methods we used for our theoretical investigation of the $LiNH_2/Li_2NH$ system.

Results

Chapter 4 We present our results on the low and high temperature phases of Li_2NH.

Chapter 5 In this chapter we discuss the scenario for the decomposition pathways that emerges from the *ab initio* calculations of the elementary reaction steps.

Chapter 6 An analysis of the elementary steps in the rehydrogenation process of Li_2NH is presented.

1

Hydrogen storage technologies

There are significant concerns about the rising level of CO_2 emissions and the impact this is having on our environment (IPPC 2007 [19]). The main sources of the increase in CO_2 is from our increasing energy demands. The right direction to follow is not only to limit the energy consumption, but it needs to further reduce CO_2 emissions and alternatives to burning fossil fuels are required.

Hydrogen is an attractive alternative to carbon-based fuels. It has a high calorimetric value, with a lower heating value (LHV, *i.e.* the heat released upon combustion without recovery of the latent heat of vaporization of any water produced) of 120 MJ kg^{-1}, compared with petrol, which is approximately a third of this at 43 MJ kg^{-1}. Furthermore, part of its attraction is that it can be produced from diverse resources, both renewable (hydro, wind, solar, biomass, geothermal) and non-renewable (coal, natural gas, nuclear).

Hydrogen can be used for power generation either by combustion, for example in an internal combustion engine (ICE), producing mechanical power or electrochemically by using a fuel cell (F-Cell) producing electrical power. In both cases the hydrogen reacts with oxygen to form water (in F-Cell water is the only emission, however for ICE there is also some NO_x depending on how hot is the combustion). In any case, using hydrogen with fuel cells is the most efficient method for all applications.

Hydrogen fuel cells have a large range of potential applications operating from a few watts up to gigawatts as shown graphically in Fig. 1.1. In particular, automotive hydrogen storage is seen as one of the biggest potential markets for hydrogen, replacing the use of petrol and diesel. However at the present time, there are three major technological barriers that must be overcome for a transition from a carbon-based (fossil fuel) energy system to a hydrogen-based economy. First, the cost of efficient and sustainable hydrogen production and delivery must be significantly reduced. Secondly, the cost of fuel cell and other hydrogen-based systems must be reduced. Last but not the least, new generations of hydrogen storage systems for both vehicular and stationary applications must be developed. One of the crucial technological barriers to the wide spread use of hydrogen as an effective energy carrier is the lack of a safe, low-weight and low-cost hydrogen storage method with a high energy density [20, 21]. Hydrogen contains more

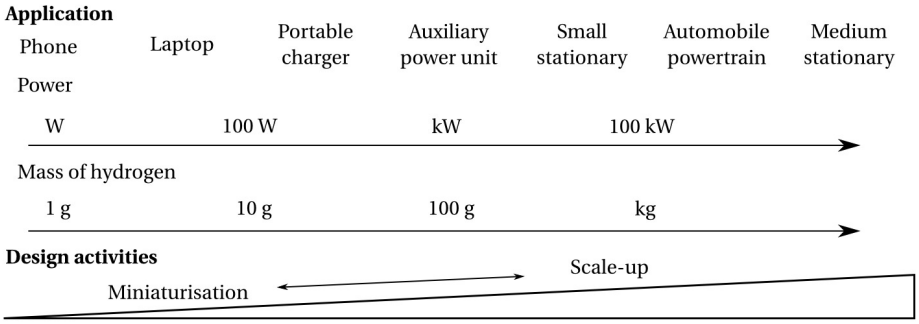

Figure 1.1: The scheme indicates the power requirement and corresponding mass of hydrogen for various applications.

energy on a weight-for-weight basis than any other substance. Unfortunately, since it is the lightest chemical element in the Periodic Table, it also has a very low energy density per unit volume (cf. Tab. 1.1).

Table 1.1: Below the specific energy and energy density of fuels, hydrogen storage options and energy sources are reported. Here the volume and the weight of the containers are excluded (cf. Ref. [22]).

Fuel	**Specific energy (kWh/kg)**	**Energy density (kWh/dm^3)**
Liquid hydrogen	33.3	2.37
Hydrogen (200bar)	33.3	0.53
Liquid natural gas	13.9	5.6
Natural gas (200bar)	13.9	2.3
Petrol	12.8	9.5
Diesel	12.6	10.6
Coal	8.2	7.6
NH_3BH_3	6.5	5.5
Methanol	5.5	4.4
Wood	4.2	3.0
Electricity (Li-ion battery)	0.55	1.69

The challenge with hydrogen is that it is a low-density gas and it is difficult to efficiently store enough hydrogen on-board to give the vehicle an adequate range, *e.g. c.* 5 kg of hydrogen for range of 500 km [2]. There are limitations on developing new technologies for on-board H-storage by the Department of Energy (DoE 2006-2009 see

Table 1.2: Performance targets revised in 2009 based on real-world experience with hydrogen fuel cell vehicles (see Ref. [4]). Old and new targets refer to DoE 2006 and DoE 2009 respectively. Ultimate targets are intended to facilitate the introduction of hydrogen-fueled propulsion systems across the majority of vehicle classes and models.

target	**2015 (old)**	**2015 (new)**	**ultimate**
System Gravimetric Density [wt.%] (kWh/kg)	[9] (3.0)	[5.5] (1.8)	[7.5] (2.5)
System Volumetric Density [g/L] (kWh/L)	[81] (2.7)	[40] (1.3)	[70] (2.3)
System fill time for 5-kg fill [min] (kgH_2/min)	[2.5] (2.0)	[3.3] (1.5)	[2.5] (2.0)
System cost [\$/kgH_2] (\$/kWh_{net})	[67] (2)	TBD	TBD

Tab. 1.2). The targets for hydrogen storage system (including the container and any balance-of-plant) shows the importance of both gravimetric and volumetric capacity of the store, as one does not want the store to be too heavy (limiting the range of the vehicle) or too voluminous (limiting the cabin and/or the luggage space).

The methods which are currently under development or investigation are physical and chemical storage methods. Physical methods include:

- compressed gaseous hydrogen (CGH_2)
- liquid hydrogen (LH_2)
- cryo-adsorption on high surface area materials (through weak van der Waals forces)

On the other hand, in the chemical method hydrogen is chemically bound to the host material forming a new compound (*e.g.* metal hydrides and complex hydrides) and hydrogen is released through a thermal decomposition and/or chemical reaction, typically through a hydrolysis reaction. Chemical methods include storage in the following system/material:

- metal hydrides MH_x
- complex hydrides $M(AH_x)_y$, with A = B, N, Al
- solid state reaction systems (mix of metal hydride and complex hydride)
- chemical hydrides, hydrolysis reaction (not reversible)[1]

[1] with the term Chemical Hydrides here we indicate all the hydrides which react in a not reversible way. These compounds react with water and release gaseous hydrogen.

- organic liquids

1.1 Physical methods for H-storage

The most common way to store hydrogen is to put gaseous hydrogen in high-pressure tanks. Composite cylinders are used as these are lighter than metal only, and typically have a working pressure of 350 bar up to 700 bar in the new generation high-pressure tanks. In the latter case, the gravimetric storage capacity is 4.5 wt% which is close to the DoE 2015 target (cf. Tab. 1.2), but the volumetric capacity is quite low. Furthermore, these high-pressure containers, when filled by about 4% hydrogen by mass, present significant disadvantages: the fuel would be available at a pressure dropping from ~700 bar to zero overpressure, so additional pressure control would be essential. High-pressure vessels present a considerable risk – the compression itself is the most dangerous and complicated part.

Another common but more sophisticated physical method is to store hydrogen in tanks in liquid form. However, such technologies refuel at very low temperature. In fact, hydrogen can not be liquefied above 20 K (this is the boiling point at 1 atmosphere). Under these conditions the density of the liquid is 0.0708 kg l^{-1}, which means a respectable volumetric capacity of 2.35 kWh l^{-1}. Storing hydrogen as a liquid, however, is not convenient because it is a very expensive process. In practice the energetic cost for liquefaction is about 10-15 kWh/kg which is 1/3 of the lower heating value (LHV). This leads to an enormous loss in efficiency for the system. Furthermore, very little energy is required to evaporate liquid hydrogen (about 0.45 MJ/kg H_2) so it continuously escapes from the tank as a consequence of the inevitable heat transfer from the exterior. The evaporated hydrogen cannot be re-liquefied because it is above the critical point (this is the so called boil-off problem). To avoid safety problems, the over-pressurized hydrogen has to be released (a loss of 4-5% per day which again lowers the efficiency). This is highly undesirable in automotive applications as it is wasteful of the hydrogen and could have serious safety issues for a vehicle left in an enclosed space for a few days. Thermal insulation to minimize the heat flow from the surrounding to the liquid hydrogen are crucial; therefore the design of tanks aims to minimize the surface area of the liquid and thus minimize heat transfer to the liquid. This problem is strictly connected with the efficiency of the storage, specifically with the volume of the container inside the car. Nevertheless, liquid hydrogen is currently used in space technology and recently also in automotive technology. Recently, hybrid dual-fuel vehicles storing liquid hydrogen have been developed. This technology provides the possibility of directly injecting liquid hydrogen in to internal combustion engines. However, since liquefying hydrogen is a complicated and very expensive procedure, this technology can not be extended to a large scale use.

Hydrogen, like any other gas, will physisorb onto a surface. The diatomic molecule does not dissociate and it is held to the surface through weak van der Waals interactions. The strength of these interactions is very weak with an enthalpy of adsorption, ΔH_a of between 4 and 10 kJ mol^{-1}. Therefore, low temperatures are needed to obtain significant amounts of adsorbed gas. Hydrogen physisorption is normally measured at liquid nitrogen temperature (77–80 K). Once a monolayer of adsorbate H_2 molecules

has formed, the gaseous species interacts with the liquid adsorbate. Thus, the binding energy of the second layer of adsorbates is similar to the latent heat of vaporization of the adsorbate. Consequently, working at 77 K leads to the adsorption of a single monolayer. For this reason the most important factors that determine the storage capacity are the specific surface area and/or the micropore volume. It is very important to stress the fact that H_2 behaves like a liquid in micropores at 77 K. Porous materials which have received considerable attention are high surface area carbons [23], carbon nanotubes [24], zeolites [25], metal-organic frameworks [26] and, more recently polymers of intrinsic microporosity [27].

1.2 Chemical methods for H-storage

Metal hydrides are the prototypical materials for chemical storage of hydrogen. Many metals and alloys are capable of reversibly absorbing large amounts of hydrogen. Molecular hydrogen is dissociated at the surface before absorption; two H atoms recombine to form H_2 in the desorption process. The regeneration of the metal can be accomplished either by increasing temperature or by reducing the H partial pressure. In fact, the thermodynamics of hydride formation from gaseous hydrogen is described by the pressure–composition isotherms (PCI) (shown in Fig. 1.2).

The host metal initially absorb some hydrogen as a solid solution, the α-phase. As the hydrogen pressure and the concentration of H in the metal is increased, a new ordered phase, namely the β-phase, is formed and keeps growing. While the two phases coexist, the isotherms show a flat plateau, the length of which determines how much H_2 can be stored reversibly with small pressure variations. In the pure β-phase, the H_2 pressure rises steeply with the concentration. At higher H_2 pressure, further plateaux and so hydride phases may be observed. The two-phase region ends in a critical point T_c, above which the transition from α- to β-phase is continuous. The plateau or equilibrium pressure depends strongly on temperature and is related to the thermodynamic properties of the material, which means on the changes ΔH and ΔS of enthalpy and entropy, respectively, following the van't Hoff equation

$$\ln\left(\frac{P_{eq}}{P^0_{eq}}\right) = \left(-\frac{\Delta H}{R}\right)\left(\frac{1}{T}\right) + \frac{\Delta S}{R}$$

where, essentially, ΔS is the entropy of gaseous hydrogen, $\approx$ 130 kJ/mol K^{-1} at 300 K. From the slope and the intercept of the van't Hoff plot, the experimental values of ΔH and ΔS can be valuated and thus thermodynamics of transformation of the material investigated (cf. Fig. 1.2).

Unfortunately, the metals and alloys with an operating temperature less then 80 °C at 1 bar are based on heavy transition metals (*e.g.* $LaNi_5$ and FeTi) and therefore have low gravimetric hydrogen storage capacities as shown in Fig. 1.3. It can be seen though that these materials have volumetric capacities far superior to that of liquid hydrogen. Because of the low gravimetric capacity for these interstitial metal hydrides, there has been a lot of interest in higher capacity materials such as magnesium hydride (with a storage capacity of 7.6 wt%) even though this has an operating temperature of 280 °C at 1 bar. On the other hand, interest grew in the use of complex hydrides when

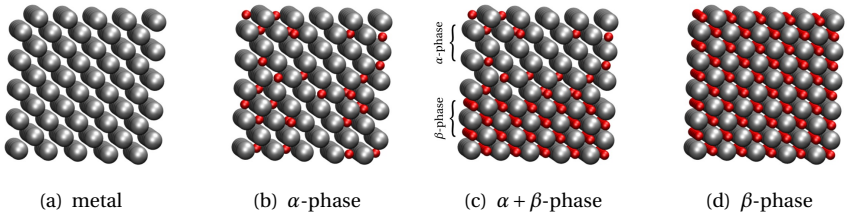

(a) metal (b) α-phase (c) $\alpha+\beta$-phase (d) β-phase

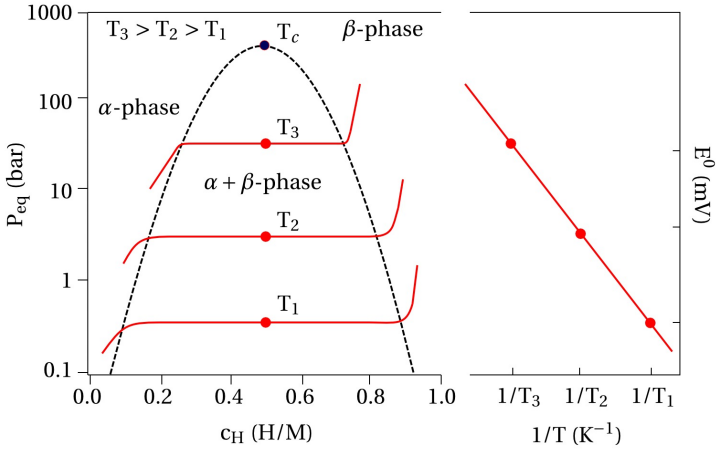

Figure 1.2: Isothermal Pressure–Composition plot and a van't Hoff curve (logarithm of the equilibrium of plateau pressure against the reciprocal temperature. From the slope of the van't Hoff plot, experimental values of the enthalpy, ΔH, and entropy, ΔS, change of hydride formation can be evaluated. The plateau pressure $P_{eq}(T)$ as a function of temperature is related to the changes ΔH and ΔS of enthalpy and entropy, respectively, by the van't Hoff equation: $\ln(P_{eq}/P^0_{eq}) = (-\Delta H/R)(1/T) + \Delta S/R$. Above a graphical representation of the transformation from the pure metal to the metal-hydride. (b) In the α-phase hydrogen atoms are dissolved into the bulk of the metal (solid solution). (c) At the plateau the hydride precipitate ($\alpha+\beta$-phase). (d) The metal is fully hydrogenated (β-phase), metal-hydride.

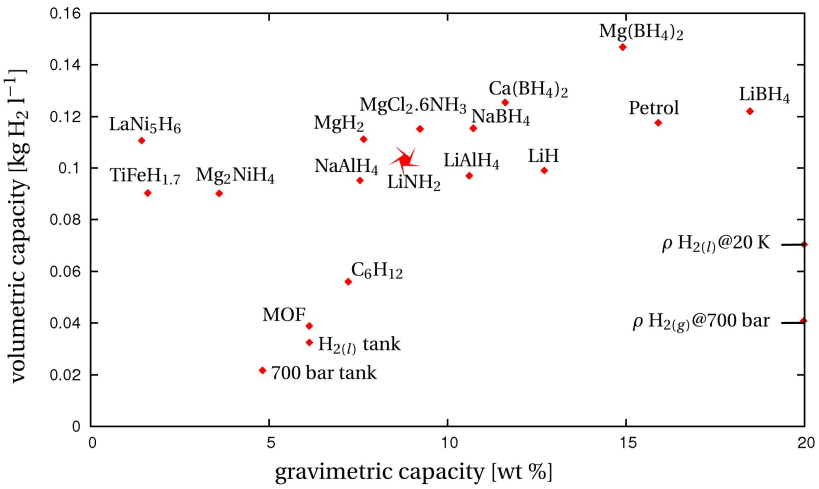

Figure 1.3: Theoretical hydrogen storage capacities for a range of storage systems (position of $LiNH_2$ in the graph is highlighted). For reference the density of liquid hydrogen, $\rho H_{2(l)}$ at 20 K, and hydrogen gas, $\rho H_{2(g)}$ at 700 bar, are given on the right of the graph.

Bogdanović and Schwickardi in 1997 [5] showed that titanium-based catalysts enable sodium alanate to be reversibly dehydrogenated (having a theoretical capacity of 7.5 wt%). In addition to this compound, there has been much interest in lithium amide and tetrahydroborates of lithium. These compounds are representative of three large families of complex hydrides namely alanates (M-AlH_4), amides (M-NH_2), borates (M-BH_4). The decomposition process of these materials follows the reactions below

(Na) Alanates

$$\begin{aligned} NaAlH_4 &\rightleftharpoons \tfrac{1}{3}Na_3AlH_6 + \tfrac{2}{3}Al + H_2 \\ \tfrac{1}{3}Na_3AlH_6 + \tfrac{2}{3}Al + H_2 &\rightleftharpoons NaH + Al + \tfrac{3}{2}H_2 \end{aligned} \tag{1.1}$$

(Li) Amides

$$LiNH_2 + LiH \rightleftharpoons Li_2NH + H_2 \tag{1.2}$$

(Li) Borates

$$LiBH_4 \longrightarrow LiH + B + \tfrac{3}{2}H_2 \tag{1.3}$$

Although these compounds achieve very high capacities for hydrogen storage, both gravimetric and volumetric, most of the time their dehydrogenation enthalpy is large resulting in a high operating temperature due to the fact that T at 1bar = $\Delta H/\Delta S$. One of the most promising strategies to destabilize complex hydrides is the replacement of single cation or single anions by mixed cations or mixed anions. This technique weakens the otherwise strong covalent bond between the hydrogen and the element A (where A is one of Al, B, N). In practice, the complex hydride, M-AH_x, is mixed with

another compound, M'. If during dehydrogenation M' is able to react with M and form an alloy we gain its enthalpy of formation which lowers the enthalpy of the overall transformation. This idea led to the proposal of the so called solid-state reaction systems (*e.g.* $LiBH_4/MgH_2$ Ref. [28], $LiNH_2/LiBH_4$ and $LiNH_2/NaAlH_4$ Ref. [10]).

The actual operating temperature is usually higher than the thermodynamical decomposition temperature due to kinetic hindrances. In several systems the activation barriers controlling the hydrogenation/dehydrogenation kinetics can be lowered by the addition of catalysts, such as titanium in $NaAlH_4$. An effective catalyst for different systems requires a better knowledge of the transformation process including the nature of the rate-limiting step that currently exists. Even in the most studied $Ti/NaAlH_4$ system the atomistic mechanism by which Ti displays its catalystic activity is still longly unknown.

The possibility of mixing different alanates, amides, borates and metal hydrides (*e.g.* MgH_2) leads to a rich playground for scientists in the search of new materials suitable to meet all the requirements for on-board hydrogen storage. This search would greatly benefit from a detailed atomistic knowledge of the transformation process which so far is unknown even for the simplest compounds. In this respect atomistic simulations can provide rich insight as we will demonstrate in the following chapters for the $LiNH_2$ / Li_2NH system.

2

Hydrogen storage in the $LiNH_2/Li_2NH$ system

An important milestone in the progress of solid-state hydrogen storage materials occurred when P. Chen *et al.* discovered that hydrogen can be reversibly stored in the $LiNH_2/Li_2NH$ system [9]. In fact, this discovery was important not only for practical reasons of H-storage (storing hydrogen in such a way it is possible to meet the gravimetric and volumetric criteria of the U.S. Department of Energy (DoE) [4]) but it was also revolutionary in the solid-state storage area. The Li–N–H system, unlike other "chemical hydrides[1]", is composed of both metallic and non-metallic elements in which the storage process involves the breaking and forming of the non-metal (N)-hydrogen bonds. The ramifications of this discovery were immediate but it soon became apparent that many of the challenges of previously studied complex hydrides (reversibility, kinetics, operating temperatures) would also be faced in $LiNH_2/Li_2NH$ system.

In this Chapter we will present a literature survey on the $LiNH_2$ / Li_2NH system. Experimental data on the microscopic structure of $LiNH_2$ and Li_2NH and on the microscopic mechanisms involved in the process of desorption are presented together with previous theoretical attempts on modeling the system. At the same time the issues of controversy are presented as well postponing in the Results part our contribution on this area of research.

2.1 The hydrogenation/dehydrogenation reaction

Lithium amide, $LiNH_2$, became of technological interest in 2002 when P. Chen *et al.* [9] showed that a suitable process occurs which allows storage of hydrogen in a reversible way. Following the original idea of Dafert and Miklauz [29] and Ruff and Georges [30], Chen and coworkers demonstrated a reversible hydrogen storage process according to the two step reaction

$$Li_3N + 2H_2 \rightleftharpoons Li_2NH + LiH + H_2 \rightleftharpoons LiNH_2 + 2LiH\,. \tag{2.1}$$

[1] here with the term *chemical hydrides* we indicate all the systems in which the hydrogen is stored through a chemical bond.

Table 2.1: Solid-state hydrogen storage properties of $LiNH_2/Li_2NH$ system ($LiNH_2 + LiH \longrightarrow Li_2NH + H_2$).

Theoretical amount of hydrogen stored	6.5 wt%
Typical operating temperature	280 °C
Equilibrium temperature at normal pressure	230 °C

The overall gravimetric and volumetric hydrogen storage capacity was measured as 9.3 wt% and 10 wt%. By taking the standard enthalpies of formation, the overall heat of reaction (2.1) was calculated to be -161 kJ mol^{-1}. In fact, only the second step of the reaction, cycling between amide and imide, is reversible at moderate H partial pressure. Desorption of hydrogen by decomposition of lithium imide into lithium nitride is possible only above 320 °C at 10^{-5} mbar of pressure, clearly a value too high for on-board applications. On the other hand, the transformation between Li amide ($LiNH_2$) and Li imide (Li_2NH) takes place at milder conditions [12, 31, 10, 7].

Hydrogen release from the mixture $LiNH_2 + LiH$ takes place according to

$$LiNH_2 + LiH \longrightarrow Li_2NH + H_2\,. \tag{2.2}$$

at a typical operating temperature of about 280 °C [9, 12, 18, 32, 33] with a maximum capacity of 6.5 wt% of hydrogen. The reaction enthalpy has been calculated within the framework of Density Functional Theory (DFT) [34] to be 73.6 kJ/ (mol H_2) close to the experimentally measured value of 65.6 kJ/(mol H_2) [35] yielding an equilibrium temperature of 230 °C at normal pressure, still too high for on-board applications. Nevertheless the amide decomposition reaction is under deep scrutiny since this material represents a prototypical, relatively simple system, which could shed light on the mechanisms of reversible H-release in the more complex, and more promising, reactive hydrides made of mixtures of amide, borohydrides and/or alanates (e.g. $LiNH_2/LiBH_4$ or $LiNH_2/NaAlH_4$) [10].

A substantial amount of work has been done to unravel the detailed mechanism of the amide decomposition but is still a matter of debate (LiH alone decomposes into H and metallic Li at 500 °C). P. Chen *et al.* [9, 12] originally suggested that H_2 release could take place at the $LiNH_2/LiH$ interface via an acid-base reaction between $H^{\delta-}$ of LiH and $H^{\delta+}$ of Li amide

$$LiNH^{\delta+}H^{\delta+} + LiH^{\delta-} \longrightarrow Li_2NH + H_2\,.$$

They performed an isotopic labeling experiment in which a mixture of $LiNH_2$ and LiD was considered [12]. If the premise was correct combining $D^{\delta-}$ from the deuterated hydride and $H^{\delta+}$ from the amide, a predominantly gaseous HD (instead of a H_2 molecule for completely hydrogenate samples) should be detected. In fact, the evolved gas consisted of mostly H_2 as well as HD and D_2. Hence, the original idea of a solid-solid reaction

at the interface between $LiNH_2$ and LiH could not explain this isotopic distribution. Furthermore, such a mechanism would require very close contact between the two phases which is hampered by the large mismatch in the lattice parameters of the two phases.[2] On the other hand $LiNH_2$ alone is known to decompose into Li_2NH releasing ammonia as

$$2\,LiNH_2 \longrightarrow Li_2NH + NH_3\,. \tag{2.3}$$

It is also known that NH_3 reacts very fast with LiH according to

$$NH_3 + LiH \longrightarrow LiNH_2 + H_2\,. \tag{2.4}$$

It is therefore conceivable that reaction (2.2) might actually consist of the two steps (2.3) and (2.4).

Indeed, Ichikawa *et al.* [13] reported evidence that reaction (2.2) is mediated by ammonia [36]. They observed that, contrary to previous experiments, the desorption reaction in the mixture $LiNH_2$ / LiH leads to evolution of a significant amount of ammonia when a mixture of 1:1 ratio is used. Interestingly, they observed that the quantity of detected ammonia decreases if $LiNH_2$ and LiH are ball milled (*i.e.* intimately mixed) and/or if the mixture ratio moves from 1:1 to 1:2 ($LiNH_2 + x$LiH with $1 < x < 2$), with vanishing amount of ammonia when $x = 2$ (as observed in the overall LiN_3–Li_2NH–$LiNH_2$ cycle).

Reaction (2.4) is very fast [37, 14] so that in the presence of LiH, ammonia is detectable by mass-spectroscopy analysis only at low temperatures and low hydrogen pressures [33]. Hence the first step (2.3) is rate-determining. The two-step process for amide decomposition was substantiated by isotopic labeling experiments by Ichikawa *et al.*, the ratio between the released HD, H_2 and D_2 molecules being consistent with an ammonia mediated process [15]. The ammonia mediated reaction would consist of successive steps of decomposition of Li amide according to

$$\begin{aligned}
LiNH_2 + LiH &\longrightarrow \frac{1}{2}LiH + \left(\frac{1}{2}LiH + \frac{1}{2}NH_3\right) + \frac{1}{2}Li_2NH \\
&\longrightarrow \frac{1}{2}LiH + \frac{1}{2}LiNH_2 + \frac{1}{2}Li_2NH + \frac{1}{2}H_2 \\
&\longrightarrow \frac{1}{4}LiH + \frac{1}{4}LiNH_2 + \left(\frac{1}{2}+\frac{1}{4}\right)Li_2NH + \left(\frac{1}{2}+\frac{1}{4}\right)H_2 \\
&\cdots \\
&\longrightarrow \frac{1}{2^n}LiH + \frac{1}{2^n}LiNH_2 + \sum_{k=1}^{n}\frac{1}{2^k}Li_2NH + \sum_{k=1}^{n}\frac{1}{2^k}H_2 \\
&\longrightarrow Li_2NH + H_2\,.
\end{aligned} \tag{2.5}$$

The two steps decomposition process is supported by thermogravimetric analysis (TGA), IR spectroscopy and isotopic labeling experiments [13, 15].

[2] The epitaxial growth of Li_2NH on LiH is disfavored by the lattice mismatch. In the $Fm\bar{3}m$ phase of Li_2NH the Li atoms form a sc sublattice of edge $a = 2.52$ Å which is longer than the edge of the Li fcc sublattice in LiH ($a = 2.042$ Å).

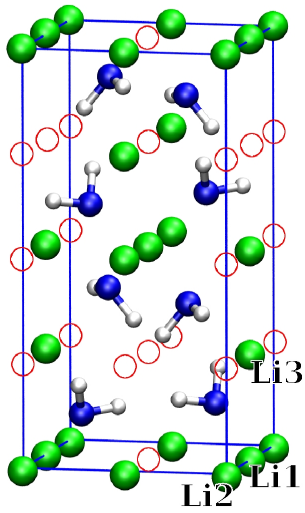

Figure 2.1: Crystal structure of $LiNH_2$. The conventional tetragonal unit cell is shown (eight formula units). Large green spheres represent Li atoms, small white spheres hydrogen atoms and blue spheres nitrogen. Vacancies of Li in the ideal anti-fluorite structure are depicted by empty circles. The Li atoms independent by symmetry are labeled.

Other experimental works on the $LiNH_2$ / LiH system report on the possibility of improving by ball milling to reduce particles size [32, 38, 39, 40] or by addition of potential catalysts to reduce desorption temperature [36, 41, 42]. A different and pioneering "additive" strategy was proposed by Nakamori and Orimo in which the additives were not so much acting as catalyst but as dopant [43, 44]. In practice, the partial substitution of Li^+ cations with other light but more electronegative elements then Li weakens the otherwise strong covalent bond between hydrogen and nitrogen and allows the formation of an intermediate compound with lower enthalpy. In such a way the temperature of decomposition is lowered. These studies opened a new branch of research together with a new families of complex amides/imides and other composite systems. Such new systems share chemical and physical properties with the "simpler" $LiNH_2$/LiH mixture, as already observed in the mixture $Mg(NH_2)_2$ / LiH in which an ammonia mediated decomposition pathway has been proposed [16].

2.2 Crystal structure of $LiNH_2$

Lithium amide, $LiNH_2$, is an ionic compound formed by Li^+ cations and NH_2^- anionic group and historically it was used primarily in organic synthesis. Preparation of the compound and earliest studies of the $LiNH_2$ were reported by Titherley in 1894 [48]. $LiNH_2$ was synthesized by the exothermic reaction between metallic lithium and gaseous

Table 2.2: Experimental neutron data of structural properties of $LiNH_2$ crystal [45]. Theoretical *ab initio* calculations, here reported in parentheses, are in very good agreement with experiments [46, 47]. See Fig. 5.1 for the labeling of atoms independent by symmetry.

lattice parameters [Å]		$a = 5.03442(24)$ ($a = 5.079$)		
		$c = 10.25558(52)$ ($c = 10.113$)		
	atomic parameters			
atom	position	x	y	z
Li1	$2a$	0 (0)	0 (0)	0 (0)
Li2	$2c$	0 (0)	1/2 (1/2)	1/4 (1/4)
Li3	$4f$	0 (0)	1/2 (1/2)	0.00253 (0.0018)
N	$8g$	0.2286 (0.2253)	0.2499 (0.2480)	0.1158 (0.1155)
H1	$8g$	0.2429 (0.2392)	0.1285 (0.1337)	0.1910 (0.1999)
H2	$8g$	0.3840 (0.3949)	0.3512 (0.3603)	0.1278 (0.1198)

or liquid ammonia following the reaction

$$2\,Li + 2\,NH_3 \longrightarrow 2\,LiNH_2 + H_2 \tag{2.6}$$

In his studies, Titherley showed that the ionic compound melts at temperatures between 373 and 375 °C and decomposes to imide and ammonia and eventually into lithium nitride, Li_3N. A partial solution of the crystal structure, in which H atoms were not located, was presented in 1951 by Juza and Opp [49] but only 21 years later Jacobs and Juza performing single crystal X-ray diffraction experiments (XRD) definitely solved the problem. The $LiNH_2$ structure is an ordered anti-fluorite derivative belonging to the tetragonal space group $I\bar{4}$ with nitrogen in a cubic close packed arrangement and lithium in tetrahedral interstices as depicted in Fig. 2.1. Furthermore, by inspection of its IR spectrum lithium amide exhibits two sharp bands corresponding to N–H stretches at 3260 cm^{-1} and 3315 cm^{-1} [35]. A subsequent experimental study with higher resolution obtained by using powder neutron diffraction (PND) experiments on deuterated samples, $LiND_2$ [50], showed N–D bond lengths longer by approximately 0.2 Å compared to reported XRD experiments (XRD assigned $d_{N-H} \sim 0.7$Å [49]). The same result was obtained later by two more PND experiments [45, 51] on both hydrogenated and deuterated samples which confirmed the longer N–H(D) bond length (PND on $LiNH_2$: $d_1 \sim 0.99$ Å, $d_2 \sim 0.94$ Å, ∠H–N–H = 99.97° [45]; PND on $LiND_2$: $d_1 \sim 0.97$ Å, $d_2 \sim 0.98$ Å, ∠D–N–D = 104.0(7)° [51]).

2.3 Crystal structure of Li_2NH

Lithium imide, Li_2NH, forms via decomposition of lithium amide at high temperature under vacuum (see Eq. (2.7)) or by reaction between ammonia and lithium hydride (Eq. (2.8)) [52, 53]

$$2\,LiNH_2 \longrightarrow Li_2NH + H_2 \tag{2.7}$$

$$2\,LiH + NH_3 \longrightarrow Li_2NH + 2\,H_2\,. \tag{2.8}$$

For this compound a structural reversible phase transition was observed by differential thermal analysis (DTA) [54] at $T_{dis} = 353(3)$ K and identified as an order–disorder transition We will refer hereafter to the two distinct crystal structure of Li_2NH as the low-temperature (LT) and high-temperature (HT) phases. In fact, combinations of ^7Li and ^1H solid-state NMR experiments by Haigh *et al.* clearly showed different properties of the imide above and below this transition temperature [55].

The first proposal for the structure of Li_2NH at room temperature (LT phase) was suggested in 1951 by Juza and Opp [49] from X-ray diffraction. Here the Li_2NH LT phase was identified as an anti-fluorite structure isomorphous with lithia, Li_2O, with a $Fm\bar{3}m$ space group. Here NH groups occupy the fcc sites with disordered orientations and Li^+ ions occupy the tetrahedral interstitial sites of the fcc. Due to the importance of this compound for H-storage its crystal structure has been revisited more recently by modern experimental means with the aim of determining the positions of the hydrogens. In 2005 powder neutron diffraction experiments (PND) at room temperature by Ohoyama *et al.* [56] confirmed the anti-fluorite structure for N and Li atoms. Concerning the

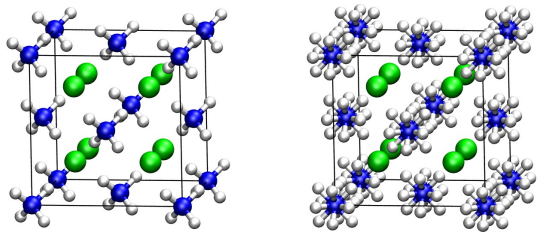

(a) (b)

Figure 2.2: (a) $F\bar{4}3m$ crystal structure of Li_2NH in which H atoms occupy the $16e$ sites with occupation $f = 1/4$ [56]. (b) $Fm\bar{3}m$ crystal structure in which H atoms occupy the $48h$ sites with occupation $f = 1/12$ [59].

positions of H atoms two space group have been proposed on the basis of Rietveld analysis [57, 58]: $Fm\bar{3}m$ and $F\bar{4}3m$ which equally fit the experimental data. H atoms occupy in a disordered manner (either static or dynamic) the $16e$ equivalent positions assigned in the $F\bar{4}3m$ structure with an occupation $f = 1/4$.

A $Fm\bar{3}m$ space group was later confirmed by Noritake *et al.* [59] from X-ray powder diffraction data. Here hydrogen atoms were placed randomly over 4 of the $48h$ sites (with occupation $f = 1/12$) with a N–H bond length of 0.80(16) Å. This N–H bond length is shorter than the N–H bond length in organic molecules (as obtained from X-ray and neutron diffraction data respectively 0.930 and 1.032 Å [60]). This discrepancy in the N–H bond length was ascribed to the disordered structure.

More recently, Balogh *et al.* [11] performed X-ray and neutron diffraction experiments on a fully deuterated compound Li_2ND which provided better resolution due to the higher scattering neutron cross section of deuterium. Neutron diffraction experiments at low (100, 200 and 300 K) and high (400 K) temperatures confirmed the structural phase transition detected in 1950's and was apparently overlooked in more recent works [11, 56].

It turned out that the anti-fluorite structure with a $Fm\bar{3}m$ symmetry could be assigned only to the high temperature phase (400 K) where hydrogen atoms were placed randomly on the $192l$ sites with the more plausible N–H bond length of 1.0 Å (see Fig. 2.3(b)). These results have been confirmed both by X-ray and neutron diffraction data [11].

At low temperature (100 K, 200 K and 300 K) the diffraction data were best fitted by a cubic crystal with $Fd\bar{3}m$ space group. The LT crystal was described as a superstructure of the anti-fluorite phase in which one out of 8 Li atoms is displaced to an interstitial site giving rise to Li vacancies arranged in a ordered manner and tetrahedrally coordinated to four NH groups (see Fig. 2.4). The structure is stabilized by electrostatic interaction of $H^{\delta+}$ pointing towards the Li^+ vacancy which is formally a negatively charged site. Similar tetrahedral arrangement of four NH groups was later identified also in other imides, such as $Li_2Mg(NH)_2$ [61]. In the LT phase, H and N atoms occupy $32e$ sites. Li atoms are distributed over three different sites (cf. Fig. 2.5): $48f$ (Li1), $8a$ (Li2) and $32e$ (Li3).

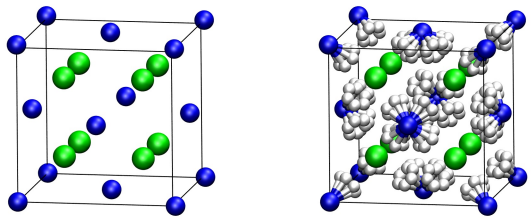

(a) (b)

Figure 2.3: (a) Basic anti-fluorite crystal structure (anions blue spheres, cations green spheres). (b) $Fm\bar{3}m$ high temperature anti-fluorite structure suggested for Li_2NH by Balogh *et al.* [11]. N atoms (blue spheres) occupy the fcc sites and Li atoms (green spheres) occupy the tetrahedral sites of the fcc. H atom are placed over the 192l sites with occupation $f = 0.0208$.

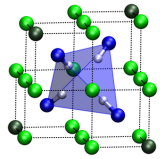

Figure 2.4: Li vacancy in a 8b site coordinated tetrahedrally by four NH groups.

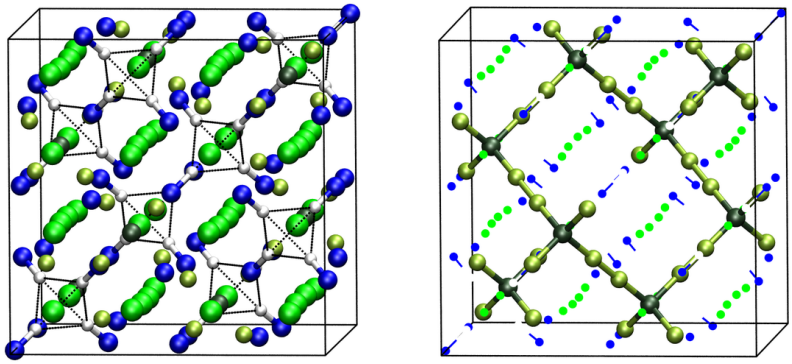

(a) $Fd\bar{3}m$ crystal structure (b) Li2 and Li3 interstitials arrangement

Figure 2.5: Disordered cubic LT $Fd\bar{3}m$ crystal structure for Li_2NH suggested by Balogh *et al.* [11]. (a) Li-vacancies, placed at 8b sites, tetrahedral coordinated by 4 ND (4 NH) groups are outlined (cf. also Fig. 2.4). (b) Each Li at 8a site (Li2) is tetrahedral coordinated by four 32e sites partially occupied by Li interstitial atoms (Li3). Legend: ● Blue = N, ○ Wihte = H/D, ● (Green) = Li1 lithium atoms placed at 48f sites, ● (Dark Green) = Li2 lithium atoms placed at 8a sites, ● (Light Green) = Li3 lithium atoms placed at 32e sites.

The Li3 site corresponds to a displacement along ⟨111⟩ directions from the octahedral position (sites 16*c* of the $Fd\bar{3}m$ space group). According to Rietveld refinement, the latter has a fractional occupation of about 1/3 at low temperatures which gets closer to the value required by stoichiometry (1/4) only at room temperature. A supercell showing the position of Li1, Li3 and of Li^+ vacancies coordinated tetrahedrally by four NH groups is shown in Fig. 2.5(a). In Fig. 2.5(b) the positions of Li2 and Li3 are highlighted.

Starting from the cubic disordered crystal structure, $Fd\bar{3}m$ reported by Balogh *et al.* Herbst and Hector [11, 34] attempted to model an ordered structure by fully occupying selected 32*e* Li3 sites. In this structure a single Li^+ ion is present around each Li2 site (cf. Fig. 2.7(a)) resulting in an $Ima2$ symmetry (see Fig. 2.6). The relationship between the unit cell of $Ima2$ and the conventional unit cell of $Fd\bar{3}m$ is shown in Fig. 2.6(a). However, by optimizing this structure by first principles calculations, (DFT), the interstitial atoms move to the octahedral positions 16*c* giving rise to a $Imma$ space group with 16 formula units per unit cell. The 16*c* octahedral sites will be referred hereafter as sites Li4. Fig. 2.7 shows the local arrangement of a Li2 and Li interstitial before geometry optimization (fig. 2.7(a), $Ima2$ space group Li interstitial in Li3 position) and after (fig. 2.7(b), $Imma$ space group Li interstitial in Li4 position). In Fig. 2.7(a) transparent spheres indicate the empty interstitial 32*e* sites of the $Fd\bar{3}m$ space group.

The relaxed structure obtained by Herbst and Hector with $Imma$ symmetry will be referred to hereafter as the HH phase (the optimized positions are compared with experimental data in Tab. 4.1 in section 4.1). The positions of Li interstitials at Li4 sites are, however, incompatible with Rietveld refinement. This is apparent from the theoretical positions given in Refs. [11, 34, 62] but was not properly addressed in these works. Moreover, the theoretical formation energy of this phase is too high when compared to experimental data. Thus, alternative proposals, based on *ab initio* calculations, have appeared in literature which suggest ordered models for the LT phase of Li_2NH. These predicted structures are lower in energy and symmetry and are also predominantly orthorhombic (cf. also Tab. 4.4).

In Fig. 2.8 we report the unit cells of the theoretical orthorhombic crystal structures $Pnma$ and $Pbca$ [63, 64] together with their structural parameters. In the $Pnma$ phase all atoms occupy the 4*c* sites (see Fig. 2.8) in a distorted anti-fluorite lattice. Here N–H units are orientated in an anti-parallel way along the ⟨001⟩ directions. The $Pbca$ phase (see Fig. 2.8) is the lowest in energy with N, H and two inequivalent Li atoms occupying 8*c* (*x*, *y*, *z*) positions [64]. The lithium atoms in this model have moved significantly from their ideal anti-fluorite positions and N–H units adopt preferred orientations with respect to their nearest neighbours. Although both structures in the $Pnma$ and $Pbca$ space group are lower in energy (cf. Tab. 4.4) than the $Imma$ phase the latter gives the best fit of the experimental data. However the positions of the interstitial atoms in the $Imma$ phase are inconsistent with the experimental data. In chapter 4 we will present our proposal, based on *ab initio* calculations, for an alternative structure for the LT phase which is in very good agreement with neutron diffraction data hence solving the inconsistencies of previous models.

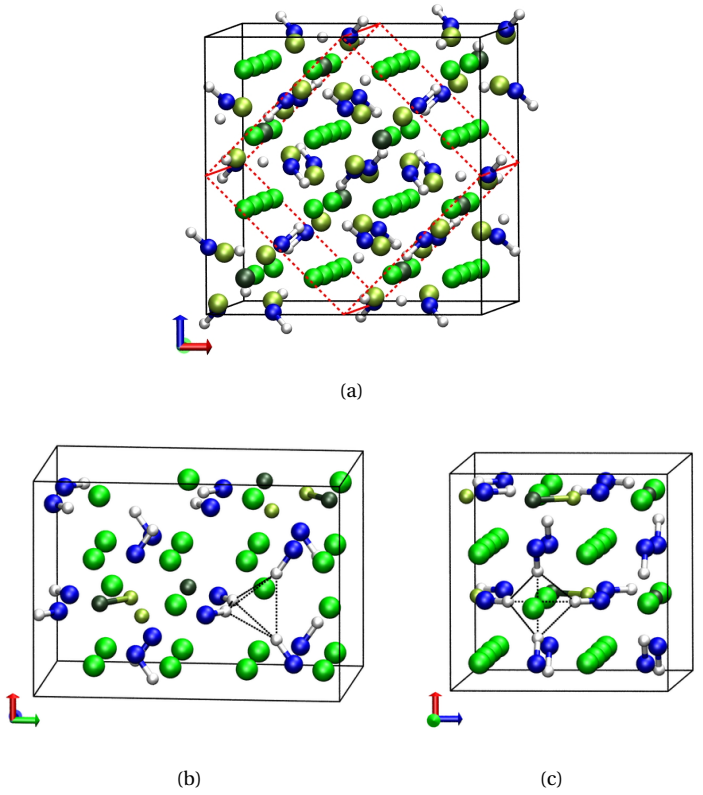

Figure 2.6: (a) Relationship between the conventional cell of $Fd\bar{3}m$ and the unit cell of $Imma$ highlighted in the picture by dotted lines. (b), (c) Two different views of the orthorhombic fully occupied $Imma$ structure for the LT phase of Li_2NH. The volume is twice that of the unit cell of the $Fd\bar{3}m$ structure ($a\sqrt{2}/2 \times a \times a\sqrt{2}/2$). A Li vacancy tetrahedrally coordinated by 4 ND (4 NH) groups is outlined (see also Fig. 2.5 for comparisons).

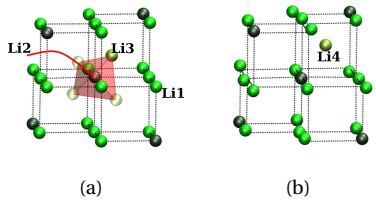

Figure 2.7: Position of Li in (a) $Ima2$, Li3 near to a Li2 atom (transparent spheres indicate the three unoccupied Li3 sites). (b) Upon geometry optimization Li interstitials are displaced from Li3 to Li4 octahedral sites with subsequent change in symmetry from $Ima2$ to $Imma$.

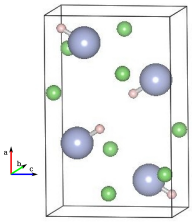

(a) *Pnma*

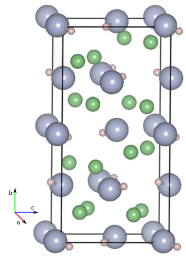

(b) *Pbca*

$a = 7.733$ Å, $b = 3.6$ Å, $c = 4.872$ Å

atom	x	y	z
Li1 (4*c*)	0.102	1/4	0.464
Li2 (4*c*)	0.201	1/4	-0.086
N (4*c*)	0.354	1/4	0.218
H (4*c*)	0.424	1/4	0.399

$a = 5.12$ Å, $b = 10.51$ Å, $c = 5.27$ Å

atom	x	y	z
Li1 (8*c*)	0.372	0.540	0.651
Li2 (8*c*)	0.480	0.256	0.191
N (8*c*)	0.297	0.370	0.451
H (8*c*)	0.363	0.610	0.066

Figure 2.8: Theoretical orthorhombic (a) *Pnma* [63] and (b) *Pbca* [64] crystal structures. Large, medium and small spheres represent nitrogen, lithium, and small hydrogen.

Table 2.3: Theoretical free energy of the different structures proposed for the LT phase of Li_2NH. Zero-point energy and phononic contribution to the entropy have been included (see also Ref. [62]).

Li_2NH structure	**Space group**	$\Delta F_{@298K}$ **[kJ mol^{-1} f.u.$^{-1}$]**
Herbst and Hector (HH)	*Imma*	0.0
Magyari-Kope *et al.* (MOW)	*Pnma*	-1.4
Mueller and Ceder (MC)	*Pbca*	-3.8

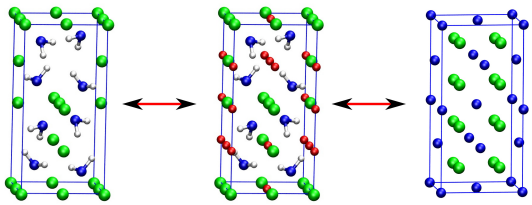

Figure 2.9: Continuous transformation from $LiNH_2$ to Li_2NH through sub-stoichiometric phases as observed from synchrotron X-ray diffraction data [17].

2.4 Mechanism of decomposition reaction

As discussed in section 2.1 Ichikawa *et al.* [13] provided evidence that the dehydrogenation of $LiNH_2$ is mediated by NH_3 according to

$$2\,LiNH_2 \longrightarrow Li_2NH + NH_3 \tag{2.9}$$

$$NH_3 + LiH \longrightarrow LiNH_2 + H_2\,. \tag{2.10}$$

The evolution of ammonia, reaction (2.9), is the rate-limiting step since reaction between ammonia and lithium hydride, reaction (2.10), is very fast [14]. The rehydrogenation reaction

$$H_2 + Li_2NH \longrightarrow LiNH_2 + LiH \tag{2.11}$$

is instead assumed to proceed without the NH_3 intermediate although rehydrogenation has been less studied than dehydrogenation.

David *et al.* [17] investigated further the amide/imide transformation by means of time resolved synchrotron XRD during the dehydrogenation / rehydrogenation cycles. They found that both hydrogenation and dehydrogenation occur through non-stoichiometric phases according to

$$Li_{1+x}NH_{2-x} \longrightarrow (1-\epsilon)Li_{1+y}NH_{2-y} + \epsilon NH_3 \tag{2.12}$$

where $(1+y)(1-\epsilon)=(1+x)$. These intermediate sub-stoichiometric phases are based on the cubic anti-fluorite crystal structure (cf. Fig. 2.9). This outcome suggested a model for the dehydrogenation / hydrogenation reactions based on a mobility of the H^+ and Li^+ charged species and the formation of NH_3 promoted by Li Frenkel pairs. Therefore, first a Frenkel pair gives rise to two adjacent charged complexes $[LiLiNH_2]^+$ and $[\square NH_2]^-$ (where $\square$ is a Li vacancy). Second, the cation complex releases a proton which reacts with the anionic complex forming ammonia [17]

$$LiNH_2 + LiNH_2 \longrightarrow [LiLiNH_2]^+[\square NH_2]^- \tag{2.13}$$

$$[LiLiNH_2]^+[\square NH_2]^- \longrightarrow Li_2NH + NH_3\,. \tag{2.14}$$

On the other hand a different mechanism has been suggested by means of kinetics measurements considering the effect on a ball milled sample [18, 38]. Earlier studies

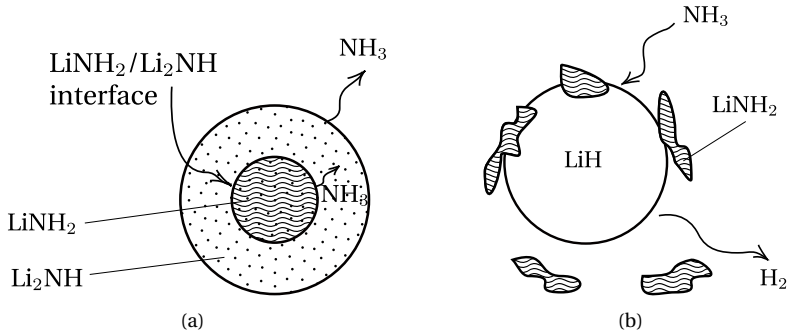

Figure 2.10: Sketch of the decomposition path of the $LiNH_2$ + LiH mixture according to Ref. [18]. (a) $2LiNH_2 \rightarrow Li_2NH + NH_3$ takes place via the growth of a shell of Li_2NH outside a shrinking $LiNH_2$ core accompanied by ammonia desorption. (b) NH_3 reacts with LiH releasing H_2 and forming $LiNH_2$ which flakes off incessantly from the LiH surface.

by Markmaitree *et al.* [38] shows that the onset temperature for $LiNH_2$ decomposition is reduced depending on how intimately $LiNH_2$ and LiH were mixed. The enhanced decomposition via ball milling is attributed to the reduced particle size and a decreased activation energy. The more mechanical activation will enhance the decomposition rate of $LiNH_2$. Later Shaw *et al.* [18] performed kinetics experiments on ball milled $LiNH_2$/LiH sample with a ratio of 1:1.1. The 10% excess of LiH was added to minimize the loss of NH_3 during the dehydrogenation process. The evolution of hydrogen during isothermal measurements has been monitored and different kinetics models have been used to fit the experimental data.

On the basis of their kinetic analysis Shaw *et al.* proposed that reaction (2.9) proceeds via the growth of a shell of the Li_2NH product on the surface of a shrinking core of the $LiNH_2$ reactant as sketched in Fig. 2.10. The good lattice parameters matching and the similarity of the Li sublattices in $LiNH_2$ and Li_2NH would favor epitaxial growth of the two phases. In the presence of LiH, the ammonia released at the Li_2NH surface would then react with lithium hydride giving rise to the formation of a $LiNH_2$ shell at the surface of LiH [18]. The large mismatch in the lattice parameters of LiH and $LiNH_2$ hinders instead a massive growth of the $LiNH_2$ shell on LiH which flakes off continuously providing new LiH surface for the fast reaction with NH_3 [18]. In fact, in the $Fm\bar{3}m$ phase of Li_2NH the Li atoms form a simple cubic lattice of edge $a = 2.55$ Å which is much longer than the edge of the Li fcc sublattice in LiH ($a = 2.042$ Å) [18, 38, 65, 66]. Following the proposal by Shaw and coworkers reaction (2.9) is the result of three elementary steps:

- formation of NH_3 in bulk or at the $LiNH_2$ / $LiNH_2$ interface
- diffusion of NH_3 inside Li_2NH
- desorption of NH_3 from the surface of Li_2NH

The evolution of NH_3 (or H_2 in the whole $LiNH_2 + LiH \longrightarrow Li_2NH + H_2$ reaction, since

reaction (2.10) is very fast) with time is best fitted by assuming that the rate limiting step consists of the diffusion of NH_3 in Li_2NH which leads to the following time dependence of the fraction, f, of released H

$$(1-f)^{1/3} = 1 - \frac{k^{1/2}}{R} t^{1/2} . \tag{2.15}$$

In the above equation R is the size of the crystallites and k is the rate constant.

The continuous decomposition pathways of reaction (2.12) and the core-shrinking model proposed in Ref. [18] seem to provide conflicting scenarios for the decomposition of $LiNH_2$. However, different transformation pathways might actually correspond to different preparation conditions of the material. In fact, the $LiNH_2/LiH$ mixture used in the kinetic measurements of Ref. [18] was ball-milled while the samples used in the X-ray diffraction measurements [17] were not.

3

Methods and computational approach

3.1 The many-body problem

Understanding and predicting properties without relying on experimental data has been the aim of first-principles calculations since their advent about 80 years ago. All the information about a system composed of N electrons and M nuclei can in principle be obtained from the many-body Schrödinger equation. Its time-independent, non-relativistic version is given by

$$H\Psi(\mathbf{r}_i, \mathbf{R}_j) = E\Psi(\mathbf{r}_i, \mathbf{R}_j)\,. \tag{3.1}$$

H is the many-body Hamilton operator providing the total energy of the system when applied to the many-body wave-function $\Psi(\mathbf{r}_i, \mathbf{R}_j)$ that depends on the nuclear positions $\mathbf{R}_j$ and the electron coordinates $\mathbf{r}_i$. The Hamiltonian itself has five main contributions: the kinetic energy operators T_n and T_e of the nuclei and the electrons respectively, the electron-electron interaction V_ee, the repulsion of the nuclei V_nn and the electrostatic interaction between the electrons and the nuclei V_ne

$$H = T_\mathrm{n} + T_\mathrm{e} + V_\mathrm{ee} + V_\mathrm{nn} + V_\mathrm{ne}\,. \tag{3.2}$$

In atomic units the components of the Hamiltonian operator are

$$T_{\mathrm{n}} = -\frac{1}{2}\sum_{j=1}^{M}\frac{1}{m_j}\nabla_j^2\,, \tag{3.3a}$$

$$T_{\mathrm{e}} = -\frac{1}{2}\sum_{i=1}^{N}\nabla_i^2\,, \tag{3.3b}$$

$$V_{\mathrm{ee}} = \sum_{i=1}^{N}\sum_{j>i}^{N}\frac{1}{|\mathbf{r}_i-\mathbf{r}_j|}\,, \tag{3.3c}$$

$$V_{\mathrm{nn}} = \sum_{i=1}^{M}\sum_{j>i}^{M}\frac{Z_iZ_j}{|\mathbf{R}_i-\mathbf{R}_j|}\,, \tag{3.3d}$$

$$V_{\mathrm{ne}} = \sum_{i=1}^{N}\sum_{j=1}^{M}\frac{-Z_j}{|\mathbf{r}_i-\mathbf{R}_j|}\,, \tag{3.3e}$$

where m_j is the mass of nucleus j in multiples of the electron mass, Z_j the nucleus charge and ∇_i^2 the Laplacian operator acting on particle i.

The difficulty in solving Eq. (3.1) arise from the large number of variables that the many-body wave-function depends on. In fact, for a system consisting of N electrons and M nuclei there are $3N+3M$ degrees of freedom, *i.e.* three spatial coordinates for each electron and for each nucleus.

A first simplification can be achieved by taking into account the large difference in masses between electrons and nuclei. Therefore, the electrons move much faster than the nuclei and a good approximation is to consider a parametric dependence of the wave-function on the nuclei positions. In this way the motion of the electrons is separated from the motion of nuclei, which now represent an "external" potential to the electrons. The kinetic energy of nuclei can be set to zero and the nuclear-nuclear repulsion term enters into the total energy expression as a constant. This is the so called Born-Oppenheimer approximation (BOA). Even though the number of degrees of freedom has now been reduced to $3N$, the remaining electronic many-body problem is not solvable exactly except for the simplest cases. The remaining electronic Hamiltonian reads [67]

$$H_{\mathrm{e}} = T_{\mathrm{e}} + V_{\mathrm{ee}} + V_{\mathrm{ne}} = -\frac{1}{2}\sum_{i=1}^{N}\nabla_i^2 + \sum_{i=1}^{N}\sum_{j>i}^{N}\frac{1}{|\mathbf{r}_i-\mathbf{r}_j|} - \sum_{i=1}^{N}\sum_{j=1}^{M}\frac{Z_j}{|\mathbf{r}_i-\mathbf{R}_j|} \tag{3.4}$$

with the electronic Schrödinger equation

$$H_{\mathrm{e}}\Psi_{\mathrm{e}}(\mathbf{r}_i) = E_{\mathrm{e}}\Psi_{\mathrm{e}}(\mathbf{r}_i) \tag{3.5}$$

where $\Psi_{\mathrm{e}}(\mathbf{r}_i)$ is the electronic wave-function. The first numerical scheme to solve this equation quantitatively to obtain an approximate wave-function and the total energy was suggested by Hartree and Fock [68, 69] in the 1930's. Since the introduction of the Hartree-Fock (HF) method wave-function based techniques have undergone enormous development [70, 71].

However, since is formulation Density Functional Theory (DFT) represents a very powerful alternative method. In fact, it is based on the electron density which is now

the central quantity instead of the wave-function. It is becoming a very popular and successful quantum mechanical approach to solve the many-body problem [72, 73].

3.2 Density Functional Theory

The electron density was used for the first time to calculate the total energy of a system by Thomas and Fermi in the late 1920's. The electron density ρ is defined as the integral of the many-body wave-function over all but one spatial coordinates of all electrons multiplied by the number of electrons

$$\rho(\mathbf{r}) = N \int \dots \int |\Psi(\mathbf{r}, \mathbf{r}_1, \mathbf{r}_2, \dots, \mathbf{r}_N)|^2 d\mathbf{r}_1, \dots, d\mathbf{r}_N \tag{3.6}$$

where $\mathbf{r}$ refers to the spatial coordinates of the density and the $\mathbf{r}_i$ to the coordinates of the individual electrons. In contrast to the wave-function, the electron density ρ is an observable and contains all information required to define the system. The integral of the density over the spatial coordinate, $\int \rho d\mathbf{r}$ gives the total number of electrons in the system, N.

Early on, Thomas and Fermi tried to express the energy of a system as a function of the electron density [74]. This approach leads to a reduction from $3N$ to 3 coordinates. The energy is given by the Thomas-Fermi kinetic energy functional which depends only on the density in addition to classical terms for the electron-electron and electron-nucleus interactions. The energy is minimized with respect to the density to obtain the ground state energy of the system.

However, for many-electron atoms and many-atom systems the results were not very satisfying. Some molecules are unstable using the Thomas-Fermi approach. This was because the sum of the energies of the isolated atoms is lower than the energy of the molecule. This is because in the Thomas-Fermi model, exchange and correlation effects are completely neglected and the kinetic energy is approximated by the kinetic energy of non-interacting electrons in a homogeneous electron gas. In 1930 Dirac added an expression which took into account the exchange energy depending only on the density. However electron correlations were again completely neglected.

Nevertheless, this model is historically very important, because it was the first example in which an expression for the energy was established using exclusively the electron density as the basic variable.

In 1964 the density functional theory was established by two theorems of Hohenberg and Kohn [75], who demonstrated that the ground state density can indeed be used to replace the complex wave-function.

They have given a simple proof of the fact that for an electron system feeling the external potential V_{ext} "*V_{ext} is (within a constant) a unique functional of ρ; since, in turn, V_{ext} fixes H we see that the full many-particle ground state is a unique functional of ρ*" [75]. Hence the density uniquely defines the Hamiltonian operator and therefore the energy of the system. Accordingly, the electronic ground state energy E_0 can be written as a functional of the ground state density ρ_0

$$\begin{aligned} E_0 = E[\rho_0] &= T_{\text{e}}[\rho_0] + E_{\text{ee}}[\rho_0] + E_{\text{ne}}[\rho_0] \\ &= F_{\text{HK}}[\rho_0] + E_{\text{ne}}[\rho_0] \,. \end{aligned} \tag{3.7}$$

This equation defines the Hohenberg-Kohn functional, $F_{\mathrm{HK}}[\rho_0]$, which is independent of the system, *i.e.* it is *universal*, but unfortunately no exact expressions for its components $T_{\mathrm{e}}[\rho]$ and $E_{\mathrm{ee}}[\rho]$ are known. However, $E_{\mathrm{ee}}[\rho]$ can be written as a sum of the Hartree energy $E_{\mathrm{H}}[\rho]$, which is the interaction of a charge distribution with itself

$$E_{\mathrm{H}}[\rho] = \frac{1}{2}\int \frac{\rho(\mathbf{r})\rho(\mathbf{r}')}{|\mathbf{r}-\mathbf{r}'|}\,d\mathbf{r}d\mathbf{r}' \tag{3.8}$$

and a non-classical part $E_{\mathrm{ncl}}[\rho]$, which contains the self-interaction correction, the exchange and the Coulomb correlations. In summary, there is a one-to-one correspondence between the external potential and the ground state density of a system. Consequently, the expectation value of any observable is also a unique functional of the exact ground state electron density. This is often called the first Hohenberg-Kohn theorem.

The second Hohenberg-Kohn theorem states that the energy is minimal for the ground state density resulting from the external potential. This enables the use of the variational principle to calculate the exact ground state density if the energy functional is known. Any density different from the ground state density yields a higher total energy than the *true* ground state one. However, it should be noted that the functional $F_{\mathrm{HK}}[\rho]$ is not known and instead approximations have to be used. As a consequence, within the given approximation for $F_{\mathrm{HK}}[\rho]$, the variational principle can only be used to find the ground state density and its corresponding energy for this functional form of $F_{\mathrm{HK}}[\rho]$.

In 1965, once DFT was finally established, Kohn and Sham developed a scheme for its practical applications introducing the concept of a non-interacting reference system [76]. Using this approach it is not required to use the unknown kinetic energy density-functional $T_{\mathrm{e}}[\rho]$. In fact, this latter term is separated into the kinetic energy T_{S} of a system of non-interacting electrons, which can be calculate exactly as

$$T_{\mathrm{S}} = -\frac{1}{2}\sum_{i}^{\mathrm{occ}}\int \varphi_i^*(\mathbf{r})\nabla^2\varphi_i(\mathbf{r})\,d\mathbf{r} \tag{3.9}$$

and the unknown component T_{C}, which contains the corrections resulting from the electronic interaction. The single particle Kohn-Sham orbitals φ_i are determined under the constraint to reproduce the ground state density of the fully interacting many-body system in a self-consistent way from the Kohn-Sham equations

$$H_{\mathrm{KS}}\,\varphi_i(\mathbf{r}) = \varepsilon_i\,\varphi_i(\mathbf{r}) \tag{3.10}$$

where the Kohn-Sham operator, H_{KS}, is an effective one-electron operator

$$\begin{aligned} H_{\mathrm{KS}} &= -\frac{1}{2}\nabla^2 + V_{\mathrm{ext}}[\rho] + V_{\mathrm{H}}[\rho] + V_{\mathrm{XC}}[\rho] \\ &= -\frac{1}{2}\nabla^2 + V_{\mathrm{eff}}[\rho]\,. \end{aligned} \tag{3.11}$$

$V_{\mathrm{ext}}[\rho]$ is the external potential due to the nuclei and it is often combined with the classical Hartree potential $V_{\mathrm{H}}[\rho]$ and the exchange-correlation potential $V_{\mathrm{XC}}[\rho]$ giving rise an effective potential $V_{\mathrm{eff}[\rho]}$. The eigenvalues ε_i are the Lagrange multipliers that ensure the orthonormality of the Kohn-Sham orbitals. The density constructed from the

Kohn-Sham orbitals φ_i and their occupation numbers f_i is the same as the density of the interacting system

$$\rho(\mathbf{r}) = \sum_{i}^{N} \varphi_i^*(\mathbf{r})\,\varphi_i(\mathbf{r})\,f_i \tag{3.12}$$

The φ_i are functionals of ρ and consequently the kinetic energy is still given as a functional of ρ in an indirect way. The remaining part T_C of the true kinetic energy is combined with the non-classical contributions to the electron-electron interaction $E_{ncl}[\rho]$ in the exchange-correlation functional $E_{XC}[\rho]$. Therefore, $E_{XC}[\rho]$ contains everything that is unknown and it is related to the exchange-correlation potential, $V_{XC}[\rho]$ in Eq. (3.11), by

$$V_{XC}[\rho(\mathbf{r})] = \frac{\delta E_{XC}[\rho(\mathbf{r})]}{\delta\rho(\mathbf{r})}\,. \tag{3.13}$$

The Kohn-Sham equations 3.10 replace the minimization of $E[\rho]$ by the solution of the single particle Schrödinger equations of non-interacting electrons. Here, the universal Hohemberg-Kohn functional is expressed in the form

$$F_{HK} = T_S + E_H + E_{XC} \tag{3.14}$$

and all the many-body effects are included in the E_{XC} term. It should be noted that the single particle orbitals φ_i are not the wave-functions of the electrons of the system, nor are the eigenvalues single-electron energies in a strict physical sense. Only the density and the total energy have a physical meaning. So far the Kohn-Sham equations do not contain any approximation and are in principle exact. However, the exact form of the exchange-correlation functional is still unknown. This is, of course, required to calculate the ground state density and energy.

3.2.1 Exchange-Correlation functionals

With the introduction of the Kohn-Sham formalism most contributions to the total energy can be calculated exactly. The remaining unknown parts are assembled in the exchange-correlation functional. Therefore, a good approximation to $E_{XC}[\rho]$ is crucial to obtain reliable results in a DFT calculation. Unfortunately, in contrast to wave-function methods there is no systematic way for more precise results to be obtained.

The first attempt to find an explicit expression for $E_{XC}[\rho]$ was based on the homogeneous electron gas. This is a uniform electron distribution on a positive background charge distribution for overall charge neutrality. The basic assumption is that exchange and correlation depend only on the local value of the density, namely the local density approximation (LDA). One approximates the real inhomogeneous electron density as a sum of small cells each of which has a homogeneous electron density. It is assumed that $E_{XC}[\rho(\mathbf{r})]$ at position $\mathbf{r}$ is identical to $E_{XC}^{LDA}[\rho(\mathbf{r})]$ of the homogeneous electron gas of the same density. The exchange-correlation functional is then given by

$$E_{XC}^{LDA}[\rho(\mathbf{r})] = \int \rho(\mathbf{r})\,\epsilon_{XC}(\rho(\mathbf{r}))\,d\mathbf{r} \tag{3.15}$$

where $\epsilon_{XC}(\rho(\mathbf{r}))$ is the exchange-correlation energy per particle of the homogeneous electron gas. E_{XC}^{LDA} can be further split into the exchange and the correlation contributions

E_X^{LDA}, E_C^{LDA}. The exchange part can be given analytically in the case of the homogeneous electron gas as

$$E_X^{LDA}[\rho(\mathbf{r})] = \int \rho(\mathbf{r}) \left(-\frac{3}{4}\right) \sqrt[3]{\frac{3\rho(\mathbf{r})}{\pi}}\, d\mathbf{r}\,. \tag{3.16}$$

On the other hand, the correlation energy is only numerically known from Monte Carlo calculations by Ceperley and Alder [77] and can be parameterized for use in DFT calculations.

Although the local-density approximation is a rather unrealistic model for real systems, it was the standard functional used until the 1990's. Results from its application are surprisingly good, comparable to Hartree-Fock for many systems. However, LDA typically overestimates binding energies and underestimates bond lengths. For systems with less homogeneous electron density the results using LDA are often disappointing. However the importance of LDA lies in the fact that the homogeneous electron gas is the only system for which the exchange-correlation functional in known and all improved functionals to date are based on this approach. Such improvements can be achieved by including the first derivative of the electron density $\nabla\rho(\mathbf{r})$ yielding the generalized gradient approximation (GGA) [72]. In this approximation $E_{XC}^{GGA}[\rho(\mathbf{r})]$ is given by

$$E_{XC}^{GGA}[\rho(\mathbf{r})] = \int f(\rho(\mathbf{r}), \nabla\rho(\mathbf{r}))\, d\mathbf{r}\,. \tag{3.17}$$

Including the gradient of the density results in much better binding energies compared to the LDA making GGA functionals the most important class of functionals in current DFT. Many GGAs exist differing in the functional form of exchange and correlation. In most cases GGA energies are more reliable than LDA results but, due to their non-unique definition there is typically a certain variation in the energies obtained from different GGA functionals. Nowadays, the development of new and better functionals is still an active field of research. E_{XC} is smaller in value than all other contributions to the total energy and usually density functional theory is used to calculate the energy difference between different systems. In this case the errors in the exchange-correlation energy often cancel to a large extent and this is the reason why approximations to E_{XC} lead to reliable results in most cases.

One of the most important functional forms for E_{XC}^{GGA}, which has been used in this work, has been proposed by Perdew, Burke and Ernzerhof in 1996 (PBE) [78]. The PBE functional has been constructed in a way to fulfill physical constraints rather than fitting to experimental data. The basic idea behind this functional was to mimic the PW91 functional of Perdew and Wang [79]. This is basically an analytical fit to a numerically determined first-principles GGA, but determines a simpler functional form by neglecting energetically irrelevant terms.

3.2.2 Applications in solid state theory

Crystalline solids and surfaces are characterized by an infinite number of atoms and their positions are related by certain symmetries inherent to the crystal structure. The only way to describe these systems within DFT is to make use of these symmetries in order to reduce the system size of the unit cell of the bulk solid or the surface by applying

periodic boundary conditions (PBC). The translational symmetry is taken into account in the construction of the Hamiltonian and the wave-functions by applying the Bloch theorem. This states that the wave function of a periodic system can be written as a product of a plane wave $e^{i\mathbf{k}\cdot\mathbf{r}}$ and a function with the lattice periodicity $u_{\mathbf{k}}(\mathbf{r})$

$$\varphi_{\mathbf{k}}(\mathbf{r}) = e^{i\mathbf{k}\cdot\mathbf{r}} u_{\mathbf{k}}(\mathbf{r}) \tag{3.18}$$

$$u_{\mathbf{k}}(\mathbf{r}) = u_{\mathbf{k}}(\mathbf{r}+\mathbf{T}) \tag{3.19}$$

where $\mathbf{k}$ is a wave vector within the first Brillouin zone (BZ) and $\mathbf{T}$ is a vector of the Bravais lattice. The one-electron wave-functions $\varphi_{\mathbf{k}}(\mathbf{r})$ are called Bloch functions.

To determine the total energy of a crystal a summation over the eigenvalues of the occupied single-particle states has to be performed. For periodic systems this sum over orbitals generalizes into an integration over the first BZ. By making use of the symmetries in the unit cell the integration over the first BZ can be further reduced to the integration of the irreducible part of the Brillouin zone. In practical calculations the integral is replaced by a summation over discrete points in reciprocal space [67], the k-points, which have to be as representative as possible for the whole Brillouin zone [80].

On the other hand, only a two dimensional periodicity could be used for a description of surfaces by density functional theory. In practice for surfaces the same procedure used for solids is applied. In fact, the surfaces are modeled by slabs, which consist of several layers of atoms of infinite extension in two dimensions by applying appropriate periodic boundary conditions. Additionally, the periodicity is artificially maintained also in the third dimension by infinitely repeating the slab in the direction perpendicular to the surface plane. This approach leads to two surfaces on both sides of the slab and one has to make sure that the slab is thick enough to avoid interactions between these surfaces. The interaction between surfaces and their periodic images are prevented by a large vacuum region. Ideally, the atoms in the middle of the slab should have the same physical properties as bulk atoms.

3.3 QUICKSTEP: a hybrid Gaussian-Plane waves method

Density functional theory is a well established method to perform electronic structure calculations. The standard computational approach to DFT is already efficient and thus appropriate for fairly large systems. However, the computation of the Hartree (Coulomb) energy and the orthogonalization of the wave functions do not scale linearly with the size of the system, therefore these terms dominate the computational cost for larger systems. The hybrid Gaussian and plane waves (GPW) method [81] provides an efficient way to treat these terms accurately at a significantly reduced cost. This method has been implemented in QUICKSTEP [82, 83], which is part of the freely available program package CP2K [84].

The method uses an atom-centered Gaussian-type basis to describe the wave functions and an auxiliary plane pane wave basis to describe the density. With a density represented with plane waves or on a regular grid, the efficiency of Fast Fourier Transforms (FFT) can be exploited to solve the Poisson equation and to obtain the Hartree energy in a time that scales linearly with the system size.

Central in Gaussian and plane waves method (GPW) is the use of two representations of the electron density. Such a dual representation allows for an efficient treatment of the electrostatic interaction and leads to a scheme that has a linear scaling cost for the computation of the total energy and Kohn-Sham matrix with respect to the system size. The first representation of the electron density $\rho(\mathbf{r})$ is based on an expansion in atom centered contracted Gaussian functions

$$\rho(\mathbf{r}) = \sum_{\mu\nu} P^{\mu\nu} \phi_\mu(\mathbf{r}) \phi_\nu(\mathbf{r}) \tag{3.20}$$

where $P^{\mu\nu}$ is a density matrix element and $\phi_\mu(\mathbf{r}) = \sum_i d_{i\mu} g_i(\mathbf{r})$, primitive Gaussian functions $g_i(\mathbf{r})$ and corresponding contraction coefficients $d_{i\mu}$. The second representation employs an auxiliary basis of plane waves

$$\tilde{\rho}(\mathbf{r}) = \frac{1}{\Omega} \sum_{\mathbf{G}} \tilde{\rho}(\mathbf{G}) \exp(i\mathbf{G}\cdot\mathbf{r}) \tag{3.21}$$

where Ω is the volume of the unit cell and $\mathbf{G}$ are the reciprocal lattice vectors. The expansion coefficients $\tilde{\rho}(\mathbf{G})$ are such that $\tilde{\rho}(\mathbf{r})$ is equal to $\rho(\mathbf{r})$ on a regular grid in the unit cell. The difference $|\rho(\mathbf{r}) - \tilde{\rho}(\mathbf{r})|$ goes to zero as the cutoff energy E_{cutoff} goes to infinity. This choice allows for a rapid conversion between $\rho(\mathbf{r})$, $\tilde{\rho}(\mathbf{r})$ and $\tilde{\rho}(\mathbf{G})$ using an efficient mapping procedure and FFT.

With this formalism of a dual density representation, the Kohn-Sham energy functional reads

$$\begin{aligned}
E[\rho] =& E_{\text{T}}[\rho] + E_{\text{en}}[\rho] + E_{\text{H}}[\rho] + E_{\text{XC}}[\rho] + E_{\text{nn}}[\rho] \\
=& \sum_{\mu\nu} P^{\mu\nu} \langle \phi_\mu(\mathbf{r}) | -\frac{1}{2}\nabla^2 | \phi_\nu(\mathbf{r}) \rangle \\
&+ \sum_{\mu\nu} P^{\mu\nu} \langle \phi_\mu(\mathbf{r}) | V_{\text{loc}}^{\text{PP}}(r) | \phi_\nu(\mathbf{r}) \rangle \\
&+ \sum_{\mu\nu} P^{\mu\nu} \langle \phi_\mu(\mathbf{r}) | V_{\text{nl}}^{\text{PP}}(\mathbf{r},\mathbf{r}') | \phi_\nu(\mathbf{r}) \rangle \\
&+ 2\pi\Omega \sum_{\mathbf{G}} \frac{\tilde{\rho}^*(\mathbf{G})\tilde{\rho}(\mathbf{G})}{G^2} \\
&+ \int \epsilon_{\text{XC}}(\mathbf{r}) d\mathbf{r} \\
&+ \frac{1}{2} \sum_{i\neq j} \frac{Z_i Z_j}{|\mathbf{R}_i - \mathbf{R}_j|}
\end{aligned} \tag{3.22}$$

where $E_{\text{T}}[\rho]$ is the electronic kinetic energy, $E_{\text{en}}[\rho]$ is the electronic interaction with the ionic cores, $E_{\text{H}}[\rho]$ is the electronic Hartree energy and $E_{\text{XC}}[\rho]$ is the exchange and correlation energy. The interaction energy of the interacting ionic cores with charge Z_i and position $\mathbf{R}_i$ is denoted by E_{nn}. E_{en}, the electron-nucleus interaction energy, is described by norm-conserving pseudopotentials which are split into a local part, $V_{\text{loc}}^{\text{PP}}(r)$, and a fully non-local part, $V_{\text{nl}}^{\text{PP}}(\mathbf{r},\mathbf{r}')$. The GPW method, as implemented in QUICKSTEP inside CP2K, uses the pseudopotential of Goedecker, Teter and Hutter (GTH) [85, 86]. This is an accurate and transferable pseudopotential which has an analytic form allowing an efficient treatment of all the terms within the GPW method.

The norm-conserving, separable, dual space GTH pseudopotentials consist of a local part including a long-range (LR) and a short-range (SR) term

$$\begin{aligned} V_{\text{loc}}^{\text{PP}}(r) &= V_{\text{loc}}^{\text{LR}}(r) + V_{\text{loc}}^{\text{SR}}(r) \\ &= -\frac{Z_{\text{ion}}}{r}\,\text{erf}\left(\alpha^{\text{PP}} r\right) + \sum_{i=1}^{4} C_i^{\text{PP}} \left(\sqrt{2}\alpha^{\text{PP}} r\right)^{2i-2} \exp\left[-\left(\alpha^{\text{PP}} r\right)^2\right] \end{aligned} \tag{3.23}$$

with

$$\alpha^{\text{PP}} = \frac{1}{\sqrt{2} r_{\text{loc}}^{\text{PP}}} \tag{3.24}$$

and a non-local part

$$V_{\text{nl}}^{\text{PP}}(\mathbf{r}, \mathbf{r}') = \sum_{lm} \sum_{ij} \langle \mathbf{r} | p_i^{lm} \rangle h_{ij}^{l} \langle p_j^{lm} | \mathbf{r}' \rangle \tag{3.25}$$

with the Gaussian-type projectors

$$\langle \mathbf{r} | p_i^{lm} \rangle = N_i^l Y^{lm}(\hat{r}) r^{l+2i-2} \exp\left[-\frac{1}{2}\left(\frac{r}{r_l}\right)^2\right] \tag{3.26}$$

where N_i^l are normalization constants and $Y^{lm}(\hat{r})$ spherical harmonics. The smallest set of GTH pseudopotential parameters ($r_{\text{loc}}^{\text{PP}}$, C_i^{PP}, r_l and h_{ij}^l) are optimized with respect to all-electron wave functions as obtained from fully relativistic density functional theory calculations.

The GPW is less sensitive to the hardness of the pseudo potential since the kinetic energy and the short range pseudo potential terms are computed analytically in the Gaussian basis. The long range term can be efficiently treated as part of the electrostatic energy, which take advantage of the plane waves representation of the density, whereas the short range term can be easily computed as two and three center overlap integrals.

3.4 Transition rates

A very important problem in theoretical chemistry and in condensed matter physics is the calculation of the rate of transitions, for example in chemical reactions or diffusion events. As we will see in the following, Transition State Theory (TST) is a theoretical framework within which, using classical statistical mechanics and few assumptions, it is possible to calculate the transition rate. However, the practical realization of calculation is based on methods that allows the determination of the minimum energy path of the transition, configuration of the transition state and the energy barrier of transition. We employed the nudged elastic band method which is a very powerful tool and at same time very simple.

3.4.1 The transition state theory

For many systems, it is sufficient to treat the motion of atoms using classical mechanics, however, the transitions of interest are typically many orders of magnitude slower than vibration of the atoms, so a direct simulation of the classical dynamics is not useful. Such slow events are called “rare events”.

Although, rare events cannot be observed in ordinary molecular dynamics simulations runs, one can obtain accurate estimates of transition rates using purely statistical methods, namely Transition State Theory (TST) [87, 88]. TST relies on two basic assumptions: (1) the rate is slow enough that a Boltzmann distribution is established and maintained in the reactant state and (2) a dividing surface of dimensionality $D-1$, where D is the degrees of freedom in the system, can be identified such that a reacting trajectory going from the initial state to the final state only crosses the dividing surface once. Therefore, the dividing surface represents a bottleneck for the transition.

The overall TST rate constant can be written as the product of the probability to find the system at the transition state times the rate at which the system moves across the transition state once it gets there

$$k_{\mathrm{TST}} = \frac{1}{2}\left\langle |v|\,\delta(r-r^{\dagger})\right\rangle \tag{3.27}$$

where $|v|$ is the velocity and $r^{\dagger}$ is the point on the dividing surface. It is known that TST overestimates the rate of escaping from a initial state and this leads to a variational principle which can be used to define the optimal dividing surface [89].

In solids atoms are typically packed together and they perform small vibrations around their equilibrium position. This is particularly true when the solid is below and far away from the melting temperature. Therefore, the solids are well described as harmonic oscillators around stationary points (minima and saddle points). For such situations the harmonic form of transition state theory (hTST) is often a very good approximation which can be used to evaluate the TST rate constant [90]. In one dimension and within the harmonic approximation one assumes that the reactant basin is quadratic $U(x) = \kappa x^2/2$ and the transition state is an exit point from the parabola to a new state at some point $x = x^{\dagger}$ with energy $\Delta E = \kappa {x^{\dagger}}^2/2$

$$\begin{aligned} k_{\mathrm{hTST}} &= C\left\langle \delta(x-x^{\dagger})\right\rangle \\ &= C\,\frac{\int_x e^{-\kappa x^2/2k_{\mathrm{B}}T}\,\delta(x-x^{\dagger})\,dx}{\int_x e^{-\kappa x^2/2k_{\mathrm{B}}T}\,dx} \\ &= C\,\frac{e^{-\Delta E/k_{\mathrm{B}}T}}{\sqrt{2\pi k_{\mathrm{B}}T/\kappa}} \\ &= \nu e^{-\Delta E/k_{\mathrm{B}}T} \end{aligned} \tag{3.28}$$

where ΔE indicates the energy difference between the transition state and the initial state, $\Delta E = E^{\dagger} - E^{\mathrm{init}}$. In higher dimensional systems, the analysis is the same, except that the transition state is characterized by a saddle point with $3N-1$ real normal modes, and the minimum by $3N$ normal modes. The ratio of partition functions is given by the product of positive frequencies at the saddle and the minimum (entropic term) times the probability of being at the saddle point energy (enthalphic term)

$$k_{\mathrm{hTST}} = \frac{\prod_i^{3N}\nu_i^{\mathrm{init}}}{\prod_i^{3N-1}\nu_i^{\dagger}}\,e^{-\Delta E/k_{\mathrm{B}}T} \tag{3.29}$$

The most challenging part of the calculation is the search for the relevant saddle points. The reaction coordinate at the saddle point is the direction of the unstable mode (the

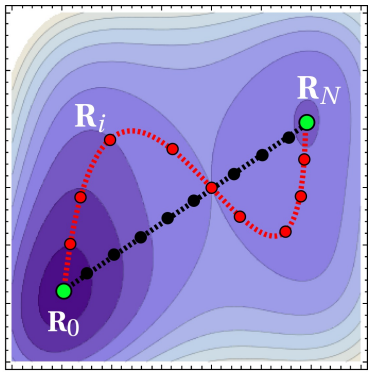

Figure 3.1: Schematic representation of the nudged elastic band method. Here a hypothetical potential energy surface is represented on which an unoptimized (black) and optimized (MEP) paths are shown. 1) Initial state and the final state are known *a priori*, $\mathbf{R}_0$ and $\mathbf{R}_N$, 2) intermediate replicas of the system, $\mathbf{R}_i$, are created by interpolation between initial and final states and connected to each other with springs (black curve). 3) After the minimization the MEP is found (red curve).

normal mode with negative eigenvalue). For systems where one or more atoms need a quantum description zero point energy can be taken in account by means of harmonic phonon frequencies. If both zero point energy and tunneling effects have to be taken into account, a quantum mechanical extension of TST has to be considered and the Feynman Path Integrals formalism has to be used [91].

3.4.2 Nudged elastic band method

The idea behind the Nudged Elastic Band (NEB) method is very simple. However the NEB method represents a very powerful tool for finding the minimum energy path. In this method a chain of intermediate replicas of the system are created between the initial state and the final state and connected to each other by springs. In such a way a discrete representation of the transition path is reproduced. Initially, the intermediate replicas are created by interpolating the initial and final configurations or another path determined from separate calculations can be used as guess path. An optimization algorithm is then applied to relax the images down towards the MEP. We denote the string of images as $\{\mathbf{R}_0, \mathbf{R}_1, \ldots, \mathbf{R}_N\}$ where $\mathbf{R}_i$ indicate the i-th image configuration of the system and $\mathbf{R}_0$ and $\mathbf{R}_N$ correspond to the initial and final states respectively (cf. Fig. **??**).

We can write the total energy of the *elastic band* made of $N-1$ beads and N springs with spring constant k as

$$S(\mathbf{R}_0, \mathbf{R}_1, \ldots, \mathbf{R}_N) = \sum_{i=1}^{N-1} E(\mathbf{R}_i) + \sum_{i=1}^{N} \frac{k}{2} (\mathbf{R}_i - \mathbf{R}_{i-1})^2 \,. \tag{3.30}$$

This expression then is minimized with respect to the intermediate images, $\mathbf{R}_1, \mathbf{R}_2, \ldots, \mathbf{R}_{N-1}$. Actually, in this simple formulation the elastic band tends to cut the corners and gets

pulled off the MEP by spring forces in regions where the MEP is curved. Both the border-cutting and the sliding-down problems can be resolved easily with a force projection, *nudging*. The component of the spring force perpendicular to the path, which allows corner-cutting, and the parallel component of the true force coming from atom interactions, which allows sliding-down, are eliminated from the forces considered in the minimization algorithm. In this way the force acting on the i-th image reads

$$\mathbf{F}_i = -\nabla E(\mathbf{R}_i)|_\perp + \mathbf{F}_i^{\text{spring}} \cdot \hat{\tau}_i \hat{\tau}_i \tag{3.31}$$

where $\nabla E(\mathbf{R}_i)|_\perp$ is the perpendicular component of the gradient of the potential energy with respect to the atomic positions in the system at image i which is obtained by subtracting out the parallel component

$$\nabla E(\mathbf{R}_i)|_\perp = \nabla E(\mathbf{R}_i) - \nabla E(\mathbf{R}_i) \cdot \hat{\tau}_\parallel \hat{\tau}_\parallel \,. \tag{3.32}$$

$\hat{\tau}_i$ is the unit vector tangent to the path at each image and $\hat{\tau}_\parallel$ is the unit vector parallel to the path at each image.

The unit vector tangent at the path on image i can be estimated as

$$\hat{\tau}_i = \frac{\mathbf{R}_i - \mathbf{R}_{i-1}}{|\mathbf{R}_i - \mathbf{R}_{i-1}|} + \frac{\mathbf{R}_{i+1} - \mathbf{R}_i}{|\mathbf{R}_{i+1} - \mathbf{R}_i|} \,. \tag{3.33}$$

However, there are several other methods to improve the calculation of the tangent [92]. This method does not require a specific approach to the calculation of the potential energy, $E(\mathbf{R}_i)$, and classical or quantum mechanical methods can be used indistinctly. In this work $E(\mathbf{R}_i)$ is calculated within DFT framework.

A variant of the original NEB method has been developed – the Climbing Image NEB (CI-NEB) [93]. Here the image which has the highest energy in the band, after one or more step of normal NEB, is forced to move uphill in energy along the elastic band. This is realized by total cancellation of the spring force on that image and including only the parallel component of the true force with the opposite sign

$$\mathbf{F}_{i\text{-max}}^{\text{climb}} = -\left[-\nabla E(\mathbf{R}_{i\text{-max}})\right] \cdot \hat{\tau}_\parallel \hat{\tau}_\parallel \,. \tag{3.34}$$

After convergence is achieved the i-max image is sitting at the saddle point to within the prescribed tolerance. In such a way we are able to simultaneously obtain the energy barrier of the transition (difference between the energy at the transition state and the energy at the initial state, $\Delta E = E^\dagger - E^{\text{init}}$) and the system configuration of the transition state. These latter are very important to calculate the transition rate as prescribed by hTST.

3.5 Colored-noise quantum thermostat

3.5.1 Generalized Langevin equation

Nuclear quantum effects are extremely important in many condensed-phase systems. For instance, zero-point fluctuations affect static correlations, while energy quantization causes deviations from the classical value of the specific heat at low temperatures. A

quantum treatment of the ionic degrees of freedom is mandatory for capturing these effects, which are particularly important when light atoms or stiff vibrational modes are present. Conventional techniques for including quantum effects, such as Path Integral MD (PIMD) [94], are computationally demanding and for this reason the nuclei in molecular simulations are often treated classically, even when the electronic degrees of freedom are accounted for quantum-mechanically [95].

Very recently a stochastic molecular dynamics framework based on generalized Langevin equations (GLE) has been devised in our group. Among the many possible applications [96, 97, 98], it allows one to model to a good approximation nuclear quantum effects at negligible additional effort with respect to purely classical dynamics. An additional advantage of this approach is that not only atomic configurations, but also the momentum reproduce the quantum distribution.

A colored-noise Langevin dynamics for a particle with unit mass, position q and momentum p, subject to a potential $V(q)$ can be written in a Markovian form as

$$\begin{aligned} \dot{q} &= p \\ \begin{pmatrix} \dot{p} \\ \dot{\mathbf{s}} \end{pmatrix} &= \begin{pmatrix} -V'(q) \\ \mathbf{0} \end{pmatrix} - \begin{pmatrix} a_{pp} & \mathbf{a}_p^T \\ \bar{\mathbf{a}}_p & \mathbf{A} \end{pmatrix} \begin{pmatrix} p \\ \mathbf{s} \end{pmatrix} + \begin{pmatrix} b_{pp} & \mathbf{b}_p^T \\ \bar{\mathbf{b}}_p & \mathbf{B} \end{pmatrix} \begin{pmatrix} \xi \end{pmatrix} \end{aligned} \tag{3.35}$$

where ξ is a $n+1$ dimension vector of uncorrelated Gaussian numbers, *i.e.* $\langle \xi_i(t)\xi_j(0)\rangle = \delta_{ij}\delta(t)$. Furthermore, here, the dynamical variables (q,p) are supplemented by a set of n additional momenta $\mathbf{s}$, which will be bilinearly coupled to the physical momentum p, this is the way to avoid an otherwise non-Markovian formulation using only the physical dynamic variables. In this formulation we are looking at the evolution of the extended phase space vector $\mathbf{x} = (q, p, \mathbf{s})$ which is determined by the two matrices

$$\mathbf{A}_p = \begin{pmatrix} a_{pp} & \mathbf{a}_p^T \\ \bar{\mathbf{a}}_p & \mathbf{A} \end{pmatrix} \tag{3.36}$$

and

$$\mathbf{B}_p = \begin{pmatrix} b_{pp} & \mathbf{b}_p^T \\ \bar{\mathbf{b}}_p & \mathbf{B} \end{pmatrix} \tag{3.37}$$

named deterministic drift matrix and $(p,\mathbf{s})$ diffusion matrix respectively.

In order to define the conditions which are required for Eqs. (3.35) to sample the canonical, constant-temperature ensemble, it has been shown [96] that the drift and diffusion matrices have to fulfill the condition

$$\mathbf{D}_p = \mathbf{B}_p\mathbf{B}_p^T = k_\mathrm{B}T\left(\mathbf{A}_p + \mathbf{A}_p^T\right) \tag{3.38}$$

i.e. the fluctuation-dissipation theorem which fixes $\mathbf{D}_p$ once $\mathbf{A}_p$ is given. However, a number of useful properties can be obtained if the fluctuation-dissipation theorem is violated: inclusion of nuclear quantum effects is the case.

3.5.2 Quantum thermostat

To develop a robust approach for introducing nuclear quantum effects, by means of an appropriate generalized Langevin equation, we first consider the harmonic oscillator as an exact treatment available in quantum-mechanical framework.

The finite-temperature density matrix for a quantum harmonic oscillator of frequency ω at temperature T reads

$$\begin{aligned}\rho(q,q') &\propto \sum_n e^{-\varepsilon_n/k_\mathrm{B}T}\,\Psi_n^\star(q)\Psi_n(q') \\ &\propto \exp\left[-\omega^2\left(\frac{\left(q+q'\right)^2/4\hbar\omega}{\coth\left(\hbar\omega/2k_\mathrm{B}T\right)}+\frac{\left(q-q'\right)^2/4\hbar\omega}{\tanh\left(\hbar\omega/2k_\mathrm{B}T\right)}\right)\right]\end{aligned} \tag{3.39}$$

where ε_n and Ψ_n are the eigenvalues and eigenvectors of the harmonic Hamiltonian. For any temperature, the density is a Gaussian, whose width depends on ω and T

$$\rho(q)=\rho(q,q)\propto \exp\left[-\frac{1}{2}\omega^2q^2\left(\frac{\hbar\omega}{2}\coth\frac{\hbar\omega}{2k_\mathrm{B}T}\right)^{-1}\right] \tag{3.40}$$

For a classical oscillator the probability distribution of the displacement q is also a Gaussian

$$P(q)\propto \exp\left[-\frac{1}{2}\frac{\omega^2q^2}{k_\mathrm{B}T}\right]. \tag{3.41}$$

It is therefore possible to reproduce the quantum stationary distribution of q, in a purely classical framework, by performing canonical sampling using a ω-dependent target temperature

$$T^\star=\frac{\hbar\omega}{2k_\mathrm{B}}\coth\frac{\hbar\omega}{2k_\mathrm{B}T} \tag{3.42}$$

The distribution of momenta, which can be obtained by writing the density matrix in the momentum representation, is also Gaussian, and has a width consistent with the classical distribution at the effective temperature $T^\star$.

In passing, it is interesting to note that this isomorphism has consequences well beyond the marginal probabilities of the phase-space distribution. Consider any observable which depends locally on positions only. Its finite-temperature expectation value can be written in the position representation in terms of the one- particle density

$$\langle\mathscr{A}\rangle=\frac{\sum_n e^{-\varepsilon_n/k_\mathrm{B}T}\int\mathscr{A}(q)\left|\Psi_n(q)\right|^2dq}{\sum_n e^{-\varepsilon_n/k_\mathrm{B}T}}=\int\mathscr{A}(q)\rho(q)\,dq\,. \tag{3.43}$$

The same expectation value can be computed exactly as the ensemble average of $\mathscr{A}(q)$ over a classical trajectory at the effective temperature $T^\star$.

To turn this isomorphism into a viable method for computing nuclear quantum effects, one must be able to enforce the ω-dependent effective temperature, $T^\star$ simultaneously on different normal modes, without any explicit knowledge of the phonon spectrum and displacement patterns. This goal can be achieved using a generalized Langevin equation, provided that the fluctuations computed for an individual harmonic oscillator, as a function of its frequency, are consistent with Eq. (3.42).

To enforce this behavior we compute the stationary distribution in the harmonic limit, and fit the fluctuations $c_{pp}(\omega)$ and $c_{qq}(\omega)$ to the target functions $\tilde{c}_{pp}(\omega)=\omega^2\tilde{c}_{qq}(\omega)=\frac{\hbar\omega}{2}\coth\frac{\hbar\omega}{2k_\mathrm{B}T}$.

In practice, one does not need to perform a separate fit for each system and temperature. Instead, it is sufficient to prepare a library of matrices fitted using $\omega_\mathrm{max}=1$, $k_\mathrm{B}T=1$

and a number of different values for the adimensional parameter $\varphi = \hbar\omega_{\max}/k_{\mathrm{B}}T$. The resulting GLE matrices $\mathbf{A}_p$ and $\mathbf{C}_p$ can then be adapted for the simulations at any temperature T.

Discussion on accuracy A long *ab initio* MD trajectory makes it difficult to obtain a reliable reference to gauge the accuracy of our method, as an *ab initio* PIMD trajectory would be prohibitively expensive and, to our knowledge, no good-quality classical force field is available. A possible strategy for obtaining an order-of-magnitude estimate of the uncertainty in the results of a quantum thermostat calculation, that does not require one to do an expensive path-integral reference calculations, is to perform two simulations with two different sets of parameters, that are fitted to slightly different frequency ranges, or with different coupling strengths. The difference between the two results provides a lower bound on the inaccuracy in the treatment of quantum effects for the observables of interest.

We will now demonstrate how this procedure works considering the case of lithium imide, Li_2NH. We applied a empirical strategy in which two sets of parameters using different fitting strategies have been used. The inaccuracy has been quantified by calculating the discrepancy between the results obtained with the two choices. The highest frequencies present, which set the upper bound of the range to be included in the fit, can be ascribed to the NH bond stretching. Consequentially, the same GLE parameters we used for water [98] (fitted for $\varphi = \hbar\omega_{\max}/k_B T = 20$) are sufficient to cover the relevant range of frequencies at 300 K, and can be used as a first reference. As a second option we used $\varphi = 50$ since we know that $\varphi > 20$ is required in the low-temperature simulations that we intend to perform in the future (form more details on the method cf. Ref. [98]). We therefore consider the $\varphi = 50$ parameters as our best estimate, and use $\varphi = 20$ only to gauge the inaccuracies in the physical observables.

Results

4

Low and high temperature phases of lithium imide

In this chapter we present the results of our simulations of the low and high temperature phases of Li_2NH. Starting from the structure proposed by Herbst and Hector [34] (HH phase, see section 2.3) we have been able to refine the geometry so as to find a theoretical structure in excellent agreement with available experimental data and also to solve the inconsistence of previous proposals that we have described in section 2.3. By means of molecular dynamics simulations we also clarified the nature of the transformation between the low and high temperature phases and have provided a new picture for the local structure of Li_2NH at HT.

4.1 The low temperature phase

We first performed geometry optimizations of the HH unit cell of 64 atoms (16 Li_2NH formula units) using PWscf code [99] and a $4\times4\times4$ k-points mesh. The calculations have been performed within DFT with the PBE gradient-corrected exchange and correlation functional [78]. Ultrasoft [100] and Goedecker-type [85] pseudopotentials were used, respectively, for N and H atoms and for Li with three valence electrons.

As already discussed in section 2.3, we observed that upon geometry optimization the $Ima2$ symmetry is unstable and goes into a $Imma$ symmetry as Li interstitial atoms move to octahedral sites (from 32e to 16c sites of the $Fd\bar{3}m$ symmetry). In fact, the optimized positions of atoms independent by symmetry, for this $Imma$ structure are similar to previous *ab initio* results obtained by Herbst and Hector [34, 62]. Nevertheless, these authors do not mention the change in symmetry and continue to state that the optimized structure has $Ima2$ symmetry. In Tab. 4.1 we report the optimized atomic positions as obtained from our calculations, from previous *ab initio* calculations and from Rietveld refinement of experimental data [11]. Our results are very similar to the previous theoretical study and both of them differ from the experimental data,

Table 4.1: Atomic positions (in crystallographic units) of the ordered orthorhombic crystal structure with $Ima2$ space group (experimental data from Ref [11]). Upon geometry optimization in both HH (see Ref. [34]) and our results a change in symmetry is observed from the $Ima2$ space group into the $Imma$ space group.

atom	position		our	HH	exp.
Li1	4b	x	1/4	1/4	1/4
		y	0.3831	0.3826	0.3437
		z	0.3703	0.3703	0.3750
Li2	4b	x	1/4	1/4	1/4
		y	0.8751	0.8765	0.8766
		z	0.3703	0.3703	0.3750
Li3	4b	x	1/4	1/4	1/4
		y	0.1051	0.1058	0.1250
		z	0.3703	0.3705	0.3750
Li4	4b	x	1/4	1/4	1/4
		y	0.2500	0.2498	0.2876
		z	0.1202	0.1206	0.0499
Li5	8c	x	0.5081	0.5074	0.4984
		y	0.1157	0.1155	0.1250
		z	0.1370	0.1372	0.1266
Li6	8c	x	0.5081	0.5073	0.4984
		y	0.3843	0.3844	0.3750
		z	0.1036	0.1034	0.1234
N1	4b	x	1/4	1/4	1/4
		y	0.0094	0.0087	0.0082
		z	0.6093	0.6101	0.6086
N2	4b	x	1/4	1/4	1/4
		y	0.0094	0.0089	0.0082
		z	0.1313	0.1305	0.1414
N3	8c	x	0.4695	0.4691	0.4836
		y	0.2406	0.2405	0.2418
		z	0.3704	0.3700	0.3750
H1	4b	x	1/4	1/4	1/4
		y	0.5504	0.5505	0.5476
		z	0.2280	0.2295	0.2203
H2	4b	x	1/4	1/4	1/4
		y	0.5504	0.5506	0.5476
		z	0.5126	0.5114	0.5297
H3	8c	x	0.5814	0.5819	0.5953
		y	0.1933	0.1945	0.2024
		z	0.8703	0.8700	0.8750

specifically, in the position of atom Li4, which is the interstitial atom (see Tab. 4.1). We obtained the same $Imma$ geometry by using a 128 atoms supercell ($\sqrt{2} \times 1 \times \sqrt{2}$ HH unit cell, 32 Li_2NH formula units), sampling the Brillouin Zone (BZ) at the Γ-point.

Moreover, as discussed in section 2.3, the theoretical formation energy of this phase is too high when compared to experimental data and, for this reason, alternative ordered models for the LT phase of Li_2NH have been proposed by means of density functional theory calculations, in particular structures with $Pnma$ (MOW) [63] and $Pbca$ (MC) [64] space groups. Both structures $Pnma$ and $Pbca$ do result in a marginally lower free energy than the HH structure (see Tab. 4.4 in section 2.3). However, these phases do not match the experimental $Fd\bar{3}m$ space group since they show a deformed anti-fluorite structure with fcc site fully occupied by N and Li not exactly in the tetrahedral interstitial sites. Furthermore, their lattice parameters are not commensurable with the experimental values.

On the other hand, the HH structure looks more reasonable as the LT phase of Li_2NH and is in closer agreement with experiments. This is an anti-fluorite superstructure with one of eight Li sites is unoccupied and tetrahedrally coordinated by 4 NH groups. We performed MD simulations at 400 K using a 128-atoms supercell ($\sqrt{(2)} \times 1 \times \sqrt{2}$ HH unit cell, 32 Li_2NH formula units) and PBE or BLYP functionals of the $Fm\bar{3}m$ structure to test the local stability of the perfect anti-fluorite phase. Our simulations revealed that the $Fm\bar{3}m$ phase is locally unstable with respect to the formation of Li Frenkel pairs when H atoms are randomized over 48h or 24e positions as proposed in earlier experimental XRD studies [59]. Frenkel pairs spontaneously form in the simulation at 400 K. The four nearest neighbor NH groups point tetrahedrally toward the newly formed vacancy restoring the local environment of the low temperature HH phase. At the same time, other NH groups (not nearest neighbors to vacancies) rotate very rapidly (almost as fast as a free rotator at the given temperature). The rotations of NH groups are strongly coupled with Li vibrations around their antifluorite sites. By fixing the positions of Li atoms, the librational motions of the NH groups were observed to be drastically reduced. For all these reasons we chose the HH structure as starting point for our simulations.

4.1.1 Dynamical simulations

We started our analysis by investigating the stability, at 300 K, of the structure proposed by Herbst and Hctor (HH $Imma$ phase) by means of molecular dynamics simulations. A $\sqrt{2} \times 1 \times \sqrt{2}$ 128-atom supercell corresponding to two $Imma$ unit cells was used. We performed Born-Oppenheimer molecular dynamics simulations within Density Functional Theory (DFT) with the PBE gradient corrected exchange and correlation functional [78] as implemented in the CPMD package [101]. Ultrasoft [100] pseudopotentials were used for N and H atoms while for Li with all the three electrons a Goedecker-type [85] pseudopotentials was used. Kohn-Sham orbitals were expanded in plane waves up to a kinetic-energy cutoff of 50 Ry. Brillouin Zone (BZ) integration was restricted to the Γ-point only. A time step of 0.6 fs was used and a constant temperature of 300 K was enforced by an optimal-sampling generalized Langevin equation thermostat. Equilibrium geometries of relevant structures that emerged from the dynamical simulations were optimized with special k-points meshes and the PWscf program from the Quantum-Espresso suite of programs [99]. Activation energies for diffusion processes

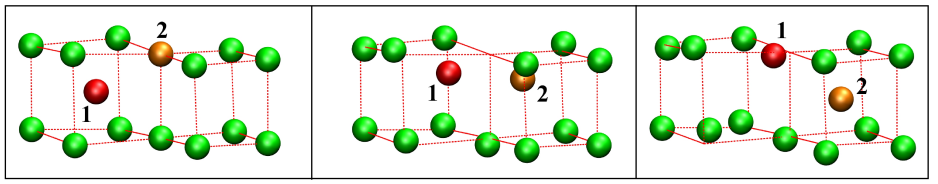

Figure 4.1: Diffusion exchange mechanism for Li interstitial. In the picture the initial, transition and final states are shown. The red and the orange spheres, also labeled 1 and 2, are the Li atoms involved in the process. In the initial configuration atom 1 occupies a Li4 site and atom 2 a Li2 site while the reverse is true in the final state.

were obtained by Nudged Elastic Band optimizations [92].

In the dynamical simulations we observed that constitutional vacancies coordinated by 4 NH groups are very stable, the latter perform only small librations around their equilibrium position. Instead, Li interstitials occupying the Li4 positions (cf. sec. 2.3 for the definition of symmetrically inequivalent Li positions) are very mobile and we observed several jumps between adjacent sites, taking place via an exchange mechanism with one of the Li2 atoms (see Fig. 4.1). The activation energy turns out to be as low as 0.13 eV. Moreover, we verified that many different arrangement of interstitial atoms in Li4 sites have total energies within few meV. At finite temperature, we would thus expect a disordered arrangement of interstitial atoms in the Li4 sites, leading to a fractional occupation of 1/2 and an overall $Fd\bar{3}m$ space group.

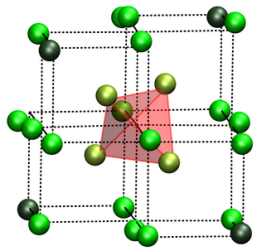

Figure 4.2: Our proposed correlation in the occupation of Li3 and Li2 sites leads to a tetrahedral cluster of four interstitial ions Li^+ at Li3 sites around a new vacancy at Li2 site.

However, the positions of Li4 still differ from those of Li3 obtained from Rietveld refinement. Moreover, the low diffusion barriers found would assign a superionic character to Li_2NH even at room temperature, which is inconsistent with experimental data.

The solution to these discrepancies came from a closer inspection of the molecular dynamics trajectory. This revealed that, as soon as three interstitial atoms happen to be all nearest neighbors to an occupied Li2 site, the latter atom is displaced from its position. A tetrahedral cluster is formed with a vacant Li2 site at its center (see Fig. 4.2). These clusters are stable and remain thereafter preventing diffusion of Li interstitials. The interstitial Li now occupies the Li3, 32*e*, sites and a vacancy is introduced at site Li2 in such a way that the very short Li3-Li2 distance of the unrelaxed HH model is removed. The Li-Li distance in the tetrahedral cluster of interstitials is 2.52 Å. Li are positive ions, they repel each other but they are all attracted to the sites Li2 which experiences a stronger negative Madelung potential. The Madelung potential is negative also on the Li4 site but it is stronger on site Li2. Once three interstitials are in nearest Li4 sites, it is favorable to displace an ion from the Li2 site since, although the latter ion looses energy, the other three gain energy by moving closer to the

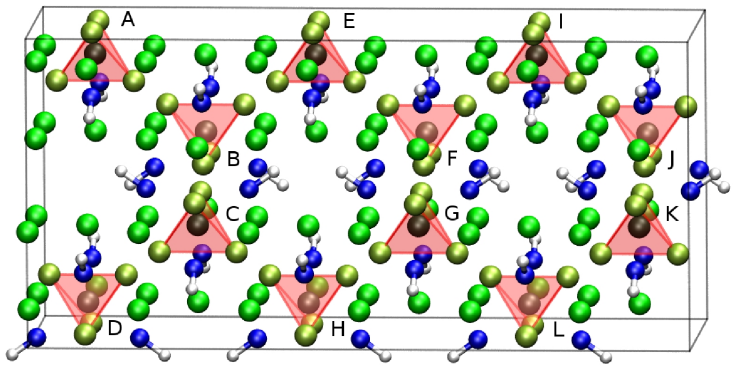

Figure 4.3: The 192 atoms supercell is shown (3 × 1 × 1 HH unit cells). The labeling indicates all possible sites where the four Li2 vacancy-Li3 interstitials clusters can be distributed inside the supercell. We found that the lowest-energy arrangements are *ACFL* (-2.89 kJ/mol/f.u.) and *AEGK* (-2.80). Energies are given relative to the relaxed HH structure. Configurations where the tetrahedra are unevenly distributed such as *AEIC* (-1.64) or *ACEG* (0.39) are higher in energy and those where nearest-neighbor sites are occupied simultaneously are even less stable.

empty Li2 site.

Having observed the propensity of Li atoms to form this rather stable tetrahedral structure, we propose a new stable structure in excellent agreement with the diffraction data. At T=0 we expect that all the Li interstitials are involved in the formation of tetrahedral clusters. The smallest supercell compatible with this requirement and consistent with the stoichiometry is formed by 3 × 1 × 1 HH unit cells (192 atoms, 48 Li_2NH formula units). In this supercell there will be four vacancy-interstitials clusters, which can be distributed over twelve Li2 sites (see Fig.4.3). These 4NH-vacancy complexes form a perfect diamond lattice. Furthermore, the sites which can host the tetrahedra of Li interstitials, *i.e.* the Li2 sites, also form a diamond lattice but this is only partially filled because of the low concentration of tetrahedra.

We considered all the possible arrangements of the vacancy-interstitials tetrahedra independent by symmetry excluding those where two first-neighbor Li3 sites are occupied.

Provided that the clusters are evenly distributed in the cell to balance the negatively-charged constitutional vacancies, the spread in the total energy of the different configurations is well within thermal energy at room temperature (see Fig. 4.3). We repeated our analysis on a larger 3 × 1 × 3 supercell and found similar results. This degeneracy allows for long-range disorder in the arrangement of tetrahedra, so that the diffraction pattern is consistent with a higher-symmetry $Fd\bar{3}m$, with fractional occupations of Li3 (1/3) and Li2 (2/3). These fractional occupations are compatible with the stoichiometry and solve the inconsistency in the model proposed by Balogh *et al.* [11].

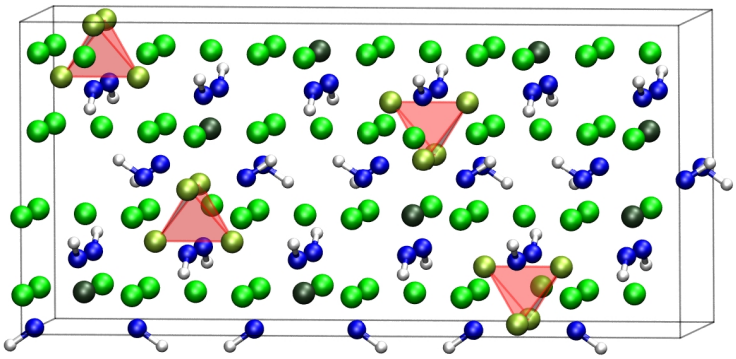

Figure 4.4: In the picture one of the possible, almost degenerate, arrangements for Li_4-clusters for our proposed LT crystal structure of Li_2NH.

4.1.2 The new low temperature crystal structure for Li_2NH: energetics and structural parameters

By averaging over possible configurations of our 192-atoms supercell we obtained the symmetry-adapted average positions reported in Tab. 4.2 and the relative mean square displacements which would correspond to a static contribution to the Debye-Waller factor. We calculated the thermal Debye-Waller factor for each species as a function of the temperature from harmonic phonons (at the supercell Γ-point; see Fig. 4.5). The mean square displacement as a function of the temperature in the harmonic approximation is given by

$$\langle u_\alpha^2 \rangle = \frac{1}{N_\alpha} \sum_{m,i} \frac{\hbar}{\omega_m} \frac{|\mathbf{e}(m,i)|^2}{M_\alpha} \left[n_B \left(\frac{\hbar \omega_m}{k_B T} \right) + \frac{1}{2} \right] \tag{4.1}$$

where α runs over the atomic species, M_α is the mass of αth species, i runs over N_α atoms of species α, while ω_m and $\mathbf{e}(m,i)$ are the frequency and the eigenvector of the mth harmonic phonon.

The presence of clusters generates long-range distortions in the Li1 lattice and in the orientation of H atoms around a constitutional vacancy, resulting in a large mean square displacement from the average position for these species.

The agreement with the experimental positions from Rietveld refinement is excellent. The diffraction pattern of our proposed structure compares well with that deduced from the experimental positions and fractional occupation as shown in Fig. 4.6

The formation enthalpy of the *ACFL* configuration (see Fig. 4.3) is lower (-2.9 kJ mol^{-1} $f.u.^{-1}$) than that of the HH structure. Considering also zero-point energy and the harmonic contribution to the total free energy, our structure is still more stable than HH's (-1.7 kJ mol^{-1} $f.u.^{-1}$ at 298 K) and the structure proposed in Ref. [63] (-0.3 kJ mol^{-1} $f.u.^{-1}$). Our structure is slightly less stable (by 2.1 kJ mol^{-1} $f.u.^{-1}$) than that suggested in Ref. [64] however that structure does not correspond to the experimental space group. Note that in accurate quantum chemical calculations one is normally satisfied when 4 kJ/mol accuracy is reached. Moreover, entropic contributions due to disorder might compete with small enthalpy differences of ordered models and need to be taken into

Table 4.2: Structural parameters for the best-fit $Fm\bar{3}m$ structure corresponding to the *ACFL* arrangement of tetrahedral clusters in a 3 × 1 × 1 HH supercell (see Fig. 4.3). The Debye-Waller factor is the sum of a contribution due to static disorder and a thermal contribution calculated at T=100K for Li_2ND. The experimental data from Rietveld refinement of neutron diffraction patterns at 100 K from Ref. [11] are given in parentheses.

Site	x **(exp. Ref. [11]) (crystal unit)**	$\mathbf{U_{iso}}$ **static/thermal** $[10^{-2}\text{Å}^2]$
N 32*e* f=1	0.2408 (0.2418)	0.34/0.50
D 32*e* f=1	0.2982 (0.2976)	1.58/2.00
Li1 48*f* f=1	0.3755 (0.3734)	2.18/0.93
Li2 8*a* f=2/3	–	0.25/0.87
Li3 32*e* f=1/3	0.0367 (0.0376)	0.22/0.91

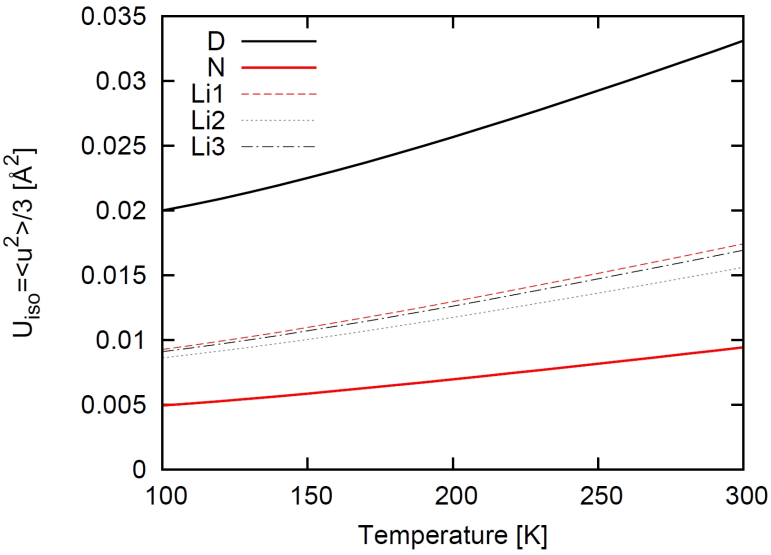

Figure 4.5: Debye-Waller factor, $U_{\text{iso}} = 1/3\langle u_\alpha^2 \rangle$, for D, N, Li1, Li2, Li3 as a function of the temperature.

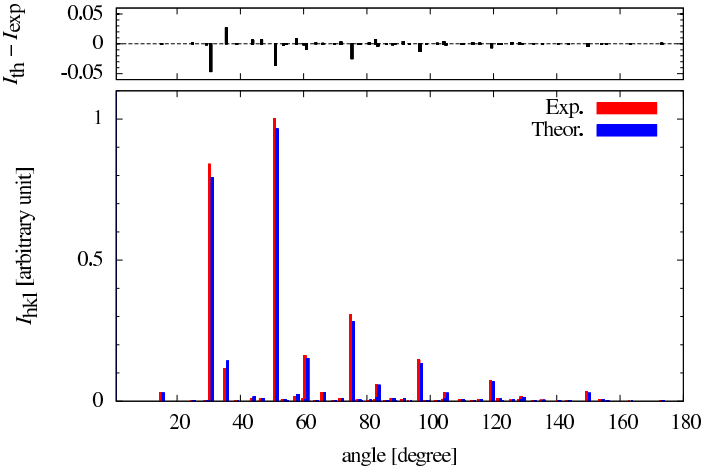

Figure 4.6: Bragg reflections intensities computed with the average positions and occupations reported in Tab. 4.2, compared with those obtained using experimental values. No instrument-related corrections have been applied and the same Debye-Waller factor (U_{iso} = 0.05 Å^2) has been used for all atomic species.

account before assigning the most stable phase at the DFT level. Because of all the above limitations, our aim was not to find the lowest possible ordered structure on the potential energy surface as pursued in Refs. [63, 64] but was instead to refine a disordered structure which was a local minimum in DFT in a way that is compatible with the experiments.

We verified the stability of the tetrahedral clusters by performing 20 ps of molecular dynamics at 300 K using the most stable arrangement *ACFL*. The vacancy-interstitials clusters do not break and the constitutional vacancies do not diffuse on the simulation time scale. In fact, the computed energy barrier to break a tetrahedral cluster by diffusion of a Li3 ion is 0.5 eV, as obtained by NEB optimization, resulting in a low mobility of Li atoms in the LT phase (Li3 diffuses by an exchange mechanism similar to that of Li4, see Fig. 4.1). The energetic cost of breaking a cluster in the *ACFL* structure, via the reaction 4 Li3 $\longrightarrow$ Li2 + 3 Li4, is ΔE=0.20 eV. This energy depends on the final configuration of the interstitials, and on the number of clusters which are simultaneously broken. For instance, the difference in energy with the HH structure – with all the clusters broken – amounts to ΔE=0.36 eV per cluster.

We can compute the change in configurational entropy due to breaking of tetrahedra and formation of these interstitial Li4 atoms, by assuming a perfectly random distribution of tetrahedra and occupied Li4 interstitial sites. To do thus we considered that the number of tetrahedra N_T is related to the number of Li4 and Li2 sites by $N_{Li4} = 6N_T$ and $N_{Li2} = 3N_T$. The change in free energy resulting from the breaking of a fraction x of

Table 4.3: Summary of reaction and activation energies of elementary processes for Li diffusion and Li-cluster breaking.

	energy [eV]	activation energy [eV]
lithium diffusion (Fig. 4.1)		
Li4 + Li2 ⟶ Li2 + Li4		0.13
Li3 + Li2 ⟶ Li2 + Li4		0.50
Li-cluster breaking		
4 Li3 ⟶ Li2 + 3 Li4	0.20	
4 [4 Li3] ⟶ 4 [Li2 + 3 Li4] (Our ⟶ HH)	0.36 (per cluster)	

tetrahedra is given by

$$\frac{F}{N_T} = x\Delta \mathrm{E}_0 - \frac{k_B T}{N_T}\left[\ln\binom{3N_T}{N_T(1-x)} - \ln\binom{3N_T}{N_T}\right] - \frac{k_B T}{N_T}\ln\binom{N_T(2+4x)}{3xN_T}$$

which yields an equilibrium concentration of

$$x \sim \sqrt[3]{4}/3\,\exp\left[-\Delta \mathrm{E}_0/3k_B T\right]$$

where $\Delta \mathrm{E}_0$ is the energetic cost to break a tetrahedron.

This corresponds to a concentration at 300 K between ~6% and ~0.5%, depending on the estimate taken for $\Delta \mathrm{E}_0$. In spite of this large concentration of Li4 the diffusivity is still low because most of the percolating paths for Li4 interstitials are suppressed by the presence of Li3 atoms fixed in tetrahedra. We speculate that the possible coexistence of partially occupied Li3 and Li4 sites might contribute to the change with temperature of the occupation of Li3 sites emerged from the Rietveld analysis [11]. We encourage new refinement of the diffraction data starting from our structural parameters in Tab. 4.2, that allows for a (small) partial occupation of the Li4 sites.

Based on *ab initio* simulations, we have identified a model for the local structure of the low temperature phase of lithium imide (Li_2NH). Atomic positions coincide with those inferred from diffraction data but partial occupations of Li sites have a strong nearest-neighbor correlation which solves the inconsistencies of previous proposed structures and fully agrees with experimental data available as discussed in Chapter 2.

As one more test we calculated the IR-spectrum by means of harmonic phonons. The absorption coefficient for the ordinary wave is given by

$$\begin{aligned}\alpha_\perp(\omega) &= \frac{\omega}{nc}\mathrm{Im}\left[\epsilon_\perp(\omega + i\gamma, \gamma \to 0)\right] \\ &= \frac{2\pi}{V_0 nc}\sum_{j=1}^{\nu}\left|\sum_{k=1}^{N}\mathbf{Z}\cdot\frac{\mathbf{e}(j,k)}{\sqrt{M_k}}\right|^2 \delta(\omega-\omega_j)\,. \end{aligned} \tag{4.2}$$

Table 4.4: Energetics comparison between our disordered $Fm\bar{3}m$ and previously suggested crystal structures for the LT phase of Li_2NH. The free energies reported here have been calculated considering the ZPE and harmonic contribution (see also [62]).

Li_2NH structure	Space group	$\Delta F_{@298K}$ [kJ mol^{-1}f.u.$^{-1}$]
HH	$Imma$	0.0
MOW	$Pnma$	-1.4
MC	$Pbca$	-3.8
Our	disordered $Fd\bar{3}m$	-1.7

The sum over k runs over the N atoms in the unit cell with mass M_k. $\mathbf{e}(j,k)$ and ω_j are the eigenstates and eigenvalues of the dynamical matrix at the Γ point, c is the velocity of light in vacuum and n is the refractive index. We approximated the δ-function by Lorentzian functions as

$$\delta(\omega-\omega_j)=\frac{4}{\pi}\frac{\omega^2\gamma}{\left(\omega^2-\omega_j^2\right)^2+4\gamma^2\omega^2}\,. \tag{4.3}$$

We did not calculate the Born effective charges and instead used qualitative diagonal **Z** matrices corresponding to the following charges: +1 on Li, +1 on H and -2 on N atoms, respectively. In Fig. 4.7 we report the calculated IR spectrum and a zoom at the high frequencies of both the calculated and the experimental IR spectra. Of course, we do not have agreement with experiment in term of the intensities of peaks because we used only a qualitative description of the charges however our calculations correctly reproduces the positions of the experimental peaks (cf. Figs. 4.7(b) and 4.7(c)).

4.2 Nuclear quantum effects

As a further check of the reliability of the structure for the low temperature phase of Li_2NH we proposed in the previous section, we computed the momentum distribution of the protons so as to compare it with experimental data from neutron Compton scattering collected by an experimental group with whom we were collaborating. Nuclear quantum effects have been included using a new recently developed method [96, 97, 98] which allowed us to perform simulations in an inexpensive way (cf. Chapter 3). In fact, within a stochastic molecular dynamics framework based on generalized Langevin equations it is possible to model to a good approximation nuclear quantum effects at negligible additional effort with respect to purely classical dynamics. Preliminary tests based on empirical force fields demonstrated satisfactory agreement with path integral molecular dynamics (PIMD) and experimental results [97, 98].

An additional advantage of this approach is that the quantum momentum distribution is reproduced as well as the quantum atomic configurations. In contrast, computing

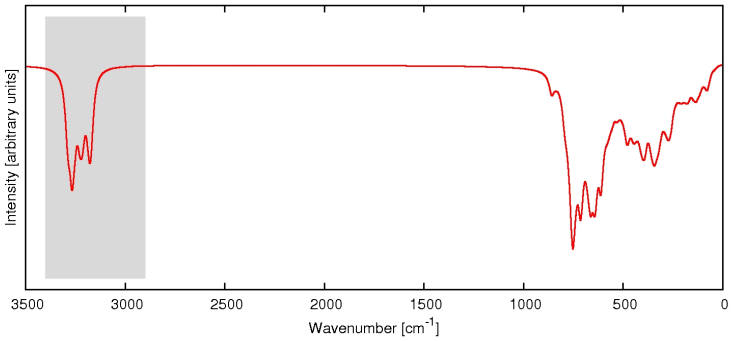

(a)

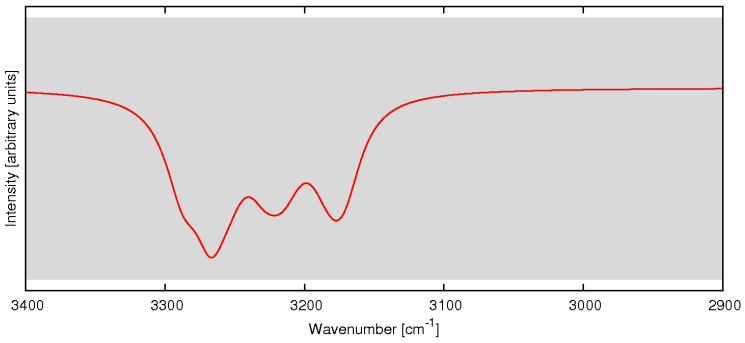

(b)

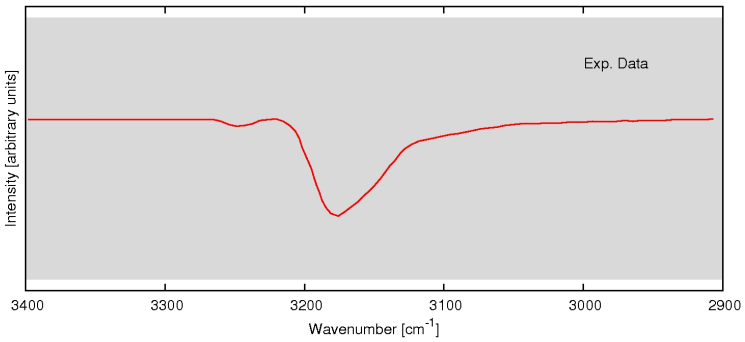

(c)

Figure 4.7: (a) Infrared absorption spectrum of Li_2NH as calculated by means of harmonic phonons. (b) and (c) Zoom of the region at high frequencies (2900–3400 cm^{-1}) for both the theoretical and the experimental IR spectra, respectively.

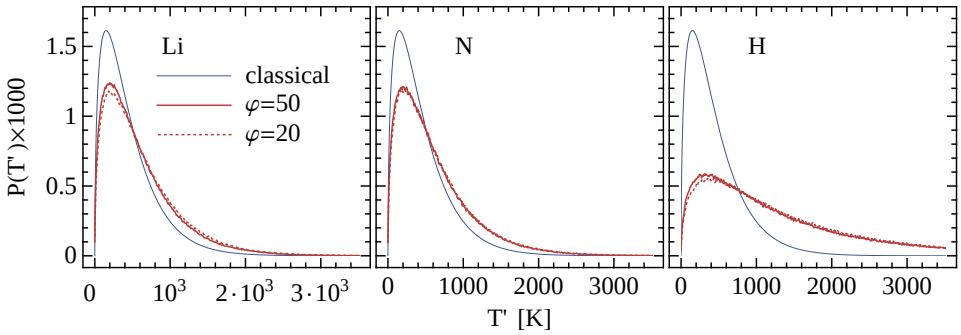

Figure 4.8: Comparison of the distribution of kinetic temperature, as computed separately for individual atomic species, for a purely classical (blue line) and two quantum thermostatted simulations of Li_2NH. The continuous red line corresponds to $\varphi = 50$, while the dotted red line to $\varphi = 20$.

the momentum distribution within a path integral formalism [102, 103] requires special techniques and, despite recent developments [104], further increases the computational effort.

Simulations were performed using the supercell containing 192 atoms and choosing, among the possible degenerate configurations for Li_4-clusters, the configuration shown in Fig. 4.4 on page 56. Starting from this structure we performed Born-Oppenheimer molecular dynamics simulations within the DFT-GGA framework (cf. also previous section). Thermal averages were performed over 15 ps of trajectory following 5 ps that were used for equilibration at $T = 300$ K.

Nuclear quantum effects were treated by means of a quantum thermostat which is based on a bespoke generalized Langevin equation containing correlated noise. This stochastic process is designed to mimic the quantum mechanical phase space distribution in the harmonic limit. The resulting non-equilibrium dynamics samples a stationary distribution which is a good approximation of the quantum mechanical one in fairly anharmonic systems as well. This result is achieved without requiring any preliminary information, except for an upper-bound estimate of the stiffest vibrational mode of the system (cf. Chapter 3 for technical details of the method and calculations).

In Fig. 4.8 we show the kinetic temperatures computed for each element separately we obtained from a number of quantum thermostatted *ab initio* molecular dynamics simulations using different choices for the GLE parameters. This analysis shows that nuclear quantum effects are very significant for hydrogen atoms. Here the computed kinetic temperature is 858 K. A deviation from the classical value is present also for the less light elements, specifically we found a temperature of 415 K for Li atoms and 410 K for N (which is heavier but is a participant in the stiff N–H stretching mode).

Before discussing the comparison with the experimental proton momentum distribution, it is necessary to stress that the presence of anharmonic wagging modes of the imide groups makes a quasi-harmonic treatment inappropriate. This is apparent in Fig. 4.9 where we compare the radial distribution function of the N–H group as computed

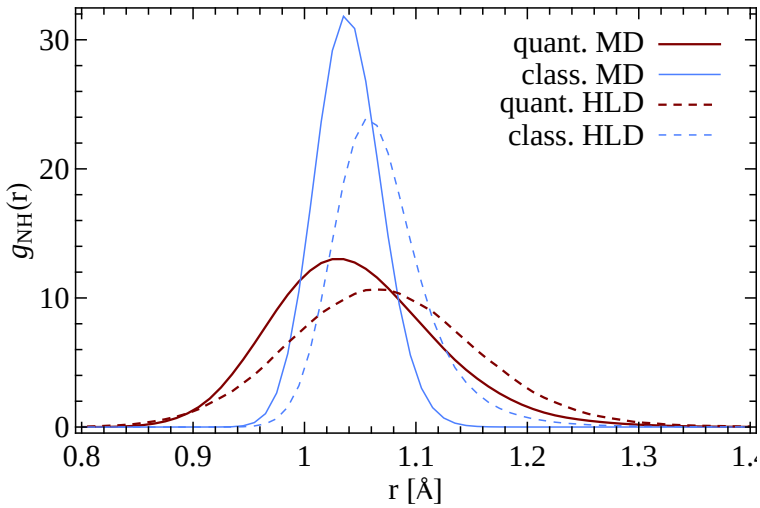

Figure 4.9: Comparison between the intramolecular peak of the N–H radial distribution function, as computed from molecular dynamics (MD) and harmonic lattice dynamics (HLD) with and without considering nuclear quantum effects. Note that because of strong anharmonicities the classical HLD provides an unsatisfactory description of this system. A similar discrepancy is found when comparing the quantum thermostat results and HLD with the Bose-Einstein occupations.

from molecular dynamics and from the harmonic normal modes (cf. also Ref. [105, 106]). The same figure also highlights the importance of nuclear quantum effects, which dramatically modify the typical fluctuations of the imide bonds. Harmonic phonons are computed by finite differences – *i.e.* displacing each atom in positive and negative x, y, and z direction by a distance of 0.01 a.u., as implemented in the CPMD code. The pair correlation function,

$$g_{\mathrm{NH}}(r) = \frac{1}{N_N \rho_H} \sum_{I,J} \langle \delta(\mathbf{r} + \mathbf{R}_I - \mathbf{R}_J) \rangle \tag{4.4}$$

(where ρ_H is the average density of atomic species H), were computed from harmonic phonons and Bose-Einstein distributions. In fact, the δ-functions are replaced with Gaussian functions with a variance σ^2 given by

$$\sigma^2 = \langle [\mathbf{d} \cdot (\mathbf{u}_N - \mathbf{u}_H)]^2 \rangle \tag{4.5}$$

where $\mathbf{u}_N$ ($\mathbf{u}_H$) is the displacement of the N (H) atom with respect to the equilibrium position $\mathbf{R}_N$ ($\mathbf{R}_H$), and $\mathbf{d}$ is a unitary vector along the direction of $\mathbf{R}_I - \mathbf{R}_J$. The brackets $\langle \cdots \rangle$ indicate a thermal average obtained as follows

$$\langle u_{Ni} u_{Hj} \rangle = \sum_m \frac{\hbar}{\omega_m} \frac{e^m_{(N,i)}}{\sqrt{M_N}} \frac{e^m_{(H,j)}}{\sqrt{M_H}} \left[n_B \left(\frac{\hbar \omega_m}{k_B T} \right) + \frac{1}{2} \right] \tag{4.6}$$

where i and j label the Cartesian directions, M_N and M_H are the masses of N and H, while ω_m and the $\mathbf{e}^m$ are the frequencies and the eigenvectors of the mth harmonic phonons. The temperature dependence enters through the Boson occupation number $n_{\mathrm{B}}(E) = [\exp(E/k_{\mathrm{B}}T) - 1]^{-1}$.

Both deviations from the classical values of kinetic temperatures and the modifications of typical fluctuations of N–H distances during the dynamics illustrate the importance of nuclear quantum effects in determining the properties of Li_2NH such as the temperature at which the transition between the low-temperature and high-temperature phases occurs (see later).

Computing the proton momentum distribution from the quantum – thermostatted dynamics is straightforward. In fact, the thermostat has been designed to yield the correct momentum and position distribution in the harmonic limit, and has proven to work also in the anharmonic case. Thus we only need to collect the momentum histogram to obtain the three-dimensional PMD, which is plotted in Fig. 4.10.

The anisotropy of $n(\mathbf{p})$, which is a purely quantum mechanical effect, reflects the symmetry of the local environment of protons inside the crystal. Consequentially we should be able to detect bonds aligned along the $\langle 111 \rangle$ direction of the nitrogen antifluorite sublattice, which point towards Li vacancies (cf. Refs. [11, 62]). For these reasons in principle the $n(\mathbf{p})$ could be a very powerful tool to discriminate among the different LT crystal structures proposed for Li_2NH. In fact, as shown in Fig. 4.11, the different symmetry of the local environment of protons inside the HH, MOW, MC structures, is qualitatively reflected by the shapes of the isosurfaces of $n(\mathbf{p})$. Unfortunately for Li_2NH it has not been possible to measure the directionally-resolved $n(\mathbf{p})$ but, the experimental group we collaborated with (A. Pietropaolo, D. Colognesi, A. Nale, M. Catti) has been able to measure the spherical average of $n(\mathbf{p})$ at 300 K.

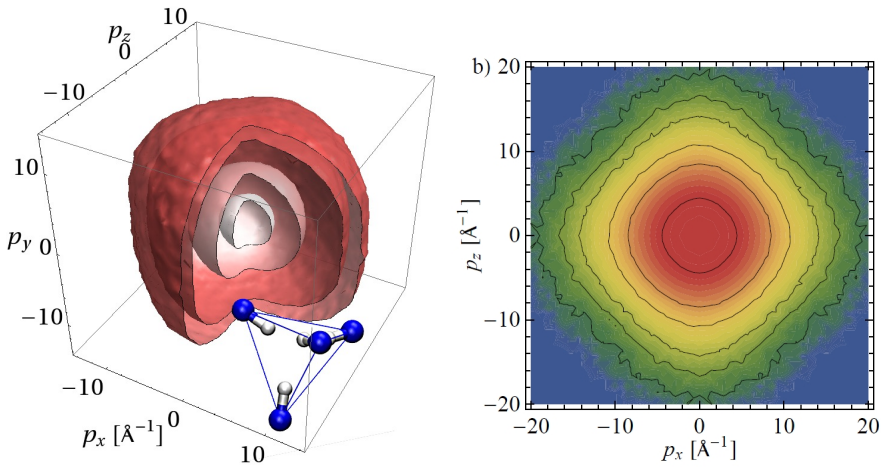

Figure 4.10: Three/Two-dimensional proton momentum distribution for the low temperature phase of lithium imide. (a) Isosurfaces enclose 95%, 90%, 50% and 10% of the probability density. The arrangement of the hydrogens around a Li vacancy, aligned along the ⟨111⟩ axes, is also reported, relative to the Cartesian reference. (b) A contour plot of the 2D PMD computed on the xz plane. Contour lines are traced for $n(p_x, p_z) = 5\times10^{-3}, 10^{-3}, 5\times10^{-4}, 10^{-4}, 5\times10^{-5}, 10^{-5}$ Å^2.

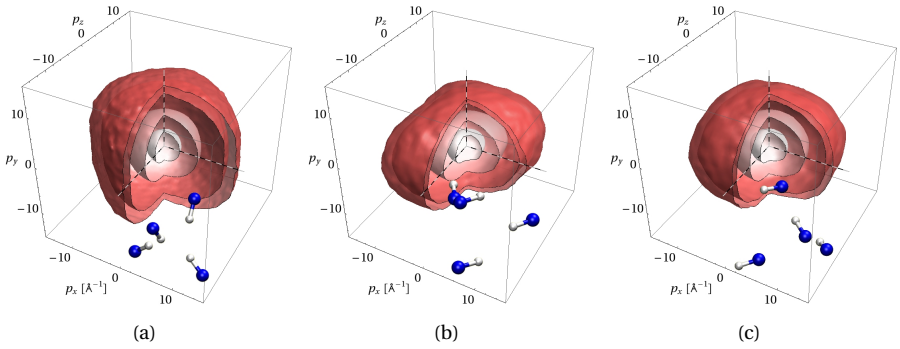

Figure 4.11: The 3D proton momentum distribution reflects the local environment experienced by hydrogen atoms. Here a 3D representation of $n(\mathbf{p})$ isosurfaces for (a) $Fd\bar{3}m$, (b) $Pnma$ and (c) $Pbca$ structures for the LT phase of Li_2NH.

In fact, to access measurements of the directionally-resolved $n(\mathbf{p})$ a large single-crystal sample is necessary but this is very difficult to obtain.

To compare with the powder sample experimental data, we spherically averaged the three dimensional PMD. As can be seen from Fig. 4.12, there is a satisfactory agreement between experiments and theory. In particular, we observe that quantum-thermostatted simulations match experimental data better than the results from the quantum harmonic approximation. To quantify the discrepancy with experiments, and to extract information relevant to the structural model of Li_2NH, we fitted the experimental and theoretical PMD's with an anisotropic Gaussian model. We assumed a different spread in the directions parallel and perpendicular to the N–H bond[107, 108], resulting in

$$n(\mathbf{p}) \propto \exp\left(-\frac{p_z^2}{2\sigma_\parallel} - \frac{p_x^2+p_y^2}{2\sigma_\perp}\right) \tag{4.7}$$

which was then spherically averaged.

The resulting fit matches both curves very well, with values of adjusted R^2 greater than 0.999. The fit yields the parameters $\sigma_\parallel = 6.49$ Å^{-1} and $\sigma_\perp = 3.15$ Å^{-1} for the theoretical PMD, and $\sigma_\parallel = 5.77$ Å^{-1} and $\sigma_\perp = 3.70$ Å^{-1} for the experimental one.

The discrepancy is certainly larger than the experimental error bar, however the anisotropy in the PMD is correctly captured, and the spread in the direction parallel and perpendicular to the bond is qualitatively reproduced. This is indeed a remarkable result for an approximate model of the nuclear quantum effect such as the one used in the present work, which can be applied with no computational overhead with respect to standard *ab initio* molecular dynamics. While it is difficult to assess the uncertainty in our theoretical results, a possible approach to gauge the error is to repeat the simulations with a different set of noise parameters. We did so using the parameters $\varphi = 20$ (see Chapter 3 of methods), and obtained $\sigma_\parallel = 6.31$ Å^{-1} and $\sigma_\perp = 3.40$ Å^{-1}. The comparison with the results obtained using $\varphi = 20$ sets a lower bound for the error at about 10%. Although the difference between the PMD obtained for different structures proposed for Li_2NH (our structure and those proposed in Refs. [11, 63, 64]) is smaller than our error bar on the spherically-averaged distribution, the difference in structure reflects in qualitatively-different three-dimensional $n(\mathbf{p})$. However, for the reasons discussed in section 2.3, the other proposed structures have to be dismissed because of their worse agreement with diffraction data.

The proton momentum distribution within harmonic lattice dynamics

Computing the quantum mechanical proton momentum distribution within harmonic lattice dynamics is straightforward, but we report here the procedure, for completeness. At first, we observe that the quantum momentum distribution can be written as a multivariate Gaussian, with frequency-dependent widths along the normal modes obtained from classical lattice dynamics. Let the indexes α, m, i label atoms, phonons and Cartesian coordinates respectively, and ω_m and $e^m_{(\alpha i)}$ be the frequency and the components of the m-th normalized eigenvector of the dynamical matrix. The covariance matrix which describes the multivariate-Gaussian distribution of momenta at temperature T reads

$$\langle p_{\alpha i} p_{\beta j}\rangle = \hbar\sqrt{M_\alpha M_\beta}\sum_m e^m_{(\alpha i)} e^m_{(\beta j)} \frac{\omega_m}{2} \coth\frac{\hbar\omega_m}{2k_B T} \tag{4.8}$$

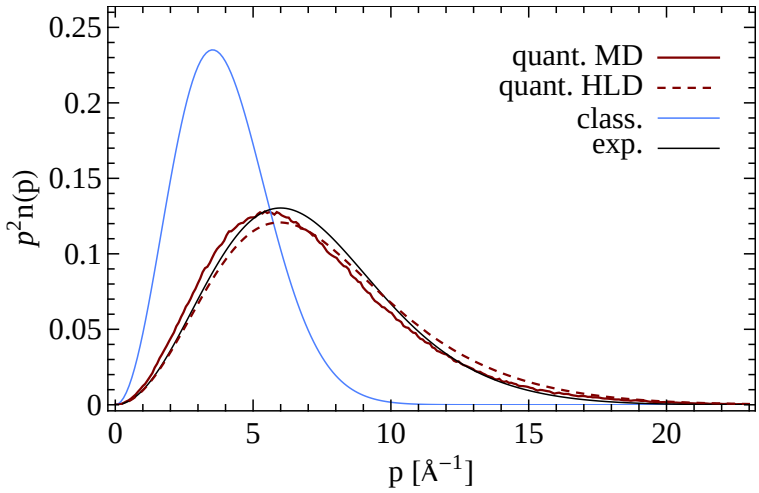

(a)

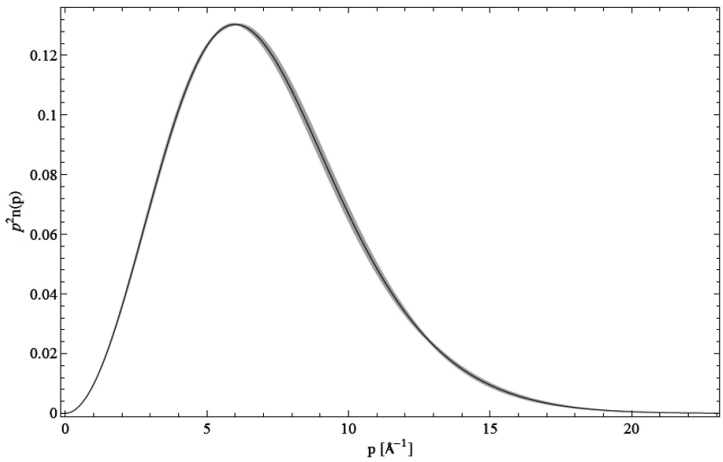

(b)

Figure 4.12: (a) Comparison between the spherically-averaged proton-momentum distribution expected for a classical system and from harmonic lattice dynamics at $T = 300$ K, the PMD measured from a lithium imide sample and that computed from quantum – thermostatted molecular dynamics. (b) Spherically-averaged proton momentum distribution for Li_2NH, as measured by inelastic neutron scattering. The experimental uncertainty is reported as a shaded area around the best estimate curve.

Then, one must consider that the scattering is incoherent, and will result from the superposition of the contributions of individual protons, which are described by the marginal probability distribution, which is given by the 3×3 matrices $C^{\alpha}_{ij} = \langle p_{\alpha i} p_{\alpha j} \rangle$.

The three dimensional PMD finally reads

$$n(\mathbf{p}) \propto \sum_{\alpha} \frac{1}{\sqrt{\det(\mathbf{C}^{\alpha})}} e^{-\frac{1}{2}\mathbf{p}^{T}[\mathbf{C}^{\alpha}]^{-1}\mathbf{p}} , \tag{4.9}$$

which can be spherically averaged to give $n(p)$.

4.3 Phase transition and high temperature phase

In the present section we investigate the structure of the high temperature phase of Li_2NH by means of *ab initio* simulations. As discussed in section 2.3 neutron diffraction measurements on Li_2NH [11] confirmed an anti-fluorite structure ($Fd\bar{3}m$) for the high temperature phase (400 K) with D atoms randomized over the 192l positions (although structure refinements with positions 96k or 4a gave similarly good fitting of the experimental data) [11]. Very recently, molecular dynamics simulations by Araujo *et al.* [109] with a 128-atoms supercell revealed the formation of Frenkel pairs and fast diffusion accompanied by fast NH rotations above 400 K starting from several initial orientations of the NH groups according to different proposals for the $Fm\bar{3}m$ phase. At the moment there is no experimental data on ionic mobility at high temperature to confirm the existence of a superionic state. Moreover, it is not clear from Ref. [109] whether fast Li conduction might also be observed by heating the low temperature $Fd\bar{3}m$ phase. To clarify this issue, we here report on simulations at several temperatures starting from a 192-atoms model of the $Fd\bar{3}m$ phase where Li interstitials form tetrahedral clusters as already discussed in section 4.1.

4.3.1 Molecular dynamics simulations

Our preliminary *ab initio* MD simulations at 400 K (128-atoms supercell) using PBE or BLYP functionals [110, 111] revealed that the $Fm\bar{3}m$ phase is locally unstable with respect to the formation of Li Frenkel pairs when H atoms are randomly placed in positions 48h or 24e as proposed in earlier experimental XRD studies [112]. Frenkel pairs spontaneously form in the simulation at 400 K. The four nearest neighbor NH groups point tetrahedrally towards the newly formed vacancy restoring the local environment of the low temperature $Fd\bar{3}m$ phase. At the same time, other NH groups not nearest neighbors to vacancies rotate very rapidly, where rapidly here means with a rotation period comparable to the value expected for a free rotator at the given temperature. These rotations of the NH groups are strongly coupled with the Li vibrations around their anti-fluorite sites. By fixing the positions of the Li atoms the librational motions of the NH groups were observed to be drastically reduced.

The same Li Frenkel pairs are the source of the superionic properties of Li_2NH (above 400 K) as revealed by means of *ab initio* MD in Ref. [109]. However, this behavior might be the result of the choice of a metastable initial configuration. To confirm the superionic behavior of Li_2NH at high temperature it is important to assess whether or not fast Li conduction is also observed on heating the low temperature $Fd\bar{3}m$ phase.

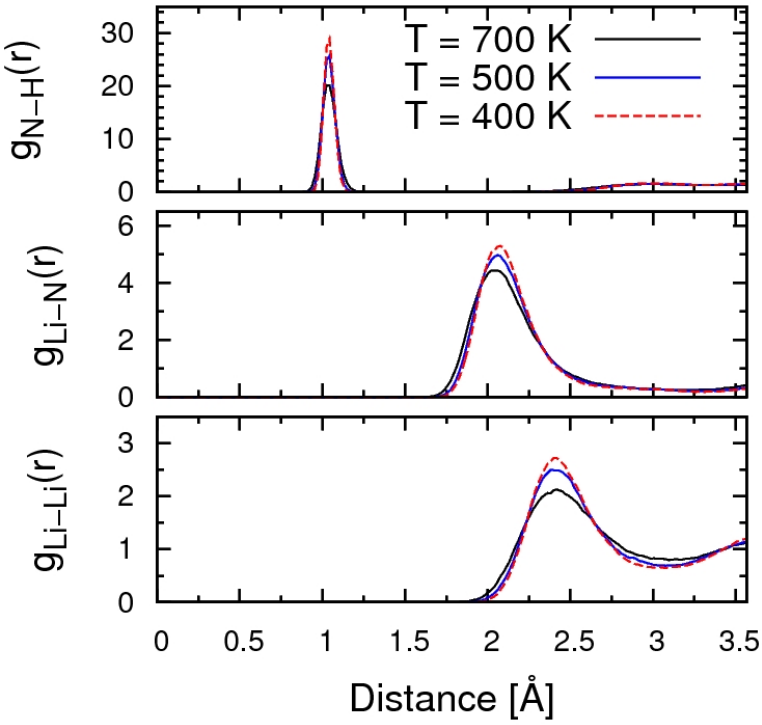

Figure 4.13: Partial pair correlation functions (N-H, Li-N, Li-Li) of Li_2NH at 700, 500 and 400 K, obtained by heating the low temperature 192-atoms $Fd\bar{3}m$ phase at 700 K and then quenching at 500 and 400 K.

To clarify this issue, we performed simulations at 300, 400, 500, 600 and 700 K (each ≥ 20 ps long) starting from a 192-atoms model of the $Fd\bar{3}m$ phase where Li interstitials form tetrahedral clusters as explained in section 4.1 (see also Fig. 4.4).

At 600 and 700 K the tetrahedral clusters of interstitial atoms, described in section 4.1 break down and the vacancies and Li interstitial start diffusing as reported in Ref. [109]. However, on quenching the system down to 500 K and then to 400 K, we observed that NH groups progressively orient themselves toward neighboring vacancies in a local geometry similar to that of the low temperature $Fd\bar{3}m$ phase (cf. also Fig. 4.14). These vacancies, make up ~70% of the total number of vacancies, and have low mobilities, due to the tetrahedral coordination by NH groups.

In contrast, Li interstitials originating from the breaking down of the tetrahedral clusters are very mobile. The pair distribution function and the angular distribution of NH orientations as a function of the temperature are reported in Figs. 4.13 and 4.14. The appearance of an angular ordering at low temperature is very clearly demonstrated by Fig. 4.14. The disappearance of the tetrahedral Li interstitial clusters results in a decrease of the number of vacancies from the total of 16 in a $Fd\bar{3}m$ disordered geometry with 192-atoms (48 formula units) (as one can see in Fig. 4.15(a) where the distribution of the

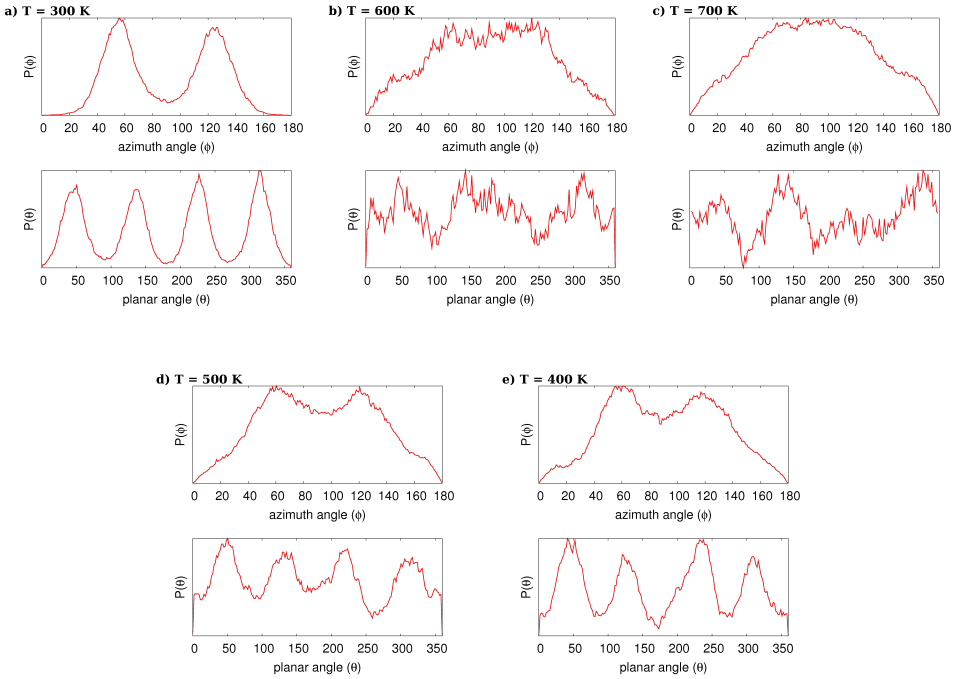

Figure 4.14: Distribution of the orientation of NH groups in Li_2NH at a) 300, b) 600, c) 700 K and d) 500, e) 400 K, obtained by heating the low temperature 192-atoms disordered $Fd\bar{3}m$ phase at 700 K (600 and 300 K) and then quenching at 500 and 400 K. The spherical polar angles are defined with respect to the abc (xyz) orthogonal axis of the fcc sublattice of N.

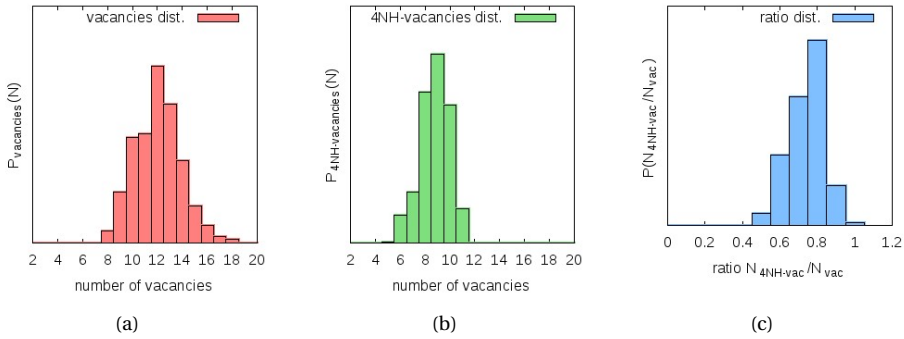

Figure 4.15: (a) Distribution of the total number of vacancies and (b) of the vacancies coordinated by four NH groups in a *Imma*-like geometry in the simulation at 500 K, 100 ps long. (c) Ratio of the two distributions of panel (a) and (b) ($N_{4NH\text{-}vac}/N_{vac}$).

total number of vacancies is shown). The majority of vacancies are now coordinated by NH groups and sometimes even reach the maximum possible value of 12 (48 NH groups in our cell).

At T = 500K the distribution of the total number of vacancies and of those coordinated by four NH groups, as in the LT geometry, are reported in 4.15(a) and 4.15(b) together with the ratio N_{4NH}/N_{vac}, Fig. 4.15(c). On average we observe 12 vacancies of which 9 are coordinated by four NH groups. These vacancies are identified according to the geometrical definition given in appendix A.

To investigate the vacancy diffusion we had to discriminate between real diffusive jumps and fast forward-backward jumps (and/or vacancy annihilation). To this end a vacancy was identified when the corresponding site was empty for a time longer than the minimum residence time for the vacancy, τ_m. By plotting the number of events (vacancy jump or creation/annihilation) N_v as a function of τ_m (averaged over the run) one obtains an exponential function

$$N_v \propto \exp(-\tau_m/\tau) \tag{4.10}$$

which defines an average minimum residence time τ to identify a vacancy in its site. By setting $\tau_m = \tau = 8.3$ ps in our definition of a vacancy (see above) we identified ~80 events of vacancy creation/annihilation and ~10 vacancy jumps in an overall simulation time of 100 ps at 500 K. In contrast interstitial atoms diffuse very fast (with 6 jumps in 20 ps).

The above results, on a 100 ps run of MD, are obtained on a smaller supercell of 128 atoms which, due to the disappearance of Li tetrahedral clusters, is also compatible with the structure of the high temperature phase.

As proposed in the Ref. [109], the order-disorder transition at 356 K could coincide with the onset of superionicity. However, we here propose that the high temperature $Fm\bar{3}m$ phase corresponds to a disordered version of the *Imma* phase by Herbst and Hector with a finite concentration of mobile Li interstitials and Li vacancies. These two types of defects diffuse on very different time scales with an extremely fast (superionic)

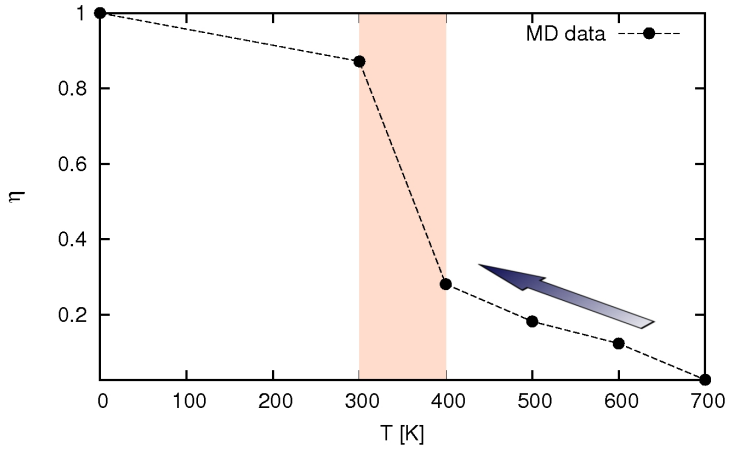

Figure 4.16: Average Li-cluster number, phenomenological order parameter as measure of structural phase transition in Li_2NH. Here N is the maximum number of Li-clusters that can exist according to stoichiometry, in our case 4. n_i Li-cluster number ($n_i = 0,1,\ldots,4$), τ_i time in which n_i are observed and t total time of simulation.

motion of Li interstitial (with 6 jumps in 20 ps) and a slower diffusion for vacancies (less than one jump per vacancy in 20 ps). The tetrahedral Li clusters are broken down by both the diffusion of Li interstitials and through the formation of Li vacancies. These features may still form at high temperature however they will have a very short life time.

The superionicity is given by Li interstitials that in our model of Li_2NH phase come from the breaking of Li-clusters at high temperature (above 400 K). On the other hand, the presence of these clusters prevents Li diffusivity in the low temperature phase. Some tetrahedral clusters also form by quenching at 400 and 500 K the HT structure at 700 K, although they experience a short lifetime. The average number of Li-clusters can be seen as an order parameter for the superionic transition. We count the number of Li-clusters as follows. We considered a spherical volume around each possible center of tetrahedral cluster. Therefore, a Li-cluster is detected when a inner spherical volume of 1.1 Å of radius is empty and 4 Li atoms are inside the volume between the previous sphere and an outermost sphere of radius 1.9 Å. Fig. 4.16 shows the behavior of the phenomenological order parameter defined as the ratio between the observed average number and the maximum number of Li-clusters, N, compatible with the size of supercell and the stoichiometry

$$\eta = \frac{1}{N}\frac{\sum_{i=1}^{N} n_i \tau_i}{t} .$$

The order parameter is $\eta \simeq 1$ (4 Li-clusters per cell) at room temperature in the low temperature phase and $\eta \simeq 0$ at 700 K where all clusters are broken. By quenching from 700 K, the fraction of tetrahedral Li-clusters slightly increases by increasing the temperature.[1]

[1] at 300 K the value of η a bit lower than 1 is due to the choice of the algorithm to count the number of

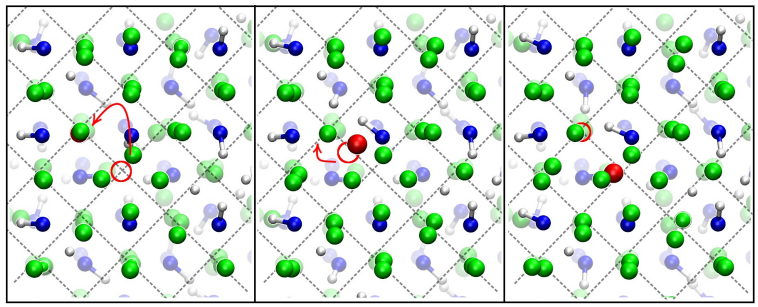

Figure 4.17: Snapshot of the initial, saddle point and final configurations of a vacancy jump in Li_2NH. The minimum energy path optimized by NEB was obtained starting from the MD trajectory at 500 K.

Still, at high temperature the NH groups preferentially point tetrahedrally towards the nearest vacancies, but for a fraction (about 30%) of the NH which are rapidly rotating. This picture is consistent with the experimental assignment of the H to the 192l positions in the $Fm\bar{3}m$ phase [11]. Li interstitials occupy the octahedral sites since tetrahedral clusters are dissolved above 400 K. An instantaneous, local snapshot of the high temperature phase might thus be still well described by the $Imma$ phase originating from the $Ima2$ structure by Herbst and Hector. Due to the diffusion of Li interstitials and vacancies, the high $Fm\bar{3}m$ symmetry structure is detected by diffraction which probes a space- and time-averaged structure.

We computed the Li self-diffusion (tracer) coefficient from the mean square displacement and the Einstein relation $\langle x^2 \rangle \rightarrow 6tD_{\mathrm{Li}}$ which yields $D_{\mathrm{Li}} = 1.44 \cdot 10^{-6}$ cm^2/s and $D_{\mathrm{Li}} = 3.26 \cdot 10^{-6}$ cm^2/s at 400 K and 500 K, respectively. These values are a factor of two lower than those reported in Ref. [109] which, however, might not correspond to a disordered "$Imma$" phase. The diffusion of Li interstitials follows the exchange mechanism with the Li on the anti-fluorite sites already discussed in section 4.1.

A calculation in the 128-atoms supercell with the Γ-point of the $Imma$ phase yielded an activation energy for the diffusion of a Li interstitial of as low as 0.06 eV, equal to the value reported in Ref. [109]. By refining the BZ integration on a $2 \times 2 \times 2$ k-points mesh the activation energy raises to 0.11 eV. On the other hand the activation energy for the jump of a vacancy initially coordinated tetrahedrally by four NH groups is as large as 0.33 eV. Snapshots of the initial, saddle point and final configurations for a vacancy jump are reported in Fig. 4.17. The minimum energy path optimized by NEB was obtained starting from the MD trajectory at 500 K. We remark that in this process with the minimum jump length the vacancy moves from a site tetrahedrally coordinated by four NH groups to a site where this coordination is not possible. In other words, the diffusion of a vacancy reasonably implies that some vacancy must be temporally not coordinated by 4 NH.

The high energy barrier for vacancy diffusion prevents the observation of vacancy jumps at 400 K in the short run of our simulation. Still the time scale for vacancy diffusion at 400 K might be sufficiently short for the diffraction experiments to average over many

Li-cluster.

different vacancy distributions. As a result, due to Li interstitials and vacancies, the high temperature $Fm\bar{3}m$ symmetry is detected by diffraction probes as a space- and time-averaged structure.

5

Lithium amide / imide transformation mechanism

In this chapter we present our results on the modeling of the decomposition of $LiNH_2$ into Li_2NH and ammonia which is thought to be the first step in the amide/imide transformation. As discussed in section 2.4 time resolved X-ray diffraction measurements revealed a continuous transformation of $LiNH_2$ into Li_2NH through sub-stoichiometric phases. In this work David *et al.* [17] suggested that Li Frenkel pairs are the key factor for ammonia formation in bulk $LiNH_2$ and for the whole decomposition process. On the other hand, other kinetic experiments performed on ball-milled samples of $LiNH_2$ revealed a different mechanism for Li_2NH growth [18]. Here, Shaw and coworkers suggested that Li_2NH grows as a shell around a shrinking core of $LiNH_2$ and demonstrated that the rate-determining step for the whole process of decomposition is the migration of ammonia inside the shell of Li_2NH. These two different proposed mechanisms seem to provide conflicting scenarios for the decomposition pathway. However, different transformation pathways might actually be a consequence of the different preparation conditions of the material. The $LiNH_2$ / Li_2NH mixture used in the kinetic measurements was ball-milled while the samples used in X-ray diffraction measurements were not.

In order to provide a theoretical support for the two step decomposition mechanism

$$2\,LiNH_2 \longrightarrow Li_2NH + NH_3 \tag{5.1}$$

$$NH_3 + LiH \longrightarrow LiNH_2 + H_2 \tag{5.2}$$

and so as to clarify the role of surfaces in this process, we performed *ab initio* calculations and calculated activation energies for different elementary steps that we hypothesize to be crucial for the ammonia-mediated transformation path focusing in particular on reaction (5.1).

We first analyzed the formation of ammonia via a proton transfer between two NH_2^- groups in the presence or absence of a Li Frenkel pair in the bulk and at the surface of $LiNH_2$. The diffusivity of H^+ (i.e. NH_3 via a Grotthuss mechanism), H^+ vacancy (NH^{2-})

and Li^+ species in $LiNH_2$ and Li_2NH were then computed to contrast the alternative scenarios described in section 2.4. The H^+ and Li^+ transfer across the $LiNH_2/Li_2NH$ interface was also investigated as well as the ammonia desorption from the Li_2NH and $LiNH_2$ surfaces. The scenario for the decomposition mechanism of $LiNH_2$ emerging from the simulations actually suggests that the transformation path depends on the surface-to-volume ratio. The formation of sub-stoichiometric phases is possibly favored in bulk material with a small surface-to-volume ratio, while the direct formation of imide is favored in the presence of small crystallites (large surface-to-volume ratio) which transform according to the core-shrinking model of Ref. [18].

Our results thus allow us to reconcile the apparently contradicting results on the presence of sub-stoichiometric phases inferred from X-ray data in Ref. [17] with the kinetic data of Ref. [18] which suggests the growth of a Li_2NH shell outside a $LiNH_2$ shrinking core. As a side product, the simulations provide a comprehensive description of defect formation and diffusivity in the bulk and at the surface of Li amide and imide which is open to experimental verification, *e.g.* by measurements of the ionic conductivity.

Hereafter, we discuss separately the processes taking place in bulk and at the surface of $LiNH_2$, the processes taking place in the bulk and at the surface of Li_2NH, and then the processes that take place at the $LiNH_2$ / Li_2NH interface. Before presenting our results on the transformation mechanism in the following we report the computational details adopted throughout this work.

Computational details Calculations have been performed within density functional theory, using the energy functional with generalized-gradient corrections proposed by Perdew-Becke-Ernzerhof (PBE) [78]. We used the PWscf code from the Quantum-Espresso package [113] for geometry optimizations by expanding Kohn-Sham orbitals in a plane-wave basis set up to a kinetic-energy cutoff of 50 Ry. Ultrasoft pseudopotentials [100] were used for H and N while a Goedecker-type pseudopotential [85, 86] with three valence electrons was used for Li. The minimum energy path for different reactions was identified by using the Nudged Elastic Band Method (NEB) [92, 93] which provides geometries and activation energies for the transition states. Climbing image and variable springs were used, with k_{max} = 0.2 a.u. and k_{min} = 0.1 a.u.. A minimization scheme was applied until the residual total forces acting on each image in the direction perpendicular to the path were smaller than 0.05 eV/Å. For what follows positive reaction energies correspond to endothermic processes. Most calculations were performed using only the Γ point in the Brillouin Zone (BZ) integration of a 128 or 256-atom supercell of $LiNH_2$. Higher accuracy in the BZ turned out to be necessary only for a few Li_2NH calculations. In all cases convergence of the activation and formation energies with respect to BZ integration up to few tens of meV was checked with $2 \times 2 \times 2$ Monkhorst-Pack (MP) meshes [80] in 128 atoms supercells. For selected processes, we computed zero point energy corrections (ZPE) using the phonons at the supercell Γ-point, calculated within density functional perturbation theory [114, 115] as implemented in the Quantum-Espresso package [113]. Reaction rates ν were computed from activation energies (E_a) and phonons within harmonic transition state theory (h-TST) as $\nu = \nu^\star \exp(-E_a/k_B T)$.

In the classical limit

$$\nu^\star = \frac{\prod_j \nu_j^{(R)}}{\prod_j \nu_j^{(TS)}} \tag{5.3}$$

where $\nu_j^{(R)}$ and $\nu_j^{(TS)}$ are the positive eigenvalues of the Hessian matrix for reactant and transition states, respectively.

The Quickstep scheme [82, 83], as implemented in the CP2K suite of programs [84], was used for selected geometry and NEB optimizations and for Born-Oppenheimer *ab initio* molecular dynamics simulations. In the Quickstep approach the Kohn-Sham orbitals are expanded on a Gaussian basis set, while an auxiliary plane-wave expansion of the electronic density is used to efficiently evaluate the Hartree part of the Coulomb interactions and the exchange-correlation energy. Goedecker-type pseudopotentials [85, 86] were used for all atoms in the CP2K calculations with triple-zeta plus polarization (TZVP) Gaussian basis sets. A kinetic cutoff of 100 Ry was used for the plane-wave expansion of the electronic density and BZ integration was restricted to the Γ point.

5.1 Defects and ammonia formation in bulk of $LiNH_2$

As discussed in section 2.2 $LiNH_2$ crystallizes in a body-centered tetragonal symmetry with a $I\bar{4}$ space group [50, 45]. The unit cell contains four formula units and the structure can be seen as a slightly tetragonally distorted anti-fluorite structure with the anionic face-centered-cubic sublattice fully occupied by NH_2 groups and the cationic sublattice (tetrahedral sites) half-occupied by Li in an ordered manner (see also Fig. 5.1). Theoretical and experimental data are in good agreement in assigning a N-H bond length that is approximately 0.2 Å longer than those previously reported by X-ray diffraction [116].

An equilibrium geometry was obtained by optimizing the c/a ratio and the internal positions at different volumes and by interpolating the resulting energy-volume data with a Murnaghan equation of state [117]. Structural properties are converged with a $2 \times 2 \times 2$ MP mesh as checked by calculations with up to $5 \times 5 \times 5$ meshes. The calculated bulk modulus and the derivative of the bulk modulus with respect to pressure at equilibrium are 24 GPa and 2.65, respectively. Experimental neutron scattering data [45] and calculated equilibrium lattice parameters and positions of the atoms independent by symmetry are compared in Tab. 5.1. Our calculated lattice parameters and atomic positions are very similar to previous *ab initio* data obtained with the same PBE-DFT functional used here [46, 47]. In order to verify the viability of the mechanism of formation of NH_3 promoted by Li Frenkel pairs suggested by David *et al.* [17] we computed the formation energy of Frenkel pairs and of NH_3 as described hereafter.

Li Frenkel pairs in $LiNH_2$ The formation energy of a Li Frenkel pair (V_{Li} plus a lithium interstitial Li_i) was computed as the sum of the formation energy E_f of the two isolated charged defects V_{Li}^- and Li_i^+ in supercells with 128 or 256 atoms. Corrections for band alignments (Δ_q) and long charge Coulomb interactions (E_{lat}^q) between the periodic images of the charged defects was included as in Ref. [118] by Freysoldt *et al.*:

$$E_f(x^q) = E_{tot}[x^q] - E_{tot}[\text{bulk}] - n\mu + q(\mu_F + E_v + \Delta_q) - E_{lat}^q \tag{5.4}$$

Table 5.1: Calculated structural properties of $LiNH_2$. Experimental neutron data from Ref. [45] are given in curly brackets, { }, and theoretical *ab initio* calculations data are reported in round brackets, ( ) [46, 47] (See Fig. 5.1 for the labeling of atoms independent by symmetry).

lattice parameters [Å]		$a = 5.051$ $\{a = 5.03442(24)\}$ $(a = 5.079)$		
		$c = 10.33$ $\{c = 10.25558(52)\}$ $(c = 10.113)$		
	atomic parameters			
atom	position	x	y	z
Li1	$2a$	0 {0} (0)	0 {0} (0)	0 {0} (0)
Li2	$2c$	0 {0} (0)	1/2 {1/2} (1/2)	1/4 {1/4} (1/4)
Li3	$4f$	0 {0} (0)	1/2 {1/2} (1/2)	0.0057 {0.00253} (0.0018)
N	$8g$	0.2267 {0.2286} (0.2253)	0.2478 {0.2499} (0.2480)	0.1149 {0.1158} (0.1155)
H1	$8g$	0.2304 {0.2429} (0.2392)	0.1204 {0.1285} (0.1337)	0.1928 {0.1910} (0.1999)
H2	$8g$	0.4074 {0.3840} (0.3949)	0.3406 {0.3512} (0.3603)	0.1215 {0.1278} (0.1198)

Ammonia formation in bulk $LiNH_2$

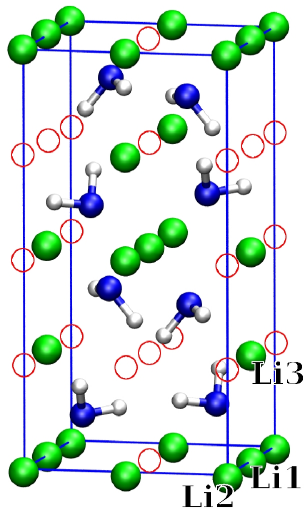

Figure 5.1: The crystal structure of $LiNH_2$. The conventional tetragonal unit cell is shown (eight formula units). Large green spheres represent Li atoms, small white spheres hydrogen atoms and the blue spheres nitrogens. Vacancies of Li in the ideal anti-fluorite structure are depicted by empty circles. The Li atoms independent by symmetry are labeled.

where μ is the chemical potential of the standard (metallic) state of Li, q is the charge of the defect (-/+1 for vacancy and interstitial respectively), μ_F is the Fermi level referred to the energy of the valence band maximum E_v and n is +1 for the interstitial and -1 for the vacancy (see App. B for details on the calculation and also Refs. [118, 119]). As interstitial sites, we considered both the empty tetrahedral sites and the octahedral sites of the NH_2 fcc-like sublattice. Li insertion in the octahedral site costs 0.2 eV more than the most favorable tetrahedral sites as discussed below. From now on we will therefore consider only tetrahedral empty sites for the location of Li interstitials. The formation energy of the unbound Frenkel pair (two isolated defects) turns out to be as large as 1.42 eV for the lowest energy sites of Li interstitial, $int1$, and Li vacancy, $vac1$, among the three possible tetrahedral sites for each defect depicted in Fig. 5.2. For less favorable sites the formation energy of a Frenkel pair increases at most by 0.30 eV. The bound Frenkel pair made of nearest neighbor Li vacancy and Li interstitial in the most favorable position costs instead only 0.97 eV as computed with both defects inside a 128-atoms supercell, at positions $int2$ for the interstitial and $vac1$ for the vacancy, cf. Fig. 5.2). The activation energy for the formation of a bound Frenkel pair is 1.15 eV.

The band alignment terms Δ_q in Eq. (5.4) introduce a large correction to the formation energy of the charged defects (up to 0.6 eV in the formation energy of the Frenkel pair) while the correction E^q_{lat} due to electrostatic interaction between the charged images is as small as 0.08 eV (in a 256 atoms cell). The formation energy of a neutral Li vacancy and neutral Li interstial are instead 3.56 eV and 0.72 eV respectively (calculated in a 128 atoms supercell).

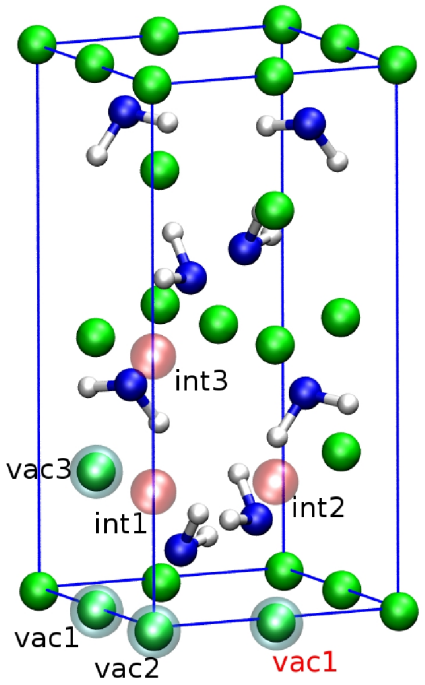

Figure 5.2: The three inequivalent sites for the position of a Li interstitial (*int1-3*) and Li vacancy (*vac1-3*). The lowest energy configuration for the interstitial is the site labeled *int1* while sites *int2* and *int3* are 0.14 eV and 0.01 eV higher in energy, respectively. The lowest energy configuration for the vacancy is the site *vac1* while the sites *vac2* and *vac3* are 0.16 eV and 0.01 eV higher in energy, respectively. The inequivalent positions of interstitials and vacancies in crystal units are: $int1$ (0.0, 0.0, 0.25), $int2$ (0.5, 0.0, 0.25), $int3$ (0.0, 0.0, 0.5), $vac1$ (0.5, 0.0, 0.0), $vac2$ (0.0, 0.0, 0.0), $vac3$ (0.0, 0.5, 0.0). The color code is the same as in 5.1. Interstitial atoms are depicted by red spheres while the vacancies are the highlighted green spheres. Two equivalent *vac1* positions are shown.

It turns out that the formation of ammonia via proton transfer between two neighboring NH_2^- groups ($2\,NH_2^- \longrightarrow NH_3 + NH^{2-}$) does not take place in bulk $LiNH_2$ in the absence of defects. In fact, ammonia is locally unstable with respect to a backtransfer of the proton to the neighboring NH_2^- group. In contrast, and in agreement with the proposal by David *et al.* [17], the NH_3/NH^{2-} pair is stabilized by the presence of a Li^+ interstitial

$$LiNH_2 + LiNH_2 \longrightarrow [LiLiNH_2]^+[\square NH_2]^- \longrightarrow Li_2NH + NH_3\,. \tag{5.5}$$

In the presence of a Li^+ interstitial only (*i.e.* in the absence of Li vacancies) the formation energy of ammonia is 1.11 eV while the activation energy for the process obtained from a NEB calculation is 1.15 eV (128-atoms supercell). By performing a molecular dynamics simulation at 400 K of $\sim$ 1 ps long, ammonia (the NH_3/NH^{2-} pair) is demonstrated to be locally stable in the presence of a Li interstitial. In the presence of both a Li interstitial and

a Li vacancy, the formation energy of ammonia is slightly higher, 1.23-1.39 eV, depending on the relative positions of the two defects. In particular, for the tightly bound Frenkel pair (nearest neighbor Li interstitial and vacancy) the formation energy of ammonia is 1.23 eV in the reaction proposed by David *et al.* [17] (cf. reaction 5.5).

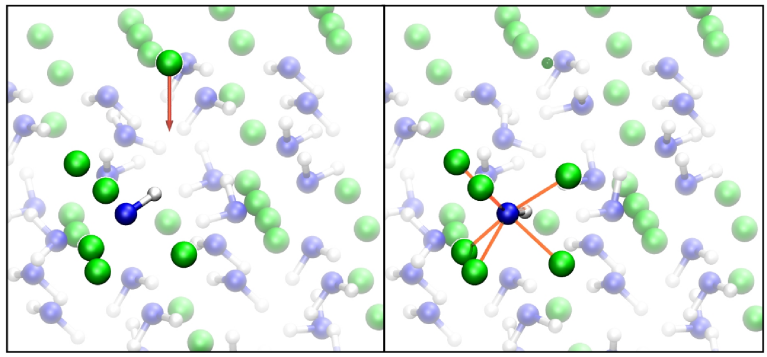

Figure 5.3: Formation of a Li Frenkel pair in the presence of a previously formed NH^{2-}/Li interstitial complex. The Li atoms nearest neighbors to the NH^{2-} group are highlighted. The color code is the same as in Fig. 5.1.

The activation energy for ammonia formation is sufficiently low to make the process viable at the temperatures and reaction speeds measured experimentally for $LiNH_2$ decomposition. However, the equilibrium concentration of the Frenkel pairs is rather small (10^{-8} per site for a formation energy of 1.42 eV at 500 K, cf. previous section), but ball-milling would increase the concentration of these defects with respect to the equilibrium values, especially when performed at a sufficiently low temperature at which defects are prevented from annealing [65]. Furthermore, once a NH^{2-} group is formed it can act as a nucleation center for the formation of other Frenkel pairs at a lower cost. Indeed in the presence of a previously formed NH^{2-} nearest neighbor to a Li interstitial, the formation energy of a second Frenkel pair is as low as 0.35 eV. The second Li interstitial increases the coordination of the NH^{2-} center whose environment becomes closer to that present in the Li_2NH phase (cf. 5.3). The formation energy of the second ammonia molecule (1.25 eV) is similar to that of the first. Fig. 5.4 shows the final configuration adopted after forming a second ammonia molecule near the second NH^{2-} center.

To sustain the accretion of an imide nucleus Li^+ and ammonia must diffuse. We thus computed the diffusivity of the two species as described hereafter.

Li diffusion in $LiNH_2$ We computed the activation energy for Li diffusion among the three interstitial sites by NEB calculations in the 128-atoms supercell. The resulting activation energies are 0.49 eV for the *int1* → *int2* jump (cf. Fig. 5.2) and 0.41 eV for *int1* ⟶ *int3* jump. The calculated activation energy for vacancy diffusion are instead 0.22 eV for the *vac1* ⟶ *vac2* jump (cf. Fig. 5.2) and 0.42 eV for the *vac1* ⟶ *vac3* jump. Sites 2 and 3 (for both the interstitial and the vacancy) are not nearest neighbors and are not connected by a single jump. For the less favored interstitial jump (*int1*

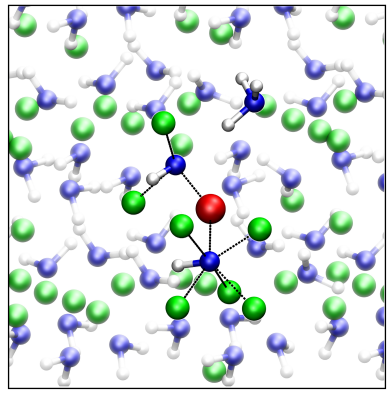

Figure 5.4: Final state after forming a second ammonia molecule near the nucleation center NH^{2-}.

$\longrightarrow$ *int2*), we computed the ZPE correction and the frequency prefactor $\nu^\star$ of the diffusion rate within harmonic transition state theory from phonons at the supercell Γ-point. The ZPE corrections slightly increases the activation energy from 0.49 eV to 0.51 eV, while $\nu^\star$ = 3.7 THz. This yields an estimated diffusion coefficient at 500 K of $D_{Li} \sim \frac{1}{6}\nu d^2 = 3.0 \cdot 10^{-9}$ cm^2/s (with the Li jump length of d=2.5 Å). However, we can envisage a preferential two dimensional diffusion mediated by vacancies (*vac1* $\longrightarrow$ *vac2* jumps) with a lower activation energy of 0.22 eV which would yield a vacancy diffusion coefficient of $D_V \sim \frac{1}{4}\nu d^2 = 3.6 \cdot 10^{-6}$ cm^2/s at 500 K by still – this assumes the same frequency prefactor, $\nu^\star$ = 3.7 THz.

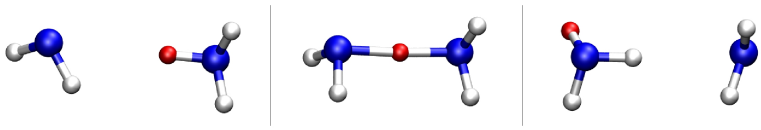

Figure 5.5: Snapshots of the initial, transition and final states of H^+ diffusion pathway in $LiNH_2$ as emerged from NEB calculations. The process corresponds to the diffusion of a NH_3 molecule. The color code is the same as in Fig. 5.1. The small red sphere indicates the jumping proton.

NH_3 diffusion in $LiNH_2$ An ammonia molecule in $LiNH_2$ can be seen as an additional proton bound to a NH_2^- group. Once formed, the ammonia molecule can easily diffuse in bulk $LiNH_2$ via a Grotthuss mechanism involving a H^+ jump between neighboring NH_2^- groups, similarly to the H_3O^+ diffusion pathway in water [120, 121]. Fig. 5.5 depicts the diffusion path for H^+ obtained from NEB calculations. The activation energy for the process is 0.45 eV or 0.36 eV in the presence of a neighboring Li interstitial. By including ZPE corrections the activation energy decreases from 0.45 eV to 0.34 eV. The frequency prefactor within the classical limit of h-TST is $\nu^\star$=1.2 THz which yields an estimated

diffusion coefficient at 500 K of $D_H \sim \frac{1}{6} \nu d^2 = 8.9 \cdot 10^{-8}$ cm^2/s (with an H^+ jump length of d=3.39 Å).

NH^{2-} diffusion in bulk $LiNH_2$ and formation of sub-stoichiometric phases The accretion of the Li_2NH nucleus by formation of additional Frenkel pairs and ammonia molecules, described above (with an overall reaction energy of 1.35+0.25 eV=1.6 eV) is in competition with the diffusion of the NH^{2-} group. The latter can migrate according to the reaction $NH^{2-} + NH_2^- \longrightarrow NH_2^- + NH^{2-}$ (cf. Fig. 5.6) which brings NH^{2-} away from the nucleus. This reaction has an activation energy of 0.65 eV in an otherwise perfect bulk $LiNH_2$ and of 0.75 eV in the neighborhood of a bound Frenkel pair (with a reaction energy of 0.1 eV to bring the NH^{2-} away from the Frenkel pair). The diffusion of NH^{2-} groups (H^+ vacancies) destroys the Li_2NH nucleus possibly leading to the formation of sub-stoichiometric phases identified in Ref. [17]. Mobile Li^+ ions to sustain the formation of the sub-stoichiometric phases are provided by the Li^+ excess generated at the $LiNH_2$ surface by ammonia desorption (see later). Once the NH^{2-} has diffused away from a Frenkel pair that had promoted the formation of the NH^{2-}/NH_3 pair, the original environment is reconstituted and a new ammonia molecule can be formed. Although the accretion of the Li_2NH nucleus in the bulk seems to be preempted by NH^{2-} diffusion, the situation is different at the surface as discussed in the next section.

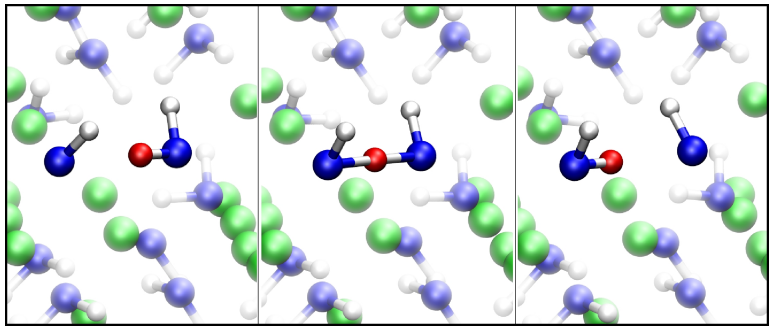

Figure 5.6: Mechanism of NH^{2-} diffusion in bulk $LiNH_2$. The geometries of the initial, transition and final states are shown. The color code is the same as in 5.5.

5.2 Formation of NH_3 at the $LiNH_2$ surface

So far we have analyzed only the elementary steps for the decomposition taking place in the bulk material. We have proposed a microscopic mechanism for the formation of the sub-stoichiometric phases that were experimentally revealed by David *et al.* [17]. However, ammonia could also form at the surface.

In order to study the microscopic processes involved in the formation of ammonia at the $LiNH_2$ surface, we considered the (001) surface of $LiNH_2$ with two different terminations: a Li-terminated surface and a NH_2-terminated surface. Both surfaces are charged so neutralization is achieved by removing half of the ions from the outermost layer (Li cations for Li-terminated surface or NH_2^- anions from the NH_2-terminated surface). A

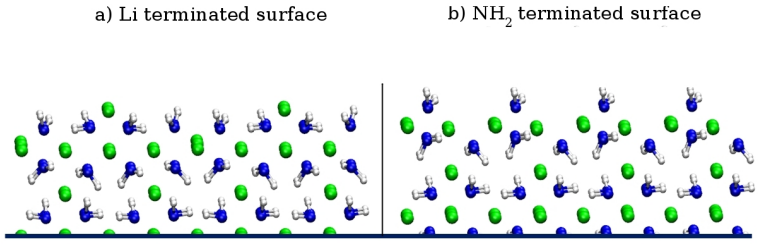

Figure 5.7: Side view of the slab models of the a) Li-terminated and b) NH_2-terminated (001) surface of $LiNH_2$ (the outermost layers are shown). The slab is made of $2 \times 2 \times 2$ replica of the $LiNH_2$ conventional unit cell (256 atoms). The vacuum is 10.33 Å in wide. The color code is the same as in 5.1.

Table 5.2: Energetic comparison of Frenkel pair and ammonia formation in the bulk and at the surface of $LiNH_2$.

	surface (eV)	bulk (eV)
Frenkel pair	0.11	0.97
ammonia	0.88	1.11

symmetric slab (256-atoms) with 17 atomic planes is considered for both terminations as depicted in Figs. 5.7a-b. The surface energy is obtained as the difference between the slab energy and the bulk energy obtained from the same slab supercell with the vacuum (10.33Å wide) filled with bulk $LiNH_2$. Convergence with respect to Brillouin Zone integration was checked with a 2×2 k-points mesh. The resulting surface energy is 0.31 J/m^2 for the Li-terminated surface and 0.83 J/m^2 for the NH_2-terminated surfaces which indicates that $LiNH_2$ (001) is terminated by Li. Surface reactions were then investigated by fixing the two bottommost atomic layers of the slab to their bulk positions. We verified that once it reaches the surface, ammonia (in the form of H^+ bound to a bulk NH_2^-) can desorb by overcoming a desorption energy barrier of 0.7 eV. We can now consider the formation of ammonia directly at the surface in the presence of a Frenkel pair. This was investigated at the (001) surface (Li-terminated) by moving a Li atom from the subsurface layer to the adjacent layer deeper in the bulk (cf. Fig. 5.8a). The formation energy of the bound Frenkel pair is now as low as 0.1 eV. As in the bulk, a Li interstitial promotes the formation of ammonia which now costs 0.88 eV with an activation energy of 1.05 eV. The ammonia molecule is formed by transferring a proton from a subsurface NH_2^- group to a surface NH_2^- group. An even lower overall formation energy of a Frenkel pair and ammonia (0.64 eV) is obtained by the same proton transfer as before but by forming a Li interstitial in the subsurface layer from an outermost surface Li atom (cf. Fig. 5.8b). This dramatic lowering of the energy of Frenkel pairs with respect to the bulk values (see Tab. 5.2) suggests that ammonia formation should start at the surface of $LiNH_2$.

Whether or not the formation of sub-stoichiometric phases in the bulk of $LiNH_2$, as discussed above, can be overridden by Li_2NH growth at the $LiNH_2$ surface, it depends on the diffusivity of Li^+ and H^+ in bulk Li_2NH and across the $LiNH_2$ /Li_2NH interface. This is an issue which will be addressed later.

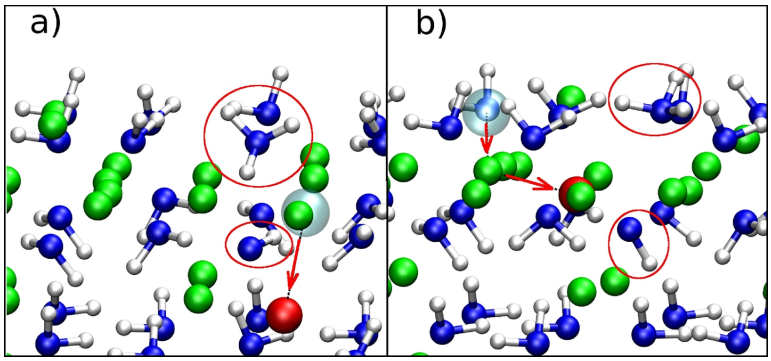

Figure 5.8: Mechanism of ammonia formation at the $LiNH_2$ (001) surface. Ammonia is formed by transferring a proton from a subsurface NH_2 group to a surface NH_2 group (indicated by circles). The resulting NH group is the nearest neighbor to a Li interstitial formed from a) a subsurface Li atom or from b) a surface Li atom. The movement of Li atoms leading to interstitial defects are indicated by arrows. The color code is the same as in Fig. 5.1. The initial position of the jumping Li atom is indicated by a semitransparent gray sphere, while the final position is indicated by a red sphere.

5.3 Diffusion of Li^+ and H^+ in Li_2NH and desorption of NH_3

A detailed discussion of the structure of Li_2NH and the nature of the order–disorder transition has been given in sections 4.1 and 4.3. In particular, as discussed before, our simulations display a very high Li^+ diffusivity in the high temperature phase of Li_2NH. As already reported in section 4.3 we calculated the Li self-diffusion coefficient at 400 and 500 K by means of mean square displacement which, using the Einstein relation $\langle x^2 \rangle \rightarrow 6tD_{\mathrm{Li}}$, gave us values of $D_{\mathrm{Li}}^{@\,400\,\mathrm{K}} = 1.44 \times 10^{-6} \mathrm{cm}^2/\mathrm{sec}$ and $D_{\mathrm{Li}}^{@\,500\,\mathrm{K}} = 3.26 \times 10^{-6} \mathrm{cm}^2/\mathrm{sec}$.

In what follows we also aim to model Li^+/H^+ transfer across the Li_2NH /$LiNH_2$ interface. It turns out that the activation energies for these processes are sufficiently low to sustain the decomposition reaction at the experimental transition temperature, but still too high to see these events occurring spontaneously during the short time span of an *ab initio* simulation, even at 500 K. Therefore, we had to resort to zero temperature NEB calculation to address several elementary processes, including H diffusion, also in the high temperature phase of Li_2NH as we did for $LiNH_2$.

As a good zero temperature model of the high temperature phase we adopted the *Imma* phase since it is a locally stable structure which embodies the local environment of vacancies and interstitials which, according to our previous discussion in section 4.3, survives in the high temperature $Fm\bar{3}m$ phase. We modeled the *Imma* phase with a

tetragonal 128-atoms supercell with lattice parameters fixed at the experimental values of a= 7.133 Å, b=10.087 Å and c= 7.133 Å [11]. The optimized atomic positions are essentially the same as the previous ab-initio results of Ref. [11] as can be seen from Tab. 4.1 on page 52.

H diffusion in Li_2NH We considered H^+ diffusion in Li_2NH by adding a proton to the 128-atoms supercell giving rise to a NH_2^- group which diffuses via a proton jump according to $NH_2^- + NH^{2-} \longrightarrow NH^{2-} + NH_2^-$. This reaction can take place between two groups that are nearest neighbors to the same vacancy or between two groups which are still nearest neighbors to each other but which point toward different Li vacancies. The activation energy of the proton transfer is 1.25 eV for the former process and 0.67 eV for the latter (cf. Fig. 5.9). In the absence of vacancy diffusion, both processes must take place to allow H^+ diffusion in Li_2NH . However, once Li vacancies start to diffuse at high temperatures, see section 4.3, the less energetically costly proton transfer process suffices to promote H^+ bulk diffusion or equivalently NH_2^- diffusion. We estimated ZPE corrections by calculating the Γ-point phonons at the initial and the transition states. These corrections reduce the activation energy from 0.67 eV to 0.57 eV. The frequency prefactor (cf. Eq. (5.3)) is $\nu^\star$ = 25 THz yielding an estimated diffusion coefficient of $D_H \sim \frac{1}{6}\nu d^2 = 8.5 \cdot 10^{-9}$ cm^2/s at 500 K where the H^+ jump length is d=3.27 Å.

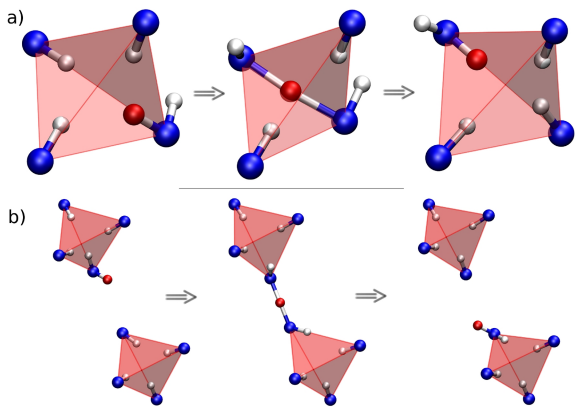

Figure 5.9: Initial, transition and final states for H^+ diffusion in Li_2NH among two NH groups that are a) nearest neighbors to the same Li vacancy (activation energy E_a=1.25 eV) or that are b) nearest neighbors to different vacancies although still nearest neighbors of each other (E_a=0.67 eV). The color code is the same as in Fig. 5.5.

Li_2NH surface and ammonia desorption Once two NH_2^- diffuse up to the surface they can react and form NH_3 which can then desorb from the surface. To study these processes we considered the (001) surface of Li_2NH with two types of terminations. Both surfaces are charged and neutralization is achieved by removing half of the ions from the outermost layer, Li^+ or NH^{2-} depending on the termination. A symmetric slab with 17 planes is considered both for Li-terminated and NH-terminated surfaces. The surface energy (256-atoms) is 0.56 J/m^2 for Li-terminated surface and 0.59 J/m^2 for the

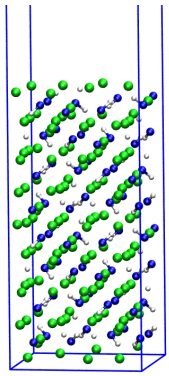

Figure 5.10: Side view of the slab model of the Li-terminated Li_2NH surface containing 256 atoms ($\sqrt{2}\times 1\times 2\sqrt{2}$ replica of the tetragonal cell, cf. section 4.1 (only the outermost layers are shown). The color code is the same as in 5.1.

NH-terminated surfaces. The surface energy is obtained as the difference between the slab energy and the bulk energy obtained from the same slab supercell but with the vacuum 10.33 Å wide filled with bulk Li_2NH . Hereafter we will consider only the more stable Li-terminated surface.

By diffusing in the bulk along the pathway discussed in previous sections, protons and thus NH_2^- groups can reach the Li_2NH surface and eventually react to give rise to an ammonia molecule which can then desorb. The formation of ammonia according to the reaction $2\,NH_2^- \longrightarrow NH_3 + NH^-$ is an endothermic process with an energetic cost of 0.3 eV which was computed as the energy difference between a configuration with a NH_3 at the surface and a configuration with two subsurface NH_2^- groups as far apart as possible in the 256-atoms slab. To compute the desorption energy of ammonia from the Li_2NH surface, we added two protons to the outermost NH layer of the slab with the bottommost two layers held fixed at their bulk positions. The charge was neutralized by a uniform background as is usual in periodic calculations. We then removed a neutral ammonia molecule from the surface and computed the desorption energy as the energy difference between the charged slab with and without the ammonia supplemented by the energy of a single ammonia molecule computed in the same supercell. The desorption energy turns out be as small as 0.08 eV.

5.4 H^+ / Li^+ transfer at the $LiNH_2$-Li_2NH interface

In a model in which decomposition is promoted at the $LiNH_2$ surface Li^+ and H^+ diffusion in Li_2NH are very important processes as they allow the system to evolve during the transformation. In the preceding section we presented our results on the diffusivity of the two charged species, Li^+ and H^+. However we still need one more step to complete this microscopic scenario. If the system is to decompose there must be a supply of H^+ to the Li_2NH and a supply of Li^+ to the $LiNH_2$ resulting in the release of NH_3 at the surface and the growth of Li_2NH. These processes take place at the $LiNH_2$ / Li_2NH interface by

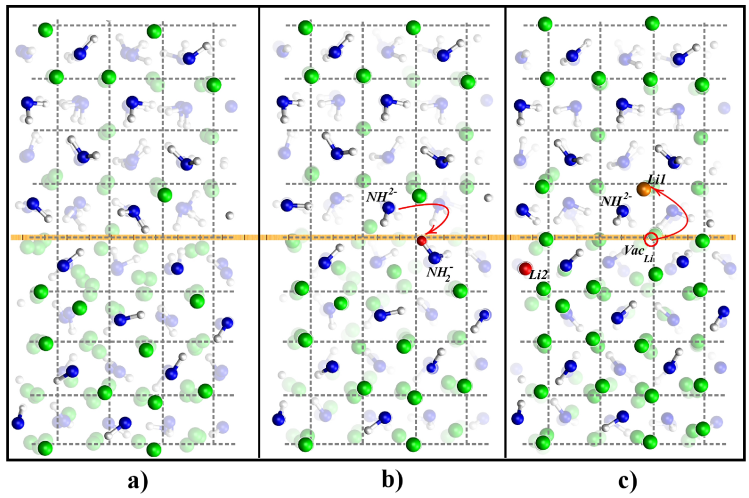

Figure 5.11: a) Side view of the slab model of the $LiNH_2/Li_2NH$ interface made of the two neutral slabs used previously for the $LiNH_2$ and Li_2NH surfaces (cf. Fig. 5.7a and Fig. 5.10). The supercell is made of 8 atomic layers of $LiNH_2$, 8 atomic layers of Li_2NH and two interface layers – 256 atoms in total. $LiNH_2$ is in the upper part. b) Path for H^+ transfer from $LiNH_2$ to Li_2NH. c) Path for Li^+ transfer from the interface to $LiNH_2$ (labeled Li1) in the presence of a Li interstitial (labeled Li2) in Li_2NH and a previously formed NH^{2-} in $LiNH_2$. In both cases b) and c) the systems are overall neutral. The color code is the same as in Fig. 5.5.

a mechanism of ion exchange.

Two neutral surfaces of $LiNH_2$ and Li_2NH (cf. Fig. 5.7a and Fig. 5.10) were merged by forming a neutral $LiNH_2$ /Li_2NH interface as shown in Fig. 5.11a. The interfacial lattice parameters were fixed to those obtained for the $LiNH_2$ (10.102 Å × 10.102 Å, cf. also Tab. 2.2) which are very close to the experimental ones of Li_2NH (10.087 Å × 10.087 Å, cf. also sections 4.1 and 4.3). Due to the similarities between the two structures (cf. sections 2.2 and 2.3), an epitaxial growth of Li_2NH on $LiNH_2$ is very likely.

The $LiNH_2/Li_2NH$ interfacial energy is 0.33 J/m^2 as computed from the difference between the interface slab and the bulk energies of amide and imide computed with a bulk supercell with the same number of atoms and the atomic layers of the interface model. We considered a proton transfer reaction across the interface by moving a proton from an NH_2^- group in $LiNH_2$ to an NH^{2-} group in Li_2NH in such a way that both lie close to the interface. The proton transfer costs 0.13 eV and requires that an activation energy of 0.61 eV be overcome (cf. Fig. 5.11b). The proton in Li_2NH can then diffuse away from the interface according to the mechanism discussed previously. On the other hand a Li interstitial can diffuse from bulk Li_2NH to the interface as discussed in section 4.3. We then considered the possibility that an interstitial Li in Li_2NH may be transferred across the interface in the neighborhood of a previously formed NH^{2-} group in $LiNH_2$. This is achieved by moving a Li^+ ion from the interface to a bulk position in $LiNH_2$ in the presence of both a Li^+ interstitial in Li_2NH and a NH^{2-} group in $LiNH_2$ (cf. Fig. 5.11c).

Table 5.3: Summary of reaction and activation energies of elementary processes in $LiNH_2$. Self-diffusion coefficients ($10^{-9}cm^2/s$) at 500 K are given in parenthesis.

	energy [eV]	activation energy [eV]
bound Frenkel pair (bulk)	0.97	1.15
unbound Frenkel pair (bulk)	1.42	–
NH_3 formation (bulk)	1.11	1.15
second Frenkel pair (bulk)	0.35	–
second NH_3 (bulk)	1.25	–
NH^{2-} (H^+ vacancy) diffusion	–	0.65
NH_3 (H^+) diffusion	–	0.34 (89)
Li diffusion	–	0.51 (3)
Frenkel pair (surface)	0.1	–
NH_3 formation (surface)	0.88	1.05
NH_3 desorption	0.7	–

The reaction energy for this process is 0.3 eV and the activation energy is 0.5 eV. In the absence of a previously formed NH^{2-} group in $LiNH_2$, the transfer of a Li interstitial from Li_2NH to $LiNH_2$ can be as expensive as 0.9 eV. This reaction energy corresponds to the least favorable situation for Li transfer.

5.5 A microscopic scenario for $LiNH_2$ / Li_2NH transformation

The reaction and activation energies of the elementary processes in $LiNH_2$, Li_2NH and at the $LiNH_2$/Li_2NH interfaces presented in the previous Sections are summarized in Tabs. 5.3 and 5.4. As discussed in section 5.1, NH_3 does not form within bulk $LiNH_2$ in the absence of defects. As proposed in Ref. [17], Li Frenkel pairs promote the formation of ammonia ($2\,NH_2^- \longrightarrow NH_3 + NH^{2-}$) with a reasonable activation energy (1.15-1.23 eV). Although, Frenkel pairs are few at equilibrium (10^{-8} per site at 500 K) they can act as nucleation centers for the growth of Li_2NH. In fact, a newly formed NH^{2-} species drastically lowers the formation energy of a second Frenkel pair (down to 0.35 eV) and thus of a new ammonia molecule. Ammonia can easily diffuse away ($D_{H^+} = 8.9 \cdot 10^{-8}$ cm^2/sec at 500 K) and reach the surface and desorb with an energetic cost of 0.7 eV. The excess of Li^+ formed at the surface upon ammonia desorption can also diffuse inside sufficiently rapidly (D_{Li^+}=$3 \cdot 10^{-9}$ cm^2/sec at 500 K). The accretion of Li_2NH nuclei is in competition with the diffusion of NH^{2-} species. This process has an activation energy of only 0.65 eV and serves to deplete the nuclei leading to the formation of the sub-stoichiometric phases identified in the X-ray diffraction experiments of Ref. [17].

The formation of Frenkel pairs and then of ammonia is much less expensive at the surface than in bulk $LiNH_2$ at an overall energy cost of 1.15 eV. It is therefore conceivable that the decomposition starts at the surface. In this scenario, ball milling would enhance

Table 5.4: Summary of reaction and activation energies of elementary processes in Li_2NH and at the $LiNH_2/Li_2NH$ interface. Self-diffusion coefficients ($10^{-8}cm^2/s$) at 500 K are given in parenthesis.

	energy [eV]	activation energy [eV]
Li diffusion	–	0.11 (326)
H^+ diffusion	–	0.57 (0.85)
$2\,NH_2^- \rightarrow NH_3 + NH^{2-}$	0.30	–
NH_3 desorption	0.08	–
H^+ transfer at $LiNH_2/Li_2NH$ interface	0.13	0.61
Li^+ transfer at $LiNH_2/Li_2NH$ interface	0.30	0.50

the decomposition rate by increasing the surface-to-volume ratio of the crystallites. In the early stage of the $2\,LiNH_2 \longrightarrow Li_2NH + NH_3$ transformation, the overall activation energy would be of the order of 1.8 eV which is the sum of the formation of a Frenkel pair, the formation of an ammonia at the surface and ammonia desorption energy. This activation energy is within the range of experimentally reported values of 2.54-1.44 eV [38, 33]. Once a thin shell of Li_2NH is formed around a $LiNH_2$ core, the reaction can proceed via the inward movement of the $Li_2NH/LiNH_2$ interface. This may happen by mass transport across the interface in the form of Li^+ transfer from Li_2NH to $LiNH_2$ and H^+ transfer from $LiNH_2$ to Li_2NH which both have a relatively low activation energy (0.50 eV and 0.60 eV, respectively). H^+ transfer across the interface gives rise to NH_2^- groups in Li_2NH which can diffuse (D_{H^+}=8.5 $\cdot$ 10^{-9} cm^2/sec at T=500 K), reach the surface and react to form ammonia ($2\,NH_2^- \rightarrow NH_3 + NH^-$, ΔE= 0.3 eV). This can then desorb easily at the low cost of 0.08 eV. The excess of Li^+ produced at the Li_2NH surface by ammonia desorption can diffuse very rapidly (D_{Li^+}=3.26 $\cdot$ 10^{-6} cm^2/sec at T=500 K) through Li_2NH and reach the $Li_2NH/LiNH_2$ interface. Li^+/H^+ transfer across the interface gives rise to an inward movement of the interface. This scenario corresponds to the core-shrinking model proposed in Ref. [18] which is supported by our results provided that the surface-to-volume ratio is sufficiently large for the fast surface reaction to override the slower formation of sub-stoichiometric phases in the bulk as discussed above. Since the molar volumes of $LiNH_2$ and Li_2NH are very similar and the $2\,LiNH_2 \longrightarrow Li_2NH + NH_3$ reaction involves two moles of $LiNH_2$ and one mole of Li_2NH, the volumes of the grains must shrink by a factor two during the transformation. This may occur in the core shrinking model via a simultaneous inward movement of both the $LiNH_2/Li_2NH$ interface and the outer Li_2NH surface or via generation of a porous products. This decomposition mechanism would imply a refinement of the grains upon cycling unless the grains grow during hydrogenation. Whether or not this model is consistent with the experimental observation of a stable grain size over cycling in ball-milled sample [18], remains to be seen as this requires a description of the hydrogenation step as well. According to our *ab initio* data, in the core-shrinking scenario the rate limiting step consists of the diffusion

of H^+ (NH_2^-) in the Li_2NH shell in agreement with the kinetic analysis of the late stages of decomposition in Ref. [18] which led to the conclusion that the decomposition is limited by mass transport within Li_2NH.

6

Li_2NH re-hydrogenation mechanism

As discussed in section 2.1 the hydrogenation of Li_3N was first investigated by Dafer and Miklauz [29] as early as in 1912. However, only recently P. Chen *et al.* [9] identified the full hydrogenation process and the nature of intermediates as

$$Li_3N + 2H_2 \rightleftharpoons Li_2NH + LiH + H_2 \rightleftharpoons LiNH_2 + 2LiH \tag{6.1}$$

with an overall amount of ~ 10 wt % of H_2 absorbed or desorbed.

In Chapter 5 we discussed the dehydrogenation reaction and presented our results on the microscopic mechanism of transformation. Here we focus on the reverse process: the absorption of hydrogen by Li_2NH according to

$$Li_2NH + H_2 \longrightarrow LiNH_2 + LiH\,. \tag{6.2}$$

From a detailed analysis of high-resolution synchrotron X-ray diffraction data for process 6.2 David *et al.* [17] identified the formation of sub-stoichiometric phases. According to them the key factor is the formation of Li Frenkel pairs (see eq. (6.3)) of both amide and imide in the dehydrogenation and hydrogenation processes. In the case of hydrogenation interstitial Li^+ ions migrate towards the Li_2NH surface. The incoming H_2 molecule can then react with a Li^+ interstitial according to eq. (6.4) and dissociate heterolitically

$$Li_2NH \longrightarrow [\square LiNH]^- + Li^+ \tag{6.3}$$

$$Li^+ + H_2 \longrightarrow LiH + H^+\,. \tag{6.4}$$

The presence of a negatively charged site $[\square LiNH]^-$ represents an attractive center for the proton which will turn the NH^{2-} group into NH_2^- as

$$H^+ + [\square LiNH]^- \longrightarrow [\square LiNH_2]\,. \tag{6.5}$$

Fast ionic diffusion in bulk Li_2NH can then keep supplying the surface with Li^+ ions so as to sustain the decomposition of the adsorbing H_2 molecules.

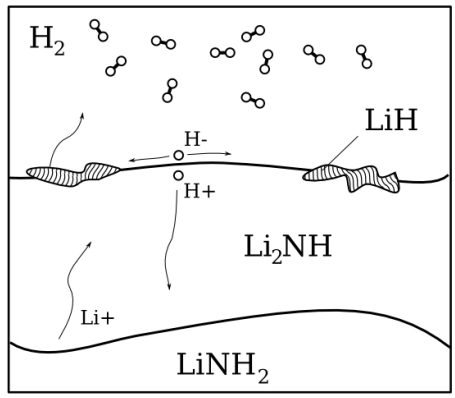

Figure 6.1: Schematic representation of a possible scenario for the microscopic mechanism of Li_2NH hydrogenation (see the text for a more detailed explanation).

6.1 Microscopic scenario for hydrogenation

Analogously to what discussed in Chapter 5 for the dehydrogenation mechanism, although the presence of Frenkel pairs may trigger the transformation, several others elementary steps are involved in the overall hydrogenation reaction. We could conceive different growth models for the amide amongst which we could select the most favorable on the basis of the calculated rate of the elementary steps. A possible reaction pathways is described in Fig. 6.1. In this pathway, H_2 molecules are adsorbed at the Li_2NH surface, where they dissociate heterolitically forming LiH molecules and H^+. These protons can then diffuse into the bulk, in the form of NH_2^- and give rise either to sub-stoichiometric phases or to $LiNH_2$. On the other hand, the accretion of LiH needs the diffusion of Li^+ from the H^+ reach region.

To check the validity of this scenario we must compute the activation energies for several elementary steps

1. heterolitic dissociation of the H_2 molecule at the surface and formation of LiH complexes and NH_2^- groups
2. diffusion of LiH complexes
3. diffusion of NH_2^- groups

The last process (H^+ diffusion in Li_2NH) has already been discussed in Chapter 5 . Hereafter we will present our results on process 1. and 2..

6.1.1 H_2 adsorption and splitting at the Li_2NH surface

We chose the (001) surface of Li_2NH (cf. also section 5.3 at page 86) which was modelled with a $\sqrt{2} \times 1 \times 2\sqrt{2}$ $Imma$ 256-atom supercell with a vacuum 10.087 Å wide and a thickness of seventeen atomic layers along the z direction. The Li-terminated

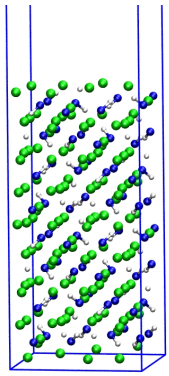

Figure 6.2: Side view of the (001) surface of Li_2NH with optimized atomic positions. The supercell used contains $\sqrt{2} \times 1 \times 3\sqrt{2}$ HH unit cell with a vacuum that is 10.087 Å wide.

surface has only a half-Li^+ coverage to make the surface neutral. To mimic a semi-infinite bulk system, three atomic layers at the bottom were fixed as their ideal crystal positions.

After geometry optimization the atoms in the topmost layer move as much as 1 Å with respect to ideal termination of the bulk. In Fig. 6.2 we report a side view of the optimized (001) surface of Li_2NH with optimized atomic positions. In particular, the outermost Li^+ layer moves inwards by reducing the interplanar space between it and the NH^{2-} plane by ~ 0.5 Å. Secondly, the NH^{2-} layer is rumpled by ~ 0.6 Å due to the presence of Li^+ vacancies on the top layer.

We considered two adsorption sites for H_2. The first is a Li^+ vacancy at the surface coming either from stoichiometry vacancies or from a Li^+ removed to enforce surface neutrality (site A, see Fig. 6.3(a)). The second site corresponds to the octahedral site of bulk Li_2NH (site B, see Figs. 6.3(b)).

The adsorption energies meanwhile are -0.02 eV and -0.05 eV for the first and the second sites respectively. At site A, geometry optimization brings the H_2 molecule far away from the neighboring Li^+ (~ 3.2 Å) and from the neighboring NH^{2-} group (~ 4 Å). In contrast at site B the distance between H_2 and the underlying NH^{2-} group is sufficiently short (~ 2.9 Å) for a heterolitic dissociation of H_2 to take place.

In Fig. 6.4 we report the initial transition and final states of a NEB optimization of the $H_2 + NH^{2-} \longrightarrow H^- + NH_2^-$ reaction. The reaction is exothermic with an energy gain of 0.2 eV and an activation barrier of 0.5 eV. The final state consists of a stable NH_2^- group and an H^- ion at the surface (cf. Fig. 6.4). The distances between the two Li atoms and H^- ion are both equal to 1.85 Å.

So far we have only analyzed the elementary step for H_2 splitting at the surface. The problem now is to figure out how the process can continue and how the products, LiH and $LiNH_2$, can grow. From an energetic point of view it seems that H_2 splitting at the surface is viable but the two newly formed defects must separate and diffuse.

In order to study H^- diffusion at the (001) Li_2NH surface we had to enlarge our surface cell by duplicating it along the x direction. Furthermore, to make the calculation

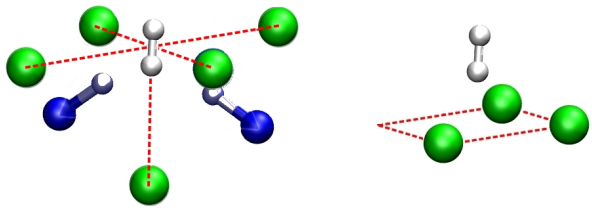

(a) site A (b) site B

Figure 6.3: Vacant sites of Li_2NH which can host an H_2 molecule. In Wyckoff notation for the $Fd\bar{3}m$ symmetry: (a) H_2 at a Li^+ vacancy site, site A, (b) and H_2 at the octahedral site of bulk Li_2NH, site B.

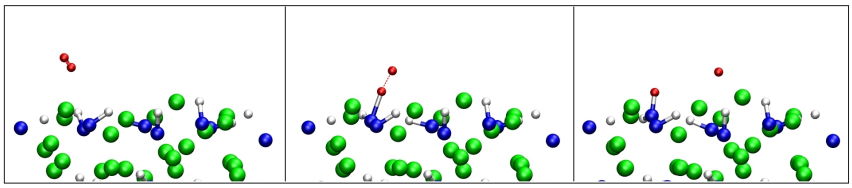

Figure 6.4: The (a) initial, (b) transition and (c) final states of the H_2 splitting process at the surface. The hydrogen atoms of the H_2 molecule that is splitting are depicted with red spheres.

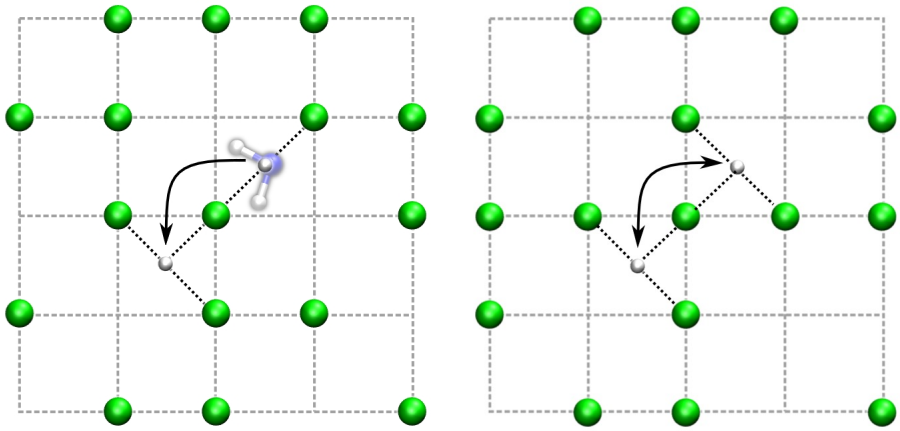

(a) (b)

Figure 6.5: Outermost plane of the Li_2NH (001) surface with a chemisorbed H_2 molecule forming an adsorbed H^- and an underlying NH_2^- group (shaded in pannel (a)). H^- jumps from a 2-fold to a 3-fold coordinated site. (b) H^- jumping among equivalent 3-fold coordinated sites.

affordable we had to reduce the thickness. The resulting supercell contained a 256-atom and consisted of $2\sqrt{2} \times 1 \times 2\sqrt{2}$ HH cells – nine atomic layers bottommost three layers fixed with the atoms on the bulk positions.

To diffuse H^- can perform a single jump from the octahedral site, where it forms, to another octahedral site (see Fig. 6.5). In the elementary jump considered, the coordination of H^- increases from two to three Li^+'s which result in an energy gain of 0.5 eV (cf. Fig. 6.5(a)). The calculations of these two processes are in progress. On the other hand, NH_2^- cen diffuse in bulk Li_2NH to form either sub-stoichiometric phases or $LiNH_2$ as discussed in chapter 5.

6.1.2 H_2 absorption and splitting in the Li_2NH bulk

The microscopic scenario discussed so far implies that an H_2 molecule splits at the Li_2NH surface. We have investigated whether or not the same process discussed above might take place inside the bulk.

The Li_2NH bulk system has been modeled with a 128-atom supercell ($\sqrt{2} \times 1 \times \sqrt{2}$ HH cell) with an $Imma$ symmetry as it is a good representation of the high temperature phase of Li_2NH (see chapters 4 and 5).

We considered three inequivalent sites in which Li_2NH could host an H_2 molecule: 8*c*, 16*c* and 16*d* (cf. Fig. 6.6). These three different sites offer to the molecule not only a symmetrically inequivalent position but also different chemical environments. The configuration in which H_2 is placed in the 8*b* site, Li^+ vacancy position, is unstable. Upon geometry optimization, the H_2 molecule spontaneously leaves the site, moving towards

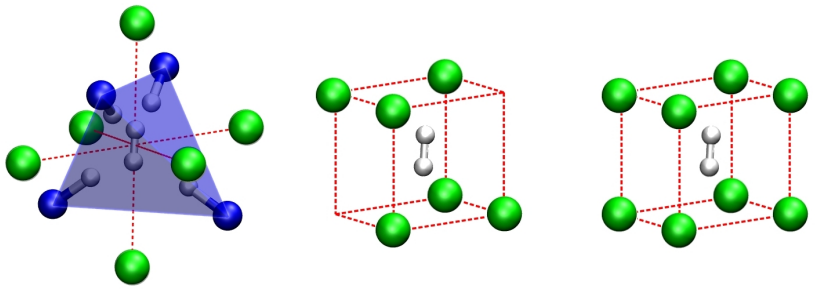

Figure 6.6: Vacant sites where Li_2NH could host a H_2 molecule. Using the Wyckoff notation for the $Fd\bar{3}m$ symmetry: (a) H_2 is placed at the 8*b* site, (b) and (c) H_2 is placed at the octahedral interstitial site 16*d* and 16*c* respectively.

an octahedral site (either 16*c* or 16*d*). The instability of this configuration for the H_2 molecule is most likely due to the strong Coulomb repulsion between H_2 and the four $H^{\delta+}$ of the NH groups that point towards the vacancy and/or due to the very small space.

On the other hand, the higher coordination in the 16*c* sites helps the heterolitic split of H_2 and the formation of NH_2^- and LiH species according to the following steps

$$NH^{2-} + H_2 + Li^+ \longrightarrow NH_2^- + H^- + Li^+ \tag{6.6}$$

$$NH_2^- + H^- + Li^+ \longrightarrow NH_2^- + LiH\,. \tag{6.7}$$

The heterolitic splitting is an exothermic process with an energy gain of 0.57 eV and an energy barrier of 0.02 eV.

In order to move the H^- ion away from the octahedral site near the NH_2^- group and allow the formation of LiH (eq. (6.7)) we performed a metadynamics simulation that used the distance between H^+ and H^- as a collective variable. This simulation was merely used to uncover the reaction path that drives H^- to form LiH. During this ~ 2 ps long metadynamics simulation, we observed the H^- ion moving away from the original position near the NH_2^- defect to a new octahedral site. The reaction path has been used as the initial path for a NEB optimization. As shown in Fig. 6.7(c) (and highlighted in Fig. 6.7(d)) the Li_2NH lattice undergoes a big distortion in the vicinity of the new position of H^-. In fact, 6 out of the 8 Li atoms belonging to the cubic structure of the Li-tetrahedral sites coordinate the H^- ion in a octahedral way as in the perfect fcc crystal structure of the solid LiH (see Figs. 6.7(c) and 6.7(d)). The average H–Li distance in these new defects is (1.89±0.09) Å which is much longer than H–Li distance in LiH bulk (1.021 Å).

The energetic cost for moving H^- from the intermediate to the final state is ΔE=0.57 eV, exactly the same amount of energy gained during the splitting process, while the energy barrier for the splitting is E_a=1.29 eV. The insertion of a H_2 molecule into the Li_2NH bulk costs 1.1 eV for insertion at the 16*c* site and 0.64 eV for insertion at the 16*d* site.

Although the H_2 splitting and formation of a LiH (strongly expanded) molecules

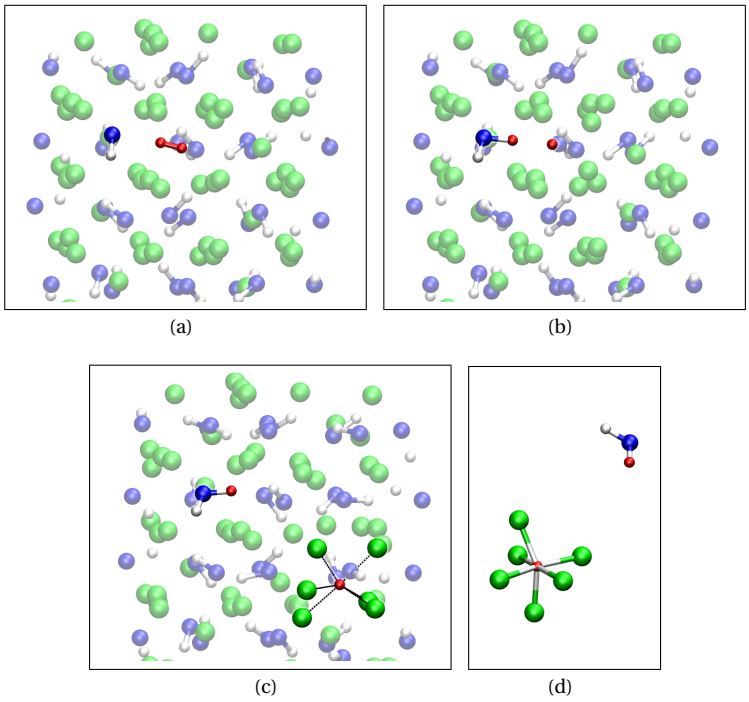

Figure 6.7: (a) Initial, (b) intermediate and (c) final states for the splitting of an H_2 in the Li_2NH bulk. In (d) the NH_2 group and the distorted octahedral coordination of H^-, as in LiH compound, are highlighted and shown in a different side view. The H atoms of the H_2 molecule before and after the splitting are represented by red spheres.

Table 6.1: Summary of reaction and activation energies for the elementary processes involved in the Li_2NH re-hydrogenation both at the surface and in the bulk (results previously presented regarding Li^+ and H^+ diffusivity in Li_2NH bulk are reported again here for completeness).

	energy [eV]	activation energy [eV]
(001) Surface		
Adsorption @ site A	-0.02	–
Adsorption @ site B	-0.05	–
$NH^{2-} + H_2 \longrightarrow NH_2^- + H^-$	-0.20	0.5
H^-, NH_2^- separation	-0.50	0.55
H^- diffusion (@ surf.)	0	–
Bulk		
H_2 insertion in 16*d* site	+0.64	–
H_2 insertion in 16*c* site	+1.1	–
$NH^{2-} + H_2 \longrightarrow NH_2^- + H^-$	-0.57	0.02
H^- diffusion	+0.57	1.29
Li^+ diffusion	–	0.11
H^+ diffusion	–	0.70

seem viable in the bulk, the energy required to insert the H_2 molecule turns to be higher than the activation energy of the H_2 splitting at the surface.

The study of the rehydrogenation mechanism is still in progress. In fact, other elementary processes might come into play as the hydrogenation proceeds.

The data obtained so far indicates that the hydrogenation process starts at the Li_2NH surface and that the accretion of $LiNH_2$ and LiH is assisted by diffusion of LiH and NH_2 species at the surface and in the bulk of Li_2NH. In fact, this is the starting point for the whole process. Clearly, splitting of H_2 molecules at the Li_2NH surface can continue only if a free surface of Li_2NH is available. In contrast, if the product phase, $LiNH_2$, grows around Li_2NH the hydrogenation can continue only via the splitting of H_2 molecules at the surface of $LiNH_2$.

To continue this work we will study the splitting process of H_2 molecules at the $LiNH_2$ surface and in the bulk and the diffusion of H^- at the $LiNH_2$ surface. This will finally provide us with a full microscopic description of the hydrogenation process.

Conclusion

In this thesis we have presented our results on the $LiNH_2/Li_2NH$ system. We have investigated the low temperature crystal structure of Li_2NH which, in spite of great interest as a potential hydrogen storage material, was still matter of debate. We have presented a new LT crystal structure which solves the inconsistencies presented in previous proposals. The microscopic mechanism for the $LiNH_2/Li_2NH$ transformation has been investigated and the apparent contradiction between two different experimental works that have appeared recently in literature has been resolved.

From our molecular dynamics simulation at 300 K we have observed that an ideal anti-fluorite structure of Li_2NH is unstable with respect to spontaneous formation of Li Frenkel pairs. Furthermore, as soon as a Li vacancy is formed NH groups reorientate towards it. In actuality, a structure in which an empty tetrahedral site (Li vacancy) is coordinated by four NH groups is very stable (4NH-vacancy complexes). However, we have observed that the corresponding number of interstitial Li atoms diffuse very fast by an exchange mechanism with an barrier as low as 0.11 eV. This low barrier allows for rapid diffusion below the structural transition temperature which, as suggested, corresponds to a superionic transition. On the other hand, we have observed from our dynamical trajectory aggregation of Li interstitials into Li_4-clusters around the new Li vacancies which also appears to be stable. Thus, we have proposed a new LT crystal structure of Li_2NH in which all the Li interstitial atoms are arranged in tetrahedral clusters. The possibility to have many almost-degenerate configurations of these clusters suggests a static disorder with a fractional occupation of the Li site in agreement with that found with Rietveld analysis. The average atomic positions are in excellent agreement with diffraction data and solve all the inconsistencies in previous proposals.

Molecular dynamics simulations below and above the transition temperature have allowed us to give an explanation for the transition mechanism from the LT to the HT phase of Li_2NH. Li_4-clusters have been considered as a phenomenological order

parameter for the phase transition. At HT all the structures, 4NH-vacancy complexes and Li_4-clusters, are broken. However, as soon as the temperature is lowered to 500 and 400 K the majority of the NH groups reorientate to reform the 4NH-vacancy complexes while these remaining other rotate very rapidly. At these lower temperature the Li_4-clusters survive but in a dynamical way with a lifetime that depends on the temperature. Above the transition temperature we have observed rapid diffusion of Li interstitials atoms together with a slower diffusion of the vacancies. The picture is that a single frame of the HT phase can be described with a $Imma$ space group. Averaging over space and time we recover the anti-fluorite structure, $Fm\bar{3}m$ space group, identified in experiment.

The reaction rates and the diffusivities of the various species in $LiNH_2$ and Li_2NH collected from our *ab initio* simulations provided a microscopic scenario for the solid state reaction $2\,LiNH_2 \longrightarrow Li_2NH + NH_3$. According to our *ab initio* calculations, the transformation path depends on the surface-to-volume ratio of the $LiNH_2$ crystallites. In short, it turns out that ammonia formation is promoted by the presence of Li Frenkel pairs as suggested in Ref. [17]. However, ammonia formation is more likely to occur at the surface than in the bulk. Hence, one might thus expect that for small $LiNH_2$ particles the transformation is controlled by the surface. In this case, during the early stage of decomposition, the rate limiting step is the formation of ammonia assisted by Frenkel pairs at the $LiNH_2$ surface. Once a shell of Li_2NH is formed outside a Li_2NH core, the rate-limiting step becomes the H^+ diffusion in the Li_2NH product. Transfer of H^+/Li^+ across the $LiNH_2/Li_2NH$ moving interface and the formation of NH_3 from NH_2^- groups in Li_2NH are not rate limiting. Our results support the kinetic model proposed in Ref. [18] in which a shell of Li_2NH grows from the surface at the expense of a shrinking core of $LiNH_2$. On the other hand, for larger crystallites with smaller surface-to-volume ratios, ammonia formation would also take place in the bulk in the presence of Frenkel pairs at a higher pace due to the larger number of defects. However, formation of Li_2NH in the bulk of $LiNH_2$ via accretion of Li_2NH nuclei is preempted by diffusion of the NH^{2-} species which can eventually lead to the formation of the sub-stoichiometric phases identified in Ref. [17]. We believe that the size dependency of the decomposition pathways that we have uncovered might not be restricted to Li amide but could be shared with other complex hydrides.

Appendices

A

Li_4-cluster and 4NH-vacancy complexes

Everyone agrees that the N atoms are fixed on fcc sites. In fact they show a perfect fcc lattice both at low and high temperatures. Also in our study we focused mainly on the Li lattice looking in particular at the peculiar structures directly and indirectly connected with Li motion. Clearly, the phase transition involves Li motion and thus any phenomenological order parameter should be connected to a specific cooperative rearrangement of local structure within the Li lattice. As already discussed Li_4-clusters and 4NH-vacancy structures make up the statically-disordered, LT, $Fd\bar{3}m$ structure discussed herein and suggested in Ref. [11]. It therefore seems reasonable to use an order parameter that detects the presence of these features to describe the phase transition and high temperature phase of Li_2NH.

As previously discussed in our simulations we modeled the system with a 192-atom supercell. Here, in order to accommodate all the NH groups tetrahedrally coordinated around a Li vacant site, 12 constitutional vacancies are present (at T=0) forming a ordered diamond-like sublattice (*i.e.* the Li2, 8*b* sites are empty). The 12 Li atoms (interstitial Li atoms) together with other four more Li atoms form a 4 Li tetrahedral cluster structure. In fact, four Li atoms placed at the 8*a* sites move away from the original site along the ⟨111⟩ direction leaving a new vacant site in the Li cubic sublattice (see section 4.1). While 4NH-vacancies form a perfect diamond sublattice (8*b* sites of $Fd\bar{3}m$ structure) the Li-cluster vacancies do not. In fact, although 8*a* of sites form a perfect diamond lattice in the $Fd\bar{3}m$ structure, they can not host a Li-cluster because of the stoichiometry. Only 4 of the 12 8*a* sites in this 192-atom Li_2NH structure can be occupied by a Li-cluster. In this picture Li_2NH presents a static disorder connected with the many possibilities distributing the Li-clusters. Therefore, directly connected with the Li atom sublattice our structure shows 16 constitutional vacancies 12 of which are 4NH-coordinated while the other 4 are 4Li-coordinated.

The spatial distribution of the Li_4 and 4NH vacancies are very similar. Both sit on a diamond lattice, however in the case of Li_4-cluster this lattice is only partially occupied (cf. Figs. A.1(b) and A.1(c)). Furthermore, from a dynamical point of view, these two superstructures are correlated because the 8*a* and 8*b* sites are the only sites in the $Fd\bar{3}m$

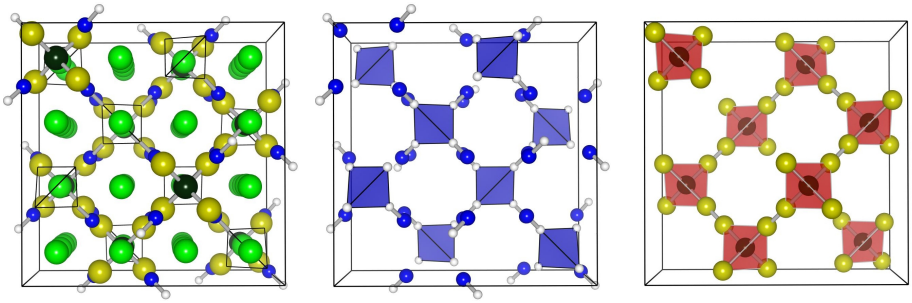

(a) (b) (c)

Figure A.1: (a) $Fd\bar{3}m$ crystal structure for Li_2NH. In the picture the atoms are represented: ● Blue = N and ○ White = H. Furthermore, Li atoms inequivalent by symmetry are represented in a different color: ● (Green) = Li1 lithium atoms placed at $48f$ sites, ● (Dark Green) = Li2 lithium atoms placed at $8a$ sites, ● (Light Green) = Li3 lithium atoms placed at $32e$ sites. (b) 4NH-vacancy complexes are highlighted by blue polyhedra. The vacant $8b$ sites form a diamond sublattice. (c) Li_4-cluster complexes are highlighted by red polyhedra. The $8a$ sites, where Li clusters are placed, form a diamond sublattice.

structure that show a tetrahedral coordination with the N atoms. Each of them could host a 4NH tetrahedron or a 4Li tetrahedron (with a relative "perpendicular" orientation), the channel of connection being the Li2, $8a$, and Li1, $48f$, occupied sites of the whole Li sublattice.

We hypothesize that by looking at these features of the whole structure we would be able to describe the dynamical-structural proprieties of the system and its behavior during the transformation.

Since N atoms perform only small vibrations around a perfect fcc site we chose the N sublattice as reference system for a structural analysis. To distinguish a tetrahedral site of the anti-fluorite structure and to assign it an available space we can image the primitive fcc anti-fluorite structure divided up into 8 cubes each of which contains a tetrahedral site (see Fig. A.2(a)). In a dynamical simulation N atoms move and the N framework is slightly distorted by the low frequencies. Now the distorted-cube vertices are defined by the 4 N atom positions and the 4 new points calculated as an arithmetical average of the nearest neighbors N atom positions that coordinate octahedrally that point (see Fig. A.2(b)). These two definitions of the tetrahedral fcc interstitial volume correspond to a division of the whole volume into Voronoi polyhedra of a cubic lattice of tetrahedral sites which are defined by N atom instantaneous positions. In addition, another volume definition has been used. Here the tetrahedral interstitial volume is a sphere with a center calculated as the average of the nearest N atom positions that coordinate tetrahedrally to the point (see Fig. A.2(c)). This last choice is in order to more accurately describe the Li-clusters we will explain later.

With these definitions for the volume of a tetrahedral fcc interstitial site we can clearly distinguish a 4NH-vacancy (4 H atoms and no Li inside the volume), a Li-cluster (4 Li atoms) and an octahedral site, Li4, occupied (only 1 Li atom). Of course, during the

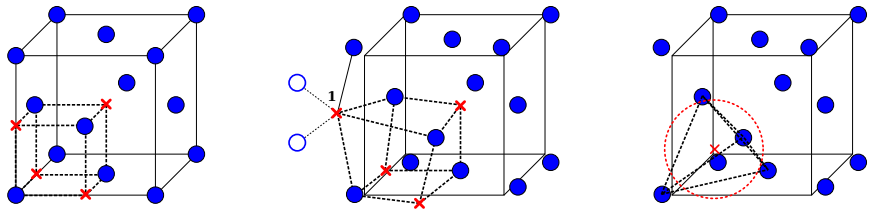

(a) T=0 (b) T≠0 (c) T≠0

Figure A.2: Definition of the volume of a tetrahedral center. (a) At zero temperature, T=0, the volume is a perfect cube (edge equal to $a/2$). (b) At T≠0 the cube is distorted with vertices represented by the 4 N positions and the other calculated as the arithmetical average of the 6 N positions octahedrically coordinated (as highlighted vertex for 1). (c) At T≠0 the volume is defined as a sphere with center in the arithmetical average of the positions of N atom tetrahedral-like coordinated. Here blue spheres are N atoms, and dashed lines indicate the tetrahedral volume.

dynamical simulation we can also have many other intermediate situations.

B

Charged defects: energetic corrections

In *ab initio* simulations, defects in solid are treated as isolated inside a supercell with periodic boundary conditions (PBC). Unfortunately, this approach introduces artificial interactions between charged defects which represents a large source of errors for evaluating the energetics of defects. Generally, the computational approach is to put the defect inside a supercell with PBC and embed it with a uniform neutralizing background. This approach fails because of the long-range nature of the electrostatic interactions. In fact, the charged defect, nonphysically, interacts with its periodic images giving rise to a very slow convergence for the defect energy with respect to the cell size.

The spurious term in the energetics can be approximately evaluated if one assumes that the charged defect with its images forms a perfect ionic lattice. Therefore the unphysical interaction energy can be estimated from the Madelung energy of an array of charged point in a uniform neutralizing background [122]

$$E_{\text{Madelung}} = -\frac{\alpha q^2}{2\varepsilon L} \tag{B.1}$$

where α is the lattice-geometry dependent Madelung constant, q is the defect charge, ε the macroscopic dielectric constant and L is the linear dimension of the cell.

This represents only an upper bound value for energy corrections when defects are studied. More accurate evaluations have been suggested where the quadrupole momenta term, qQL^{-3}, is explicitly included [123]. However, for realistic defects in crystals such corrections do not always improve the convergence and, generally, very big supercells are needed for reliable energy calculations.

B.1 Correction scheme

In our work we used the scheme proposed by Freysoldt *et al.* [118] to study the energetics of charged defects. They proposed a three step thought process to create a charged defect each step of which provides a quantity needed for the final expression.

1. A defect, with charge q, is created by adding or removing electrons from a defect state ψ_d while all other states are frozen. An unscreened charge density is obtained
$$\rho_d(\mathbf{r}) = q|\psi_d(\mathbf{r})|^2 \tag{B.2}$$
2. All electrons are permitted to relax and to screen the introduced charge. This relaxation gives rise to a change in the electrostatic potential with respect the neutral bulk system
$$\Delta V(\mathbf{r}) = V_{\text{defect}}(\mathbf{r}) - V_{\text{bulk}}(\mathbf{r}) \tag{B.3}$$
3. Periodic boundary conditions are imposed and a neutralizing background of uniform charge, $\rho_0 = -q/\Omega$, is added (Ω is the volume of the supercell).

The last stage implies that the potential will be the sum of the terms $\Delta V(\mathbf{r}+\mathbf{R})$, where $\mathbf{R}$ denotes the lattice vectors. This direct sum, actually, is not convergent but the divergence is removed by the added uniform background. Mathematically, this is realized if one removes the term $\mathbf{G} = 0$ of the Fourier transform

$$\Delta V(\mathbf{G}) = \int d\mathbf{r}\, \Delta V(\mathbf{r})\, e^{-i\mathbf{G}\cdot\mathbf{r}}. \tag{B.4}$$

Therefore, the periodic potential can be writen as a Fourier series without the divergent Fourier component

$$\Delta\tilde{V}(\mathbf{r}) = \frac{1}{\Omega}\sum_{\mathbf{G}\neq 0} \Delta V(\mathbf{G})\, e^{i\mathbf{G}\cdot\mathbf{r}}. \tag{B.5}$$

Of course, the unphysical potential due to the artificial periodicity is given by $[\Delta\tilde{V}(\mathbf{r}) - \Delta V(\mathbf{r})]$. Now if the defect state ψ_d is localized so that the defect charge density is fully contained in the supercell $\mathbf{R} = 0$, it is possible to write down the spurious energetic term we need for corrections.

First of all we have an unphysical interaction between the defect at $\mathbf{R} = 0$ and all the periodic images, $\mathbf{R} \neq 0$. Using the current formalism the energy due to this interaction is

$$\mathrm{E}_{\text{def-def}} = \frac{1}{2}\int_\Omega d\mathbf{r}\, [\rho_d(\mathbf{r}) + \rho_0][\Delta\tilde{V}(\mathbf{r}) - \Delta V(\mathbf{r})] \tag{B.6}$$

furthermore, the presence of the background introduces unphysical interaction between the charge defect and the background itself inside the supercell

$$\mathrm{E}_{\text{def-back}} = \int_\Omega d\mathbf{r}\, \rho_0\, \Delta V(\mathbf{r}). \tag{B.7}$$

Finally, the correction energy term will be the sum

$$\mathrm{E}_{\text{corr}} = \mathrm{E}_{\text{def-def}} + \mathrm{E}_{\text{def-back}}. \tag{B.8}$$

It is possible to rearrange equations (B.6), (B.7) by noting one see that the localized charge defect gives rise to a potential that, for large distance $|\mathbf{r}| \to \infty$, is dominated by the macroscopically screened Coulomb potential

$$\Delta V(\mathbf{r}) \to V_q^{\text{lr}}(\mathbf{r}) = \frac{1}{\varepsilon}\int d\mathbf{r}'\, \frac{\rho_d(\mathbf{r}')}{|\mathbf{r}-\mathbf{r}'|} \tag{B.9}$$

(here ε is the macroscopic dielectric constant. Its value will be calculated by means of DFT calculation, see below). Thus, the potential can be written as a sum of long-range and short-range terms

$$\Delta V(\mathbf{r}) = V_q^{\mathrm{lr}}(\mathbf{r}) + V^{\mathrm{sr}}(\mathbf{r})\,. \tag{B.10}$$

Furthermore, if we consider the periodicity

$$\Delta \tilde{V}(\mathbf{r}) = \tilde{V}_q^{\mathrm{lr}}(\mathbf{r}) + \tilde{V}^{\mathrm{sr}}(\mathbf{r})\,. \tag{B.11}$$

while, as usual the long-range part of the periodic potential is

$$\tilde{V}_q^{\mathrm{lr}}(\mathbf{r}) = \sum_{\mathbf{R}} V_q^{\mathrm{lr}}(\mathbf{r}+\mathbf{R}) \tag{B.12}$$

$$= \frac{1}{\Omega}\sum_{\mathbf{G}\neq 0} V_q^{\mathrm{lr}}(\mathbf{G})\, e^{i\mathbf{G}\cdot\mathbf{r}} \tag{B.13}$$

and, if $\rho_d(\mathbf{r})$ is almost totally inside the cell, the short-range part is

$$\tilde{V}^{\mathrm{sr}}(\mathbf{r}) = \sum_{\mathbf{R}} V^{\mathrm{sr}}(\mathbf{r}+\mathbf{R}) \tag{B.14}$$

$$\simeq V^{\mathrm{sr}}(\mathbf{r}) + C \quad \text{with } \mathbf{r}\in\Omega\,.$$

Substituting the previous results into Eqs. (B.6) and (B.7) we are able to distinguish a correction term due to the long-range part of the potential corresponding to the macroscopically screened lattice energy of ρ_d with neutralizing background

$$\mathrm{E}_{\mathrm{lattice}} = \int_\Omega d\mathbf{r}\,\frac{1}{2}[\rho_d(\mathbf{r})+\rho_0][\tilde{V}_q^{\mathrm{lr}}(\mathbf{r}) - V_q^{\mathrm{lr}}(\mathbf{r})] + \rho_0 V_q^{\mathrm{lr}}(\mathbf{r}) \tag{B.15}$$

and an alignment-like term

$$\Delta_q = \frac{1}{\Omega}\int_\Omega d\mathbf{r}\, V^{\mathrm{sr}}(\mathbf{r}) \tag{B.16}$$

where

$$V^{\mathrm{sr}}(\mathbf{r}) = \Delta\tilde{V}(\mathbf{r}) - \tilde{V}_q^{\mathrm{lr}}(\mathbf{r}) - C\,. \tag{B.17}$$

Equations (B.15), (B.16) and (B.17) are the main quantities which allow us to calculate the energetic correction term

$$\mathrm{E}_{\mathrm{corr}} = \mathrm{E}_{\mathrm{lattice}} + q\Delta_q\,. \tag{B.18}$$

B.2 LiNH$_2$ bulk charged defects

In the scheme shown previously it is possible to calculate the right formation energy for an isolated defect, x^q, the only requirement being that the defect state ψ_d is very localized so the defect charge density, $\rho_d(\mathbf{r})$, is fully contained into the simulation supercell. Hence, the right formation energy could be calculated within the framework of DFT with PBC using the formula

$$\mathrm{E_f}(x^q) = \mathrm{E_{tot}}(x^q) - \mathrm{E_{tot}}[\mathrm{bulk}] - n\mu + \\ + q(\mu_{\mathrm{F}} + \mathrm{E_v} + \Delta_q) - \mathrm{E_{lattice}} \tag{B.19}$$

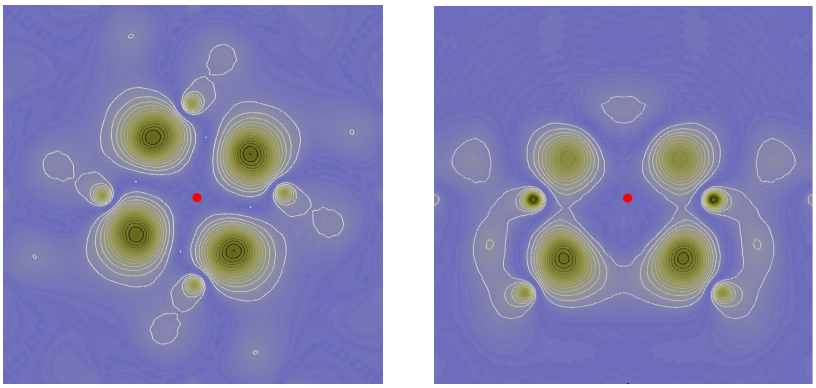

(a) $|\psi_d|^2$ plane (001) (b) $|\psi_d|^2$ plane (010)

Figure B.1: 2D representation of the well localized Li-vacancy$^-$ defect charge density, $q|\psi_d^2|$, for $LiNH_2$. In this case ψ_d has been chosen to be the highest occupied Kohn-Sham state. The red dot indicates the vacancy position: (0, 0, 0) in crystal units.

where x^q is the kind of charged defect studied (interstitial/vacancy), q is its charge, μ is the chemical potential of the standard state of the element involved – *e.g.*, for lithium interstitial/vacancy defect μ is the chemical potential of the standard metallic state of Li. μ_F is the Fermi level referred to the energy of the valence band maximum E_v and n is +1 for interstitial atom defect or -1 for vacancy defect.

Applying this scheme we have calculated the formation energy for a Li-vacancy, with a charge of -1 charged, in the $LiNH_2$ bulk. The system has been modeled with a $2 \times 2 \times 2$ $LiNH_2$ supercell of 255 atoms in which the vacancy occupies the (0, 0, 0) position in crystal units. The calculations have been performed, as usual, within DFT-PBE with a cutoff of 50 Ry for the wave-functions while only the Γ-point in the Brillouin Zone (BZ) integration has been considered. To be sure that the main requirement of the correction scheme was fulfilled we have extracted from our *ab initio* calculations the highest occupied Kohn-Sham state and plotted it. This is our defect state and, as shown in Fig. B.1, it is a well localized state as the theory requires.

Let see how we obtained the important quantities to explicitly calculate the artificial interactions when PBC are used: ε, $\rho_d(\mathbf{r})$, $\Delta\tilde{V}(\mathbf{r})$ and C.

We used the theoretical value of ε as calculated within the framework of density-functional perturbation theory [114, 115] (for $LiNH_2$ ε=2.61). The defect charge density, $\rho_d(\mathbf{r})$, was modeled with a spherically symmetric Gaussian charge density with $\sigma \sim 0.5$ Å

$$\rho_d(r) \approx \rho_G(r) = \frac{q}{\sqrt{8\pi^3}\,\sigma^3}\, e^{-r^2/2\sigma^2}. \tag{B.20}$$

In fact, it turns out that any reasonable approximation for ρ_d suffices since the sum of lattice energy and alignment correction are not sensitive to the details of ρ_d. Putting this

charge distribution into the Poisson's equation gives

$$\nabla^2\varphi(r) = -\frac{\rho_G(r)}{\varepsilon} \tag{B.21}$$

we obtained the related electrostatic potential

$$\varphi(r) = \frac{1}{4\pi\varepsilon}\frac{q}{r}\,\mathrm{erf}\left(\frac{r}{\sqrt{2}\sigma}\right) \tag{B.22}$$

where erf(x) is the error function. Of course when r is greater than σ, the error function approaches unity quickly and the potential, φ, approaches the point-charge potential $\frac{1}{4\pi\varepsilon}\frac{q}{r}$, as one would expect. For these reasons the long-range part of the potential can be approximated as

$$V_q^{\mathrm{lr}} \equiv \varphi(r) \tag{B.23}$$

and

$$\tilde{V}_q^{\mathrm{lr}} \equiv \tilde{\varphi}(r)\,. \tag{B.24}$$

The value of $\Delta\tilde{V}$ was directly obtained from our DFT supercell with PBC calculations. The quantities calculated so far allowed us to evaluate the lattice energy correction for a Li-vacancy$^-$ in $LiNH_2$ bulk using Eq. (B.15).

To calculate the alignment constant one requires that the short-range potential V^{sr} decays to zero far from the defect. In practice, we calculated the planar average of potentials in the xy planes as a function of z. Figure B.2 illustrates this for the potentials $\Delta\tilde{V}$, V_q^{lr} and for their difference. This difference $\Delta\tilde{V} - V_q^{\mathrm{lr}}$ reaches a plateau $C \approx -0.18$ eV (thin dashed line) between the positions of the two defects located at z=0 Å and, its image, at z=20.66 Å.

Finally, using Eq. (B.19) the correct formation energy for the vacancy was obtained. In order to have more information on defect-defect interactions we calculated the formation energy for the Li-vacancy with alignment correction only

$$\begin{aligned}\mathrm{E_f}(x^q) = \mathrm{E_{tot}}(x^q) - \mathrm{E_{tot}}[\mathrm{bulk}] - n\mu + \\ + q(\mu_{\mathrm{F}} + \mathrm{E_v} + \Delta'_q)\,.\end{aligned} \tag{B.25}$$

Here Δ'_q is the alignment term between the averaged bulk potential, $\tilde{V}_{bulk}(z)$, and the averaged bulk with vacancy potential, $\tilde{V}_{\text{Li-vac}}(z)$ (see Fig. B.3(a))

Comparing the two methods the difference in formation energy was on the order of 0.07 eV. This means that for our system the alignment term was the dominant term in energy correction and the term due to defect-defect interactions could be neglected.

A Li^+-interstitial ion defect has been considered as well. In contrast to a Li-vacancy here the defect state ψ_d was completely delocalized in the simulation cell. For this reason we could not apply the correction scheme already used for the Li-vacancy. However, given that, for the localized vacancy state, the energy lattice correction could be neglected for $LiNH_2$, for delocalized states the replica interactions are also unimportant. Therefore, considering that only the defect charge density and uniform background interaction were significant for the correction, we refined the formation energy with the alignment term only (see Fig. B.3(b)).

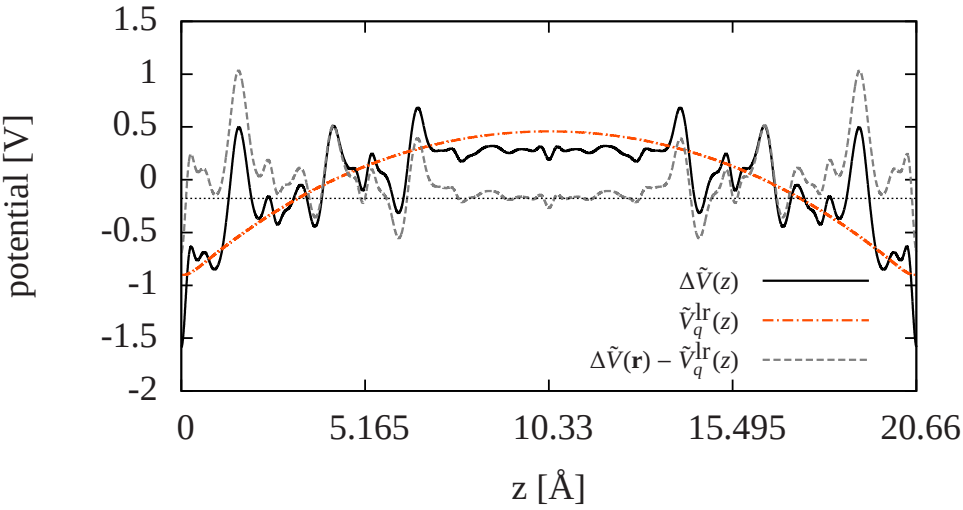

Figure B.2: With reference to the text we plot here the electrostatic potentials (averaged on x,y plane as function of z) for a Li-vacancy^{-} in a 2×2×2 supercell of $LiNH_2$. The defect is located at z=0 Å with its periodic image at z=20.66 Å.

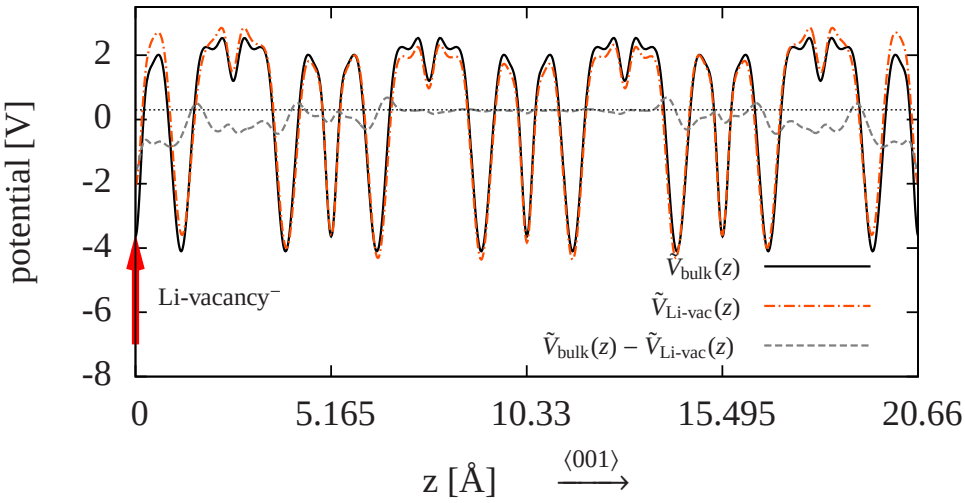

(a) Li-vacancy$^-$

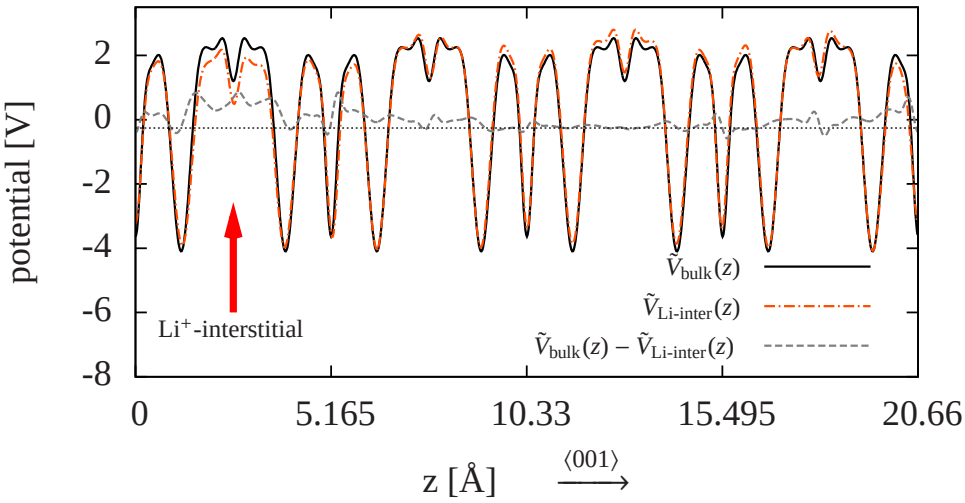

(b) Li^+-interstitial

Figure B.3: Electrostatic potentials for $LiNH_2$ bulk, (a) with a Li-vacancy and (b) with a Li-interstitial. The red arrows in the pictures indicate (a) the position of vacancy and (b) the position of Li-interstitial defects respectively.

Bibliography

[1] Verne, J. ***L'île mystérieuse***, 1874. http://www.gutenberg.org/wiki/Main_Page, available on line: The Project Gutenberg EBook.

[2] Schlapbach, L.; Züttel, A. Hydrogen-storage materials for mobile applications. *Nature* **2001**, *414*, 353–358.

[3] Grochala, W.; Edwards, P. Thermal decomposition of the non-interstitial hydrides for the storage and production of hydrogen. *Chemical Reviews* **2004**, *104*, 1283–1316.

[4] *U.S. Department of Energy*. http://www.energy.gov/.

[5] Bogdanović, B.; Schwickardi, M. Ti-doped alkali metal aluminium hydrides as potential novel reversible hydrogen storage materials. *Journal of Alloys and Compounds* **1997**, *253*, 1–9.

[6] Bogdanović, B.; Schwickardi, M. Ti-doped NaAlH4 as a hydrogen-storage material–preparation by Ti-catalyzed hydrogenation of aluminum powder in conjunction with sodium hydride. *Applied Physics A: Materials Science & Processing* **2001**, *72*, 221–223.

[7] Orimo, S.; Nakamori, Y.; Elise, J. F.; Züttel, A.; Jensen, C. M. Complex Hydrides for Hydrogen Storage. *Chemical Reviews* **2007**, *107*, 4111.

[8] Sakintuna, B.; Lamari-Darkrim, F.; Hirscher, M. Metal hydride materials for solid hydrogen storage: A review. *International Journal of Hydrogen Energy* **2007**, *32*, 1121 – 1140.

[9] Chen, P.; Xiong, Z.; Luo, J.; Lin, J.; Tan, K. L. Interaction of hydrogen with metal nitrides and imides. *Nature* **2002**, *420*, 302–304.

[10] Chen, P.; Zhu, M. Recent progress in hydrogen storage. *Materials Today* **2008**, *11*, 36.

[11] Balogh, M. P.; Jones, C. Y.; Herbst, J. F.; Hector Jr, L. G.; Kundrat, M. Crystal structures and phase transformation of deuterated lithium imide, Li_2ND. *Journal of Alloys and Compounds* **2006**, *420*, 326.

[12] Chen, P.; Xiong, Z.; Luo, J.; Lin, J.; Tan, K. L. Interaction between Lithium Amide and Lithium Hydride. *The Journal of Physical Chemistry B* **2003**, *107*, 10967–10970.

[13] Ichikawa, T.; Hanada, N.; Isobe, S.; Leng, H. Y.; Fujii, H. J. Mechanism of novel reaction from $LiNH_2$ and LiH to Li_2NH and H_2 as a promising hydrogen storage system. *The Journal of Physical Chemistry B* **2004**, *108*, 7887–7892.

[14] Hu, Y. H.; Ruckenstein, E. Ultra-fast reaction between LiH and NH_3 during H_2 storage in Li_3N. *The Journal of Physical Chemistry A* **2003**, *107*, 9737–9739.

[15] Isobe, S.; Ichikawa, T.; Hino, S.; Fujii, H. Hydrogen Desorption Mechanism in a Li-N- H System by Means of the Isotopic Exchange Technique. *The Journal of Physical Chemistry B* **2005**, *109*, 14855–14858.

[16] Leng, H.; Ichikawa, T.; Fujii, H. Hydrogen Storage Properties of Li- Mg- N- H Systems with Different Ratios of LiH/Mg (NH2) 2. *The Journal of Physical Chemistry B* **2006**, *110*, 12964–12968.

[17] David, W. I. F.; Jones, M. O.; Gregory, D. H.; Jewell, C. M.; Johnson, S. R.; Walton, A.; Edwards, P. P. A mechanism for non-stoichiometry in the lithium amide/lithium imide hydrogen storage reaction. *Journal of the American Chemical Society* **2007**, *129*, 1594–1601.

[18] Shaw, L. L.; Osborn, W.; Markmaitree, T.; Wan, X. The reaction pathway and rate-limiting step of dehydrogenation of the $LiNH_2$+LiH mixture. *J. Power Sources* **2008**, *177*, 500–505.

[19] *Intergovernmental Panel on Climate Change*. http://www.ipcc.ch/.

[20] Harris, R.; Book, D.; Anderson, P.; Edwards, P. Hydrogen storage: the grand challenge. *The Fuel Cell Review* **2004**, *1*, 17–23.

[21] Crabtree, G.; Dresselhaus, M.; Buchanan, M. The hydrogen economy. *Physics Today* **2004**, *57*, 39–44.

[22] Edwards, P.; Kuznetsov, V.; David, W.; Brandon, N. Hydrogen and fuel cells: Towards a sustainable energy future. *Energy policy* **2008**, *36*, 4356–4362.

[23] Yang, Z.; Xia, Y.; Mokaya, R. Enhanced hydrogen storage capacity of high surface area zeolite-like carbon materials. *Journal of the American Chemical Society* **2007**, *129*, 1673–1679.

[24] Poirier, E.; Chahine, R.; Benard, P.; Cossement, D.; Lafi, L.; Melancon, E.; Bose, T. K.; Desilets, S. Storage of hydrogen on single-walled carbon nanotubes and other carbon structures. *Applied Physics A: Materials Science & Processing* **2004**, *78*, 961–967.

[25] Langmi, H. W.; Book, D.; Walton, A.; Johnson, S. R.; Al-Mamouri, M. M.; Speight, J. D.; Edwards, P. P.; Harris, I. R.; Anderson, P. A. Hydrogen storage in ion-exchanged zeolites. *Journal of Alloys and Compounds* **2005**, *404*, 637–642.

[26] Lin, X.; Jia, J.; Zhao, X.; Thomas, K. M.; Blake, A. J.; Walker, G. S.; Champness, N. R.; Hubberstey, P.; Schröder, M. High H2 Adsorption by Coordination-Framework Materials. *Angewandte Chemie International Edition* **2006**, *45*, 7358–7364.

[27] Budd, P.; Butler, A.; Selbie, J.; Mahmood, K.; McKeown, N.; Ghanem, B.; Msayib, K.; Book, D.; Walton, A. The potential of organic polymer-based hydrogen storage materials. *Physical Chemistry Chemical Physics* **2007**, *9*, 1802–1808.

[28] Vajo, J. J.; Skeith, S. L.; Mertens, F. Reversible storage of hydrogen in destabilized $LiBH_4$. *The Journal of Physical Chemistry B* **2005**, *109*, 3719–3722.

[29] Dafert, F. W.; Miklauz, R. Über einige neue Verbindungen von Stickstoff und Wasserstoff mit Lithium. *Mh. Chem.* **1912**, *33*, 65.

[30] Ruff, O.; Georges, F. On the lithium-imide and some remarks on the work by Dafert and Miklauz: "On some new compounds of nitrogen and hydrogen with lithium.". *Ber. Dtsch Chem. Ges.* **1911**, *44*, 504.

[31] Gregory, D. H. Lithium nitrides, imides and amides as lightweight, reversible hydrogen stores. *J. Mat. Chem.* **2008**, *18*, 1221–2330.

[32] Leng, H.; Ichikawa, T.; Isobe, S.; Hino, S.; Hanada, N.; Fujii, H. Desorption behaviours from metal-NH systems synthesized by ball milling. *Journal of Alloys and Compounds* **2005**, *404*, 443–447.

[33] Pinkerton, F. E. Decomposition kinetics of lithium amide for hydrogen storage materials. *Journal of Alloys and Compounds* **2005**, *400*, 76–82.

[34] Herbst, J. F.; Hector Jr, L. G. Energetics of the Li amide/Li imide hydrogen storage reaction. *Physical Review B* **2005**, *72*, 125120.

[35] Kojima, Y.; Kawai, Y. IR characterizations of lithium imide and amide. *Journal of Alloys and Compounds* **2005**, *395*, 236–239.

[36] Ichikawa, T.; Isobe, S.; Hanada, N.; Fujii, H. Lithium nitride for reversible hydrogen storage. *Journal of Alloys and Compounds* **2004**, *365*, 271–276.

[37] Hu, Y.; Ruckenstein, E. H_2 storage in Li_3N. Temperature-programmed hydrogenation and dehydrogenation. *Industrial & Engineering Chemistry Research* **2003**, *42*, 5135–5139.

[38] Markmaitree, T.; Ren, R.; Shaw, L. L. Enhancement of lithium amide to lithium imide transition via mechanical activation. *The Journal of Physical Chemistry B* **2006**, *110*, 20710–20718.

[39] Kojima, Y.; Kawai, Y. Hydrogen storage of metal nitride by a mechanochemical reaction. *Chemical Communications* **2004**, 2210–2211.

[40] Kojima, Y.; Kawai, Y.; Ohba, N. Hydrogen storage of metal nitrides by a mechanochemical reaction. *Journal of Power Sources* **2006**, *159*, 81–87.

[41] Ichikawa, T.; Hanada, N.; Isobe, S.; Leng, H.; Fujii, H. Hydrogen storage properties in Ti catalyzed Li-N-H system. *Journal of Alloys and Compounds* **2005**, *404-406*, 435 – 438.

[42] Isobe, S.; Ichikawa, T.; Hanada, N.; Leng, H.; Fichtner, M.; Fuhr, O.; Fujii, H. Effect of Ti catalyst with different chemical form on Li-NH hydrogen storage properties. *Journal of Alloys and Compounds* **2005**, *404*, 439–442.

[43] Nakamori, Y.; Orimo, S. Li-N based hydrogen storage materials. *Materials Science and Engineering B* **2004**, *108*, 48–50.

[44] Nakamori, Y.; Orimo, S. Destabilization of Li-based complex hydrides. *Journal of Alloys and Compounds* **2004**, *370*, 271–275.

[45] Yang, J. B.; Zhou, X. D.; Cai, Q.; James, W. J.; Yelon, W. B. Crystal and electronic structures of $LiNH_2$. *Appl. Phys. Lett.* **2006**, *88*, 041914.

[46] Miwa, K.; Ohba, N.; Towata, S.; Nakamori, Y.; Orimo, S. First-principles study on lithium amide for hydrogen storage. *Physical Review B* **2005**, *71*, 195109.

[47] Song, Y.; Guo, Z. X. Electronic structure, stability and bonding of the Li-NH hydrogen storage system. *Physical Review B* **2006**, *74*, 195120.

[48] Titherley, A. W. XLV.–Sodium, potassium, and lithium amides. *Journal of the Chemical Society* **1894**, *65*, 504 – 522.

[49] Juza, V. R.; Opp, K. Metallamide und Metallnitride, 25. Mitteilung. Zur Kenntnis des Lithiumimides. *Z. Anorg. Allg. Chemie.* **1951**, *266*, 325–330.

[50] Nagib, M.; Jacobs, H. Neutron Diffraction by Lithium Deuteroamides. *Atomkernenergie* **1973**, *21*, 275–278.

[51] Sørby, M.; Nakamura, Y.; Brinks, H.; Ichikawa, T.; Hino, S.; Fujii, H.; Hauback, B. The crystal structure of $LiND_2$ and $Mg(ND_2)_2$. *Journal of Alloys and Compounds* **2007**, *428*, 297–301.

[52] Jolly, W. *The inorganic chemistry of nitrogen*; W. A. Benjamin: New York, 1964.

[53] Franklin, E. C. *The nitrogen system of compounds*; Reinhold: New York, 1935; pp 53–63.

[54] Forman, R. A. Order-disorder transition in Lithium imide, Li_2NH. *The Journal of Chemical Physics* **1971**, *55*, 1987.

[55] Haigh, P. J.; Forman, R. A.; Frish, R. C. Nuclear Magnetic Resonance of ^7Li and ^1H in Solid Lithium Imide, Lithium Amide, and Lithium Nitride. *The Journal of Chemical Physics* **1966**, *45*, 812.

[56] Ohoyama, K.; Nakamori, Y.; Orimo, S.; Yamada, K. Revised crystal structure model of Li_2NH by neutron powder diffraction. *J. Phys. Soc. Jpn.* **2005**, *74*, 483–487.

[57] Rietveld, H. Line Profiles of Neutron Powder-diffraction Peaks for Structure Refinement. *Acta Crystallogr.* **1967**, *22*, 151–2.

[58] Rietveld, H. A Profile Refinement Method for Nuclear and Magnetic Structures. *J. Appl. Crystallogr.* **1969**, *2*, 65–71.

[59] Noritake, T.; Nozaki, H.; Aoki, M.; Towata, S.; Kitahara, G.; Nakamori, Y.; Orimo, S. Crystal structure and charge density analysis of Li_2NH by synchrotron X-ray diffraction. *Journal of Alloys and Compounds* **2005**, *393*, 264–268.

[60] Allen, F. H. A systematic pairwise comparison of geometric parameters obtained by X-ray and neutron diffraction. *Acta Cryst.* **1986**, *B42*, 515–522.

[61] Rijssenbeek, J.; Gao, Y.; Hanson, J.; Huang, Q.; Jones, C.; Toby, B. Crystal structure determination and reaction pathway of amide-hydride mixtures. *Journal of Alloys and Compounds* **2008**, *454*, 233 – 244.

[62] Hector Jr, L. G.; Herbst, J. F. Density functional theory for hydrogen storage materials: successes and opportunities. *Journal of Physics: Condensed Matter* **2008**, *20*, 064229.

[63] Magyari-Köpe, B.; Ozolins, V.; Wolverton, C. Theoretical prediction of low-energy crystal structures and hydrogen storage energetics in Li_2NH. *Physical Review B* **2006**, *73*, 20101(R).

[64] Mueller, T.; Ceder, G. Effective interactions between the N-H bond orientations in lithium imide and a proposed ground-state structure. *Physical Review B* **2006**, *74*, 134104.

[65] Osborn, W.; Markmaitree, T.; Shaw, L.; Hu, J.-Z.; Kwak, J.; Yang, Z. Low temperature milling of the $LiNH_2$ + LiH hydrogen storage system. *Int. J. Hydrogen Energy* **2009**, *34*, 4331–4339.

[66] Osborn, W.; Markmaitree, T.; Shaw, L. L. The long-term hydriding and dehydriding stability of the nanoscale LiNH2+ LiH hydrogen storage system. *Nanotechnology* **2009**, *20*, 204028.

[67] Ashcroft, N. W.; Mermin, N. D. *Solid State Physics*; Holt, Rinehart and Winston, New York, 1976.

[68] Hartree, D. The wave mechanics of an atom with a non-Coulomb central field. Part I. Theory and methods. *Mathematical Proceedings of the Cambridge Philosophical Society*, 1928; pp 89–110.

[69] Fock, V. Näherungsmethode zur Lösung des quantenmechanischen Mehrkörperproblems. *Zeitschrift für Physik A Hadrons and Nuclei* **1930**, *61*, 126–148.

[70] Szabo, A.; Ostlund, N. *Modern quantum chemistry*; McGraw-Hill New York, 1989.

[71] Pople, J. Nobel lecture: Quantum chemical models. *Reviews of Modern Physics* **1999**, *71*, 1267–1274.

[72] Parr, R.; Yang, W. *Density-functional theory of atoms and molecules*; Oxford University Press, USA, 1994.

[73] Dreizler, R.; Gross, E. *Density functional theory. An approach to the quantum many-body problem*; Berlin etc, 1990.

[74] March, N. H. *Electron Density Theory of Atoms and Molecules*; Academic Press, London, 1992.

[75] Hohenberg, P.; Kohn, W. Inhomogeneous Electron Gas. *Physical Review* **1964**, *136*, B864–B871.

[76] Kohn, W.; Sham, L. Self-Consistent Equations Including Exchange and Correlation Effects. *Physical Review* **1965**, *140*, A1133–A1138.

[77] Ceperley, D.; Alder, B. Ground state of the electron gas by a stochastic method. *Physical Review Letters* **1980**, *45*, 566–569.

[78] Perdew, J.; Burke, K.; Ernzerhof, M. Generalized gradient approximation made simple. *Physical Review Letters* **1996**, *77*, 3865–3868.

[79] Perdew, J.; Wang, Y. Accurate and simple analytic representation of the electron-gas correlation energy. *Physical Review B* **1992**, *45*, 13244–13249.

[80] Monkhorst, H.; Pack, J. D. Special points for Brillouin-zone integrations. *Physical Review B* **1976**, *13*, 5188–5192.

[81] Lippert, G.; Hutter, J.; Parrinello, M. A hybrid Gaussian and plane wave density functional scheme. *Mol. Phys.* **1997**, *92*, 477–487.

[82] Krack, M.; Parrinello, M. In *High Performance Computing in Chemistry*; Grotendorst, J., Ed.; NIC, 2004; Vol. 25, pp 29–51.

[83] VandeVondele, J.; Krack, M.; Mohamed, F.; Parrinello, M.; Chassaing, T.; Hutter, J. QUICKSTEP: Fast and accurate density functional calculations using a mixed gaussian and plane waves approach. *Computer Physics Communications* **2005**, *167*, 103–128.

[84] *CP2K*. http://cp2k.berlios.de, freely available, released under GPL license.

[85] Goedecker, S.; Teter, M.; Hutter, J. Separable dual-space Gaussian pseudopotentials. *Physical Review B* **1996**, *54*, 1703–1710.

[86] Krack, M. Pseudopotentials for H to Kr optimized for gradient-corrected exchange-correlation functionals. *Theoretical Chemistry Accounts: Theory, Computation, and Modeling (Theoretica Chimica Acta)* **2005**, *114*, 145–152.

[87] Pechukas, P. Transition state theory. *Annual Review of Physical Chemistry* **1981**, *32*, 159–177.

[88] Laidler, K.; King, M. Development of transition-state theory. *The Journal of Physical Chemistry* **1983**, *87*, 2657–2664.

[89] Truhlar, D.; Garrett, B. Variational Transition State Theory. *Annual Review of Physical Chemistry* **1984**, *35*, 159–189.

[90] Voter, A.; Doll, J. Dynamical corrections to transition state theory for multistate systems: Surface self-diffusion in the rare-event regime. *The Journal of Chemical Physics* **1985**, *82*, 80.

[91] Feynman, R. P.; Hibbs, A. R. *Quantum Mechanics and Path Integrals*; McGraw-Hill, New York, 1965.

[92] Henkelman, G.; Jónsson, H. Improved tangent estimate in the nudged elastic band method for finding minimum energy paths and saddle points. *The Journal of Chemical Physics* **2000**, *113*, 9978.

[93] Henkelman, G.; Uberuaga, B.; Jónsson, H. A climbing image nudged elastic band method for finding saddle points and minimum energy paths. *The Journal of Chemical Physics* **2000**, *113*, 9901.

[94] Ceperley, D. Path integrals in the theory of condensed helium. *Reviews of Modern Physics* **1995**, *67*, 279–355.

[95] Marx, D.; Hutter, J. Ab initio molecular dynamics: theory and implementation. *Modern methods and algorithms of quantum chemistry* **2000**, *1*, 301–449.

[96] Ceriotti, M.; Bussi, G.; Parrinello, M. Langevin equation with colored noise for constant-temperature molecular dynamics simulations. *Physical Review Letters* **2009**, *102*, 20601.

[97] Ceriotti, M.; Bussi, G.; Parrinello, M. Nuclear quantum effects in solids using a colored-noise thermostat. *Physical Review Letters* **2009**, *103*, 30603.

[98] Ceriotti, M.; Bussi, G.; Parrinello, M. Colored-Noise Thermostats à la Carte. *Journal of Chemical Theory and Computation* **2010**, *6*, 1170–1180.

[99] QUANTUM-ESPRESSO. http://www.quantum-expresso.org,http://www.pwscf.org, QUANTUM-ESPRESSO is a community project for high-quality quantum-simulation software, based on density-functional theory, and coordinated by Paolo Giannozzi.

[100] Vanderbilt, D. Soft self-consistent pseudopotentials in a generalized eigenvalue formalism. *Physical Review B* **1990**, *41*, 7892–7895.

[101] *CPMD*. http://www.cpmd.org/, Copyright IBM Corp 1990-2008, Copyright MPI für Festkörperforschung Stuttgart 1997-2001.

[102] Ceperley, D. M. Path integrals in the theory of condensed helium. *Reviews of Modern Physics* **1995**, *67*, 279–355.

[103] Morrone, J.; Car, R. Nuclear quantum effects in water. *Physical Review Letters* **2008**, *101*, 17801.

[104] Lin, L.; Morrone, J.; Car, R.; Parrinello, M. Displaced path integral formulation for the momentum distribution of quantum particles. *Arxiv preprint arXiv:1004.0868* **2010**.

[105] Giacomazzi, L.; Umari, P.; Pasquarello, A. Vibrational spectra of vitreous germania from first-principles. *Physical Review B* **2006**, *74*, 155208.

[106] Kohanoff, J.; Andreoni, W.; Parrinello, M. Zero-point-motion effects on the structure of C_{60}. *Physical Review B* **1992**, *46*, 4371–4373.

[107] Reiter, G.; Li, J. C.; Mayers, J.; Abdul-Redah, T.; Platzman, P. The proton momentum distribution in water and ice. *Braz. J. Phys.* **2004**, *34*, year.

[108] Garbuio, V.; Andreani, C.; Imberti, S.; Pietropaolo, A.; Reiter, G.; Senesi, R.; Ricci, M. Proton quantum coherence observed in water confined in silica nanopores. *The Journal of chemical physics* **2007**, *127*, 154501.

[109] Araujo, C. M.; Blomqvist, A.; Scheicher, R. H.; Chen, P.; Ahuja, R. Superionicity in the hydrogen storage material Li_2NH: Molecular dynamics simulations. *Physical Review B* **2009**, *79*, 172101.

[110] Becke, A. D. Density-functional exchange-energy approximation with correct asymptotic behavior. *Physical Review A* **1988**, *38*, 3098.

[111] Lee, C.; Yang, W.; Parr, R. G. Development of the Colle-Salvetti correlation-energy formula into a functional of the electron density. *Physical Review B* **1988**, *37*, 785–789.

[112] Noritake, T.; Nozaki, H.; Aoki, M.; Kitahara, G.; Nakamori, Y.; Orimo, S. Crystal structure and charge density analysis of Li2NH by synchrotron X-ray diffraction. *Journal of Alloys and Compounds* **2005**, *393*, 264–268.

[113] Giannozzi, P.; *et al.*, *Quantum-ESPRESSO*. http://www.quantum-expresso.org,http://www.pwscf.org.

[114] Baroni, S.; Resta, R. Ab initio calculation of the macroscopic dielectric constant in silicon. *Physical Review B* **1986**, *33*, 7017–7021.

[115] Baroni, S.; de Gironcoli, S.; Dal Corso, A.; Giannozzi, P. Phonons and related crystal properties from density-functional perturbation theory. *Reviews of Modern Physics* **2001**, *73*, 515.

[116] Jacobs, V. H.; Juza, R. New determination of crystal-structure of lithium amide. *Z. Anorg. Allg. Chem.* **1972**, *391*, 271.

[117] Murnaghan, D. The compressibility of media under extreme pressures. *Proc. Nat. Acad. Sci. USA* **1944**, *30*, 224.

[118] Freysoldt, C.; Neugebauer, J.; Van de Walle, C. Fully Ab Initio Finite-Size Corrections for Charged-Defect Supercell Calculations. *Physical Review Letters* **2009**, *102*, 016402.

[119] Van de Walle, C.; Neugebauer, J. First-principles calculations for defects and impurities: Applications to III-nitrides. *J. Appl. Phys.* **2004**, *95*, 3851.

[120] Agmon, N. The Grotthuss mechanism. *Chemical Physics Letters* **1995**, *244*, 456–462.

[121] Tuckerman, M.; Laasonen, K.; Sprik, M.; Parrinello, M. Ab initio molecular dynamics simulation of the solvation and transport of H_3O^+ and OH^- ions in water. *The Journal of Physical Chemistry* **1995**, *99*, 5749–5752.

[122] Leslie, M.; Gillan, N. J. The energy and elastic dipole tensor of defects in ionic crystals calculated by the supercell method. *J. Phys. C* **1985**, *18*, 973.

[123] Makov, G.; Payne, M. C. Periodic boundary conditions in ab initio calculations. *Physical Review B* **1995**, *51*, 4014.

Acknowledgements

It is a pleasure to thank all the people who made this thesis possible.

First of all I would like to express my gratitude to my supervisor Prof. Marco Bernasconi. He has always supported and guided me through this journey. I have appreciated his contributions of time, ideas and suggestions to make my Ph.D. experience stimulating and productive. He has taught me the rigorous way of doing research.

It is a pleasure and an honor for me to thank Prof. Michele Parrinello. For the second time, after my Master's degree, he gave me the opportunity to join his group in Lugano to pursue my research activity. Once again I enjoyed a lot of the stimulating environment that characterizes this group.

I owe debt of gratitude to Lord Tribello of Gibraltar a.k.a. Garretto, who has, over the past three years, tried to accomplish the desperate mission of teaching me English. I would also like to express my gratitude to *Maestro* Ali Hassanali who, together with Gareth, checked for grammar mistakes in this thesis.

Thank you to the members of the Parrinello group. They have contributed immensely to my personal and professional time in Lugano: Michele, Meher, Alessandro, Enrico, Sebastiano, Hagai, Rustam, Giovanni, Rodrigo, Tilde, Paolo, Max. Thanks to Daniela Wirz for helping me in every single bureaucratic problem concerning my stay in Switzerland. Thanks to Gabriele and all the people in Milano.

Special thanks go to the many people with which I shared much of my free time in Lugano. Anna Berteotti, the "wise woman". We discussed, during lunch time, about our doubts concerning the future and most of the time she mitigated my pessimistic view. Vittorio Limongelli and Ivan Rivalta, I enjoyed the relaxing time that I spent with them. With pleasure I remember the nice day we spent together in Scilla this summer.

I owe debt of gratitude to all my best friends. I was able to avoid cooking after a hard days of work thanks to my friend Silvia Piras who generously used to invite me to dinner. Thanks to my friend and colleague Michele Pepe for the nice discussions, advises and

time we spent together. Davide Portelli, the “adventurous man”, with whom I shared wonderful experiences and adventures in Pisa and around Europe. I remember with immense pleasure the last minute trips organized for Frankfurt and Munchen. Thanks to all my best friends in Sicily and those that at the moment live in various cities around the world. Thank you!

I would like to thank Adele with whom I spent wonderful days in the last year. She always finds a way to make me happy when I am at my worst. Thanks to Cristina and all the friends in Geneva for inviting me to the nice parties they have organized.

Lastly, I would like to thank my family for their love. For my brother Roberto who gives me encouragement and for my mother who always supports and encourages me. Thank you!